The composition of kimberlite magma with implications for the Earth's environment

by

Michael Vincent Patterson

Department of Earth and Planetary Sciences

McGill University, Montréal

November 2014

A thesis submitted to

Graduate and Post-doctoral Studies

in partial fulfilment of requirements of the degree of

Doctor of Philosophy

Abstract

Despite general agreement amongst kimberlite researchers on many of the basic characteristics of kimberlite, the International Union of Geological Sciences (IUGS) still considers kimberlite undefined. Furthermore, a fundamental and crucially important characteristic of kimberlite is still fiercely debated: the composition of its primary magma. Two distinct schools of thought have emerged to explain the composition of kimberlite magma. The first favors a volatile-rich ultramafic silicate melt while the other suggests a silico-carbonatite parental melt. Kimberlite can be described by two principle components: mantle-derived carbonate and xenocrystic olivine. Despite this prevalence of carbonate and the near-absence of magmatic olivine, the parental magma is often assumed to be a volatile-rich ultramafic silicate melt. The overwhelming volume of silicate magmatism, operating within the framework of plate tectonics, has led to a bias against the existence of any magmatic process that is divorced from plate tectonics and would thus result in a magma composition that is different in chemical character. This thesis investigates the nature of the composition of kimberlite magma, constraining the composition of kimberlite magma by using the composition of magmatic olivine overgrowths and the composition of kimberlite pelletal lapilli. This thesis then illustrates the implications of kimberlite eruptions of that composition on Earth's climate.

In an effort to elucidate the outstanding question regarding the composition of the parental magma of kimberlite, the magmatic overgrowths on xenocrystic olivine grains from kimberlite are utilized as an avenue to constrain the composition of the magma from which they crystallized. The majority of the olivine core compositions are similar to that of olivine in the sub-continental lithospheric mantle (~Fo_{92} and Ni ~3,000 ppm), although there are two

other less abundant types of olivine core compositions observed. However, the composition of the olivine margin is distinct in each kimberlite suite, regardless of the composition of the olivine core. Although the compositions of the olivine margins are distinct within the individual kimberlite suites, they vary from Fo_{87} to Fo_{91} between kimberlite suites. Although the initial compositional pattern varies, composition of the olivine margin stabilizes to constant forsterite composition and Ni contents. Clearly a similar process or processes are responsible for these magmatic margin compositions, and these may provide evidence for the composition of the magma from which they crystallized.

In addition to utilizing the direct evidence that magmatic overgrowths on kimberlite olivine provide, a more indirect approach to constraining the composition of kimberlite magma utilizes pelletal lapilli commonly found in kimberlite. Pelletal lapilli have long been recognized as droplets of magma formed during the eruption of a variety of volcanic suites, including kimberlites. A comparison of the compositions of pelletal lapilli from three kimberlite occurrences obtained using broad beam electron microprobe analysis in conjunction with those of lapilli obtained using X-ray fluorescence analysis (major elements) indicate that the composition obtained by applying each method to the same lapilli are indistinguishable. Thus pelletal lapilli too small for XRF analysis were confidently analyzed by EMP, and used to reconstruct the composition of the kimberlite liquid. Kimberlite whole-rock data and pelletal lapilli data both exhibit well-developed, but distinct, compositional arrays in binary plots (Mg versus Si, Ca, C) that intersect at a common Mg content. The kimberlite whole-rock compositional array is assumed to reflect this variation, due to entrainment of variable amounts of xenocrystic mantle. The pelletal lapilli compositional arrays differ systematically

from those of their host kimberlite whole-rocks and reflect the variable modal abundance of carbonate and serpentine. The intersection of the lapilli array with that of the whole-rock array is similar to the carbonate-rich and silica-poor magma compositions obtained via the xenocrystic mantle extraction method.

The carbonate-rich nature of kimberlite magma raises questions regarding the effect of large kimberlite eruptions on Earth's climate; addressing this question is hampered by the fact that there have been no kimberlite eruptions in human history. However, the early Cenozoic experienced at least three short but major hyperthermals associated with disruptions of the global carbon cycle that are coincident with large kimberlite eruptions. The largest among those, the Paleocene-Eocene thermal maximum, was associated with a negative carbon isotopic excursion of ~ 2.5‰ that appears to be best explained by the thermal dissociation of methane hydrates due to an initial period of warming. The cause of the initial warming has been attributed to a massive injection of carbon (CO_2 and/or CH_4) into the atmosphere, however, the source of the carbon has proved to be elusive. The emplacement of a large cluster of kimberlite pipes at ~56 Ma in the Lac de Gras region of northern Canada may have provided the carbon that triggered early warming in the form of exsolved magmatic CO_2. Our calculations indicate that the estimated 900-1,100 Pg of carbon required for the initial ~3 °C of ocean water warming associated with the Paleocene-Eocene thermal maximum could have been released during the emplacement of a large kimberlite cluster. The coeval ages of two other kimberlite clusters in the Lac de Gras field and two other early Cenozoic hyperthermals indicate that CO_2 degassing during kimberlite emplacement is a plausible source of the CO_2 responsible for these sudden global warming events.

Multiple lines of evidence were used in this thesis to constrain the composition of the kimberlite parental magma. Petrographic evidence, xenocrystic extraction models, orthopyroxene assimilation/olivine crystallization models, the geochemistry of olivine's magmatic overgrowth margins, and the geochemistry of the pelletal lapilli all point to a silico-carbonatitic parental magma composition. Acceptance of this silico-carbonatitic nature of kimberlite is being delayed by biases inherent to established science, but once it is achieved, larger questions may be addressed. This thesis thus offers an explanation to the triggering of the PETM, based on the high-carbon nature of kimberlite eruptions, and the synchronous timing of the Lac de Gras kimberlite field and three early Cenozoic hyperthermals. A reaffirmation of scientific values is warranted, even in the age of nano-measurements: unrelenting skepticism of new and old ideas, the judgment of all ideas and arguments on their objective merits, the hierarchy of scale and the need for a holistic approach to science. As scientists, as geologists, it is our responsibility to not only to judge new and challenging ideas on their merits, and not on our prejudices, but to seek out answers, even in the most unforeseen of places.

Résumé

Malgré un accord général parmi les chercheurs de kimberlite sur la plupart des caractéristiques de base de kimberlite, l'Union internationale des sciences géologiques (UISG) considère encore kimberlite indéfini. De plus, une caractéristique fondamentale et d'une importance cruciale de kimberlite est encore âprement débattue: la composition de son magma primaire. Deux écoles de pensée distinctes ont émergé pour expliquer la composition du magma kimberlitic: La première favorise un silicate ultramafique riche en volatil, tandis que l'autre suggère un liquide parental de caractére silico-carbonatitic. Il est incontestable que la kimberlite peut être décrit par deux composantes principales: le carbonate et l'olivine. Malgré la prevalence de carbonate et une absence quasi-complète d`olivine magmatique, la magma parental is souvent supposé d`être d`un caractére silicate ultramafique rich en volatil. L`énorme volume de magmatisme silicate contribue certainement à un préjugé contre l'existence de processus magmatique qui est distinct de la tectonique des plaques, et donc contre l`existence de magma d`une caractère chimique différente. Cette thèse étudie la composition du magma parental de kimberlite, contraignant la composition du magma de kimberlite en utilisant la composition de surcroissances d'olivine magmatiques et la composition de lapilli pelletal de kimberlite. Ensuite, cette thèse illustre les conséquences des éruptions de kimberlite de cette composition sur le climat de la Terre.

Dans un effort d`élucider la question en suspens concernant la composition du magma parental de kimberlite, les excroissances magmatiques des grains d'olivine xénocristaux du kimberlite sont utilisé pour contraindre la composition du magma de laquelle ils ont été cristallisé. La majorité des compositions de base d'olivine sont similaires à celle de l'olivine dans

la lithosphère manteau sous-continental (Fo92 ~ et ~ 3000 ppm Ni), mais il existe deux autres types de compositions moins abondantes. Cependant, la composition de la marge de l'olivine est distinct dans chaque suite de kimberlite, indépendamment de la composition du noyau de l'olivine. Bien que les compositions des marges d'olivine sont unique dans chaque suites de kimberlite, ils varient d'Fo87 à Fo91 entre les suites de kimberlite. Le profile de la composition initiale varie, mais la composition de la marge de l'olivine se stabilise à composition constant de forstorite et en teneurs en Ni. Il est clair qu'un processus ou des processus comparables sont responsables de ces compositions de marge magmatiques similaire, et cela peut fournir des indications de la composition du magma de laquelle ils ont été cristallisé.

Suite à l'utilisation de la preuve directe que des excroissances d`olivine magmatiques fournissent, une approche plus indirecte de contraindre la composition du magma de kimberlite utilise des lapillis pelletaux souvent trouvés dans de la kimberlite. Les lapillis pelletaux ont longtemps été reconnus comme des gouttelettes de magma formé lors de l'éruption d'une variété de suites volcaniques, y compris les kimberlites. Les compositions de lapillis pelletaux de trois occurrences de kimberlite, obtenues en utilisant un microsonde électronique, sont comparé avec des analyses de lapilli obtenue en utilisant la fluorescence aux rayons X (éléments majeurs). Les résultats indiquent que les compositions obtenues par l'application de chaque méthode sur la même lapilli sont indiscernables. Ainsi, les données recueillies auprès des lapillis pelletaux trops petits pour analyze par FRX ont été analyser par microsonde électronique avec confience, et sont utilisées pour reconstruire la composition du liquide parentale de kimberlite. Les analyses de roche-totale de kimberlite et des lapillis pelletaux présentent tous les deux des tendances bien développées, mais distinctes, dans les graphiques binaires (Mg par rapport à Si, Ca, C), et ces tendances se croisent au même contenu de Mg. Les tendances des analyses de roche-totale de kimberlite sont supposées refléter la variation cause par l'entraînement des quantités variables de xénocristaux provenant du manteau. La composition des lapillis pelletaux diffèrent systématiquement de la composition du roche-totale kimberlite hôte et reflètent l'abondance modale variable de carbonate et de serpentine. L'intersection des tendances des lapillis et celle de la roche-totale donne une composition qui est similaire aux compositions magmatiques riches en carbonate et pauvres en silice obtenues par la méthode d'extraction des xénocristaux du manteau.

La nature riche en carbonate du magma kimberlitic soulève des questions concernant l'effet des grandes éruptions de kimberlite sur le climat de la Terre; mais addresser cette question directement est compliqué par le fait qu'il n'y a pas eu d'éruptions de kimberlite dans l'histoire humaine. Cependant, le début du Cénozoïque a connu au moins trois hyperthermals courts mais importants liés à des perturbations du cycle mondial du carbone qui coïncident avec des grandes éruptions de kimberlite. Le plus grand parmi ceux-ci, le maximum thermique Paléocène Eocène, a été associée à une excursion isotopique du carbone négatif de ~ 2,5 ‰ qui semble être mieux expliqué par la dissociation thermique des hydrates de méthane en raison d'une période initiale de réchauffement. La cause du réchauffement initial a été attribuée à une injection massive de carbone (CO2 et / ou CH4) dans l'atmosphère, cependant, la source de carbone est encore inconnu. La mise en place d'un grand groupe de cheminées de kimberlite à ~ 56 Ma dans la région du lac de Gras au nord du Canada ont fourni le carbone qui a déclenché le réchauffement au début de la forme d'exsolvée magmatique CO2. Nos calculs indiquent que l'estimation 900-1,100 Pg de carbone nécessaire pour la première ~ 3 ° C de réchauffement de

l'eau de mer associée avec le maximum thermique Paléocène Eocène aurait pu être libéré au cours de la mise en place d'un grand essaim de kimberlites. Les contemporaines âge de deux autres groupes de kimberlite dans le domaine du lac de Gras et deux autres hyperthermals Cénozoïque début indiquent que le dégazage de CO2 lors de la kimberlite est une source plausible de CO2 responsables de ces événements soudains réchauffement de la planète.

Plusieurs éléments de preuve ont été utilisés dans cette thèse pour contraindre la composition du magma parental du kimberlite. Preuve pétrographique, les modèles d'extraction xénocristaux, les modèles d`assimilation d`orthopyroxène / cristallisation d'olivine, la géochimie des marges de surcroissances d'olivine, et la géochimie des lapillis pelletaux pointent tous vers une composition silico-carbonatitique pour la magma parentale. L'acceptation de la nature silico-carbonatitique de kimberlite est retardée par des biais inhérents à la science établie, mais une fois qu'il est atteint, les grandes questions peuvent être adressées. Cette thèse propose ainsi une explication au déclenchement de la PETM, basé sur la nature des éruptions de kimberlite, qui ont une haute teneur de carbone, et la synchronization des ages du champ de kimberlites du lac de Gras et trois hyperthermals Cénozoïque. Une réaffirmation des valeurs scientifiques est justifiée, même dans l'ère des nano-mesures: le scepticisme implacable d'idées nouvelles et anciennes, le judgement de toutes les idées et les arguments sur leurs mérites objectifs, la hiérarchie de l'échelle et la nécessité d'une approche holistique de la science. Comme scientifiques, comme géologues, il est notre responsabilité de ne pas seulement juger les idées nouvelles et stimulantes sur leurs mérites, et non sur nos préjugés, mais à chercher des réponses, même dans le plus imprévu des lieux.

Acknowledgements

In 2006, I arrived in at McGill University in Montréal and was given a set of rocks, thin sections and bulk-rock data on the Foxtrot suite of kimberlites from northern Québec, these were to form the basis of my Master of Science thesis. My immediate reaction was astonishment to all the carbonate I observed in the thin sections. What was so much pristine carbonate doing in a deep mantle derived rock? Even as my MSc. came to fruition, the excitement and astonishment never left my approach to kimberlite. Late in my MSc. work, Don Francis and I were sitting on a ledge above a new discovery in the Foxtrot field eating our lunch and enjoying a warm sunny break, when he asked what my thoughts were regarding doing a PhD study into the origins of kimberlite. My response was that I would absolutely sign up for such a study.

I would like to primarily acknowledge my supervisor Don Francis who gave me the opportunity to study this unique set of compositions and thank him for his full support and guidance throughout this project. I would also like to thank Bill Minarik and Boswell Wing for their scientific input as members of my advisory committee, and special thanks to Bill Minarik for his work obtaining bulk-rock composition of my samples. I would also like to extend a very special thank you to Lang Shi for his endless assistance when using the Electron Microprobe; Dr. Al Mucci, Dr. Eric Galbraith and Dr. Dirk Schumann for their scientific input regarding Earth's paleoclimate.

My time at McGill was not only an academic endeavor; the City of Montréal provided a vast array of cultural experience that will stick with me to the end of days. All of Montréal is thanked for such a great experience. There is one very special Montrealer that needs to be recognized, Stephanie Nichols. Stephanie helped with my academic endeavors as well as opening cultural doors as well. Through deep philosophical discussions, cultural experiences and spiritual growth, Stephanie is irreplaceable as a partner. Her help and assistance with the boring doldrums of writing, grammar, spelling, structure and the importance of the word "the" is greatly appreciate.

As a final hommage to Don Francis:

"We soar through the cosmos aboard a rock tethered to a star."

Table of Contents

List of Tables

Table

Lists of Figures

Figure

List of Appendices

Contribution of authors

The manuscripts included in this thesis are authored by Michael V. Patterson (MVP) and Don Francis (DF). The original ideas of this thesis topic were conceived by both MVP and DF during many discussions and field excursions during my MSc. (2006-2009). Preparation for field excursions to the Foxtrot and Buffalo Head Hills as well as sample collection trips to kimberlite core facilities in both Vancouver and Yellowknife was completed by MVP. Sample collection in the field was carried out by both MVP and DF. Preparation of samples for petrographic thin sections and geochemical analysis was done by MVP. The data analysis and writing of the manuscript and thesis was done by MVP, with the guidance of DF.

The current status of the material contained in the thesis is as follows:

CHAPTER 2: SUBMITTED TO LITHOS - Patterson, Michael and Francis, Don. The implications of magmatic margins on xenocrystic olivine kimberlite magma composition.

CHAPTER 3: IN PREPARATION FOR LITHOS - Patterson, Michael and Francis, Don. Constraining the compositions of kimberlite magma using pelletal lapilli.

CHAPTER 4: PUBLISHED - Patterson M. V., and D. Francis (2013) Kimberlite eruptions as triggers for early Cenozoic hyperthermals, Geochem. Geophys. Geosys., 14, 448 – 456, doi:10.1002/ggge.20054.

CHAPTER 1

Philosophical shift in the intellectual approach to unravelling the *'Mythology'* of kimberlites

General Introduction

In *The Descent of Man* (1871), Charles Darwin stated;

> *"... ignorance more frequently begets confidence than does knowledge: it is those who know little, and not those who know much, who so positively assert that this or that problem will never be solved by science".*

Of course, Darwin was referring to the debate on the origins of man. This characterization, however, applies to many of the outstanding questions in the geosciences, one of which remains: What is kimberlite? Despite general agreement among kimberlite researchers on many of the basic characteristics of kimberlite, the International Union of Geological Sciences (IUGS) still considers kimberlite undefined. Furthermore, a fundamental and crucially important characteristic of kimberlite is still fiercely debated: the composition of its primary magma. Although there has been decades-worth of work on this subject, the composition of kimberlite magma remains an outstanding question. This is exemplified by the recent International Kimberlite Conferences (10th – February, 2012 in Bangalore, India; 9th – August, 2008 in Frankfurt, Germany; 8th – July, 2003 in Victoria, Canada), at which this issue continued to be addressed and vigorously debated.

Two distinct schools of thought have emerged to explain the composition of kimberlite magma. The first favors a volatile-rich ultramafic silicate melt (Price et al., 2000; Becker & le Roex, 2006a; Kopylova et al., 2007), while the other suggests a silico-carbonatite parental melt (Dawson & Hawthorne, 1973; Kamenetsky et al., 2007; Nielsen & Sand, 2008; Francis & Patterson, 2009; Patterson et al., 2009; Russell et al., 2012). The dynamic at play between these two schools of thought can perhaps be best understood by considering the philosophy of science. In his book *The Structure of Scientific Revolutions*, Thomas S. Kuhn discusses the philosophy of science and how a community’s current philosophy shapes which new theories are acceptable. One of his basic tenets is that a scientific community cannot practice its trade without some set of established beliefs and that these beliefs form the foundation of the "educational initiation that prepares and licenses the student for professional practice." Kuhn refers to “normal science” as "predicated on the assumption that the scientific community knows what the world is like" and to this end, "normal science often suppresses fundamental novelties because they are necessarily subversive of its basic commitments." New ideas that lie outside the currently-accepted paradigms require the re-evaluation of prior facts and the reconstruction of prior assumptions. This re-evaluation process is quite difficult and faces strong resistance by the established community, even if the evidence supporting the new idea is compelling.

The unifying paradigm within which the geosciences currently operate is the theory of plate tectonics. A truism resulting from geology’s unifying theory is that volcanism primarily occurs at localities where the mechanisms of plate tectonics are best observed: mid-oceanic spreading ridges and subduction zones. In the simplest terms, volcanism at these sites is caused either by perturbation of the pressure-temperature regime or introduction of fluids to the upper mantle. These processes almost inevitably produce partial melts that are silicate in character. Most volcanism that occurs away from the type localities also complies with the silicate nature that is expected of mantle-derived magmas, i.e. continental flood basalts. I believe that this overwhelming volume of silicate magmatism has led to a bias against the existence of any magmatic process different in chemical character and divorced from plate tectonics. This bias is part of the set of established beliefs against which the "normal science" judges the merit of any idea. In the case of kimberlite, it is this bias which fuels the school of thought that kimberlite magmas must be volatile-rich ultramafic silicate melts.

In our increasingly micro- or nano- scaled world, science can often suffer from becoming myopic in its views. In our science, geology, we strive to extract the minutest morsel of data from our rocks and can now do so with amazing accuracy and precision. One of the pitfalls of this approach is that we often do not comprehend, or sometimes do not even attempt to comprehend, the context of our objects of study. Everything necessary to understanding the majority of characteristics of a rock is actually visible to the human eye. This does, however, require that we look at the outcrop from which the sample originates; the formations that are above, below and cross-cut the formation from which our sample is extracted; the structural geology of the area; the rock itself and its mineralogy, both with the naked eye and with the petrological microscope. If done properly, at the end of the foregoing investigation, our observations will have constrained the type of rock and, in general, the chemistry of the sample, its age and how it came to be in the location we found it. Then and only then do we have sufficient context that will enable us to confidently interpret the information that is gathered at the micro- and nano- scales.

My impression of kimberlite was established when I first viewed it through a petrographic microscope and I asked "what is all this carbonate doing in a mantle-derived rock?" My initiation into geology had also asserted that the physical world must obey the plate tectonics paradigm, and therefore mantle-derived rocks should be silicate in nature. If I were to have adhered dogmatically to this paradigm, I would have attempted to justify how such a volume of carbonate could exist in a mantle-derived silicate melt. However, never known to be much of a conformist, I allowed myself to fall down the proverbial rabbit hole. I chose to study kimberlite without imposing onto it any pre-conceived notions of what it ought to be: to start at the beginning and follow the evidence, in context, where it lead. As a result of this approach, I found myself butting up against the “normal science,” which still wants to believe that everything from the mantle is silicate in character, despite what the evidence suggests. These dogmatists, who suffer from a failure of the imagination, speak from a position of ignorance when they say that science will not be able to solve the problem otherwise and therefore prefer to assert that kimberlite cannot be defined.

I agree that the petrogenesis of kimberlite does have many unique and intricate, often confusing and possibly contradictory characteristics and therefore its magma composition will reflect this exquisite uniqueness. Despite the foregoing, it is indisputable that kimberlite can be described by two principal components: carbonate and olivine. James Hutton’s principle of uniformitarianism provides the basis to state that any description of kimberlite magma cannot betray the absolute truth that the composition of kimberlite rocks is controlled inextricably by carbonate and olivine. Keeping to first-order principles and an approach unhampered by obstructionist biases, the composition of kimberlite magma was investigated. This thesis constrains the composition of kimberlite magma by using the composition of magmatic olivine overgrowths and the composition of kimberlite pelletal lapilli, and then illustrates the implications of kimberlite eruptions of that composition on Earth’s climate.

References

Becker, M. & le Roex, A. P. (2006a). Geochemistry and petrogenesis of South African isotopically transitional kimberlites located on and off the Kaapvaal Craton. *Lithos*.

Dawson, J. B. & Hawthorne, J. B. (1973). Magmatic sedimentation and carbonatitic differentiation in kimberlite sills at Benfontein, South Africa. *Journal of the Geological Society* **129**, 61-85.

Francis, D. & Patterson, M. (2009). Kimberlites and aillikites as probes of the continental lithospheric mantle. *Lithos* **109**, 72-80.

Kopylova, M. G., Matveev, S. & Raudsepp, M. (2007). Searching for parental kimberlite melt. *Geochimica et Cosmochimica Acta* **71**, 3616-3629

Kamenetsky, V. S., Kamenetsky, M. B., Sharygin, V. V., Faure, K. & Golovin, A. V. (2007). Chloride and carbonate immiscible liquids at the closure of the kimberlite magma evolution (Udachnaya-East kimberlite, Siberia). *Chemical Geology* **237**, 384-400.

Nielsen, T. F. D. & Sand, K. K. (2008). The Majuagaa kimberlite dike, Maniitsoq region, West Greenland: Constraints on an Mg-rich silicocarbonatitic melt composition from groundmass mineralogy and bulk compositions. *Canadian Mineralogist* **46**, 1043-1061.

Patterson, M., Francis, D. & McCandless, T. (2009). Kimberlites: Magmas or mixtures? *Lithos* **112**, 191-200.

Price, S. E., Russell, J. K. & Kopylova, M. G. (2000). Primitive magma from the Jericho Pipe, NWT, Canada: constraints on primary kimberlite melt chemistry. *Journal of Petrology* **41**, 789-808.

Russell, J. K., Porritt, L. A., Lavallee, Y. & Dingwell, D. B. (2012). Kimberlite ascent by assimilation-fuelled buoyancy. *Nature* **481**, 352-356.

CHAPTER 2

The implications of olivine magmatic margins for kimberlite magma composition

Abstract

Despite years' worth of studies, the composition of the parental magma of kimberlite remains an outstanding question. The presence of magmatic overgrowths on xenocrystic olivine grains from the Nikos and Nanuq Kimberlite (northern Canada) present an avenue to constrain the composition of the magma from which they crystallized. The majority of the olivine core compositions (Type 1) in both the investigated suites are similar to that of olivine in the sub-continental lithospheric mantle (~Fo_{92} and Ni ~3,000 ppm). There are two other types of olivine core compositions that are less abundant and have lower forsterite ($Fo_{84\text{-}86}$) contents than Type 1 olivine cores. Type 2 olivines have high Ni contents (~2,800 ppm), whereas Type 3 olivines have relatively low Ni contents (~1,000 ppm). Three types of zoning patterns can be identified in the olivine margins: Type 1 cores always have margins with lower forsterite and Ni contents that decrease outward, Type 2 cores have margins with higher forsterite and Ni contents that decrease outward, whereas Type 3 cores also have margins with higher forsterite contents, but Ni first increases within tens of microns of the boundary to levels similar to that of the margins of Type 1 and 2 cores. Within individual kimberlite suites, the magmatic margins converge to similar compositions. The compositions of the olivine margins do vary from Fo_{87} to Fo_{91} between different kimberlite suites. The forsterite content changes sharply at the boundary between the olivine margins and core composition, but remains constant across the margin. Whereas, the Ni content can either initially increase or decrease immediately outward from the olivine core, but always converges to a similar decreasing outward pattern. It is possible to constrain the composition of the kimberlite parental magma by removing the xenocrystic component from kimberlite bulk-rock compositions until the residue would crystallize olivine with the composition of the margins assuming the $k_{D(Fe/Mg)}$ for olivine crystallization in kimberlite magmas is ~0.3, similar to that of basalts. However, the constant forsterite content of the margin indicates that the Fe/Mg of the liquid remains constant, therefore the Fe/Mg content of that liquid must be buffered. Conversely, the nickel content of the margins decreases significantly outwardly, thus the nickel content of the liquid must also decrease. The composition of the magmatic olivine margins are best explained by a concomitant orthopyroxene assimilation and olivine crystallization model with a one-to-one molar ratio. The different compositions exhibited by magmatic olivine margins Fo_{87-91} in different kimberlite suites indicate that the composition of their parental magmas must also be distinct. All the calculated parental magmas are, however, rich in carbonate (>50%) and therefore are silico-carbonatites.

Introduction

Although kimberlite magmas are volumetrically minor compared to most magma types found on Earth, the composition(s) of their parental magmas remains controversial and much debated. The importance of kimberlite magmas lies in the information they carry as probes of the cratonic upper mantle; they not only carry xenoliths of the mantle from depths of over 150 km (Kennedy & Kennedy, 1976; Ringwood *et al.*, 1992; Mitchell, 1995; Girnis, 2005), but their compositions provide important constraints on their source regions (Francis & Patterson, 2009). Despite the large number of publications dealing with the nature of kimberlite magmas, two fundamentally different proposals have emerged Older studies favor a volatile-rich ultramafic silicate melt (Price *et al.*, 2000; Becker & le Roex,2006a; Kopylova *et al.*, 2007), while many more recent studies suggest that kimberlites are silico-carbonatite magmas (Dawson & Hawthorne, 1973; Kamenetsky *et al.*, 2007; Nielsen & Sand, 2008; Francis & Patterson, 2009; Patterson *et al.*, 2009; Russell *et al.*, 2012).

In an effort to resolve these two opposing views regarding the composition of kimberlite magma, we take a new approach using the chemical zonation found in the magmatic margins of olivine xenocrysts, a feature found in many kimberlite suites (Moore, 1988; Kamenetsky *et al.*, 2007; Brett *et al.*, 2009; Arndt *et al.*, 2010). In this paper, we show that the zonation in the magmatic olivine margins can be used to constrain the evolving composition of the melt from which they crystallized. We use detailed electron microprobe traverses across the zoned margins of olivine grains from the Nikos and Nanuq kimberlites (northern Canada), in conjunction with previous studies of mantled kimberlite olivine xenocrysts, to constrain the composition and the early crystallization of kimberlite magma. We demonstrate that the compositional variation in the olivine margins cannot be explained by the crystallization of olivine alone, but requires the assimilation of orthopyroxene by CO_2-rich magma with a silico-carbonatite composition.

Searching for the composition of kimberlite magma

An axiom of igneous petrology is that the compositions of crystal-poor volcanic rocks approximate liquid compositions, and that the phenocrysts present are in equilibrium with that liquid. Kimberlites typically consist of an assemblage of anhedral ultramafic minerals (primarily olivine) set in a fine-grained matrix of calcite and/or dolomite with accessory minerals such as apatite, spinel, phlogopite and perovskite. Previous studies (le Roex *et al.*, 2003; Kopylova *et al.*, 2007; Mitchell, 2008) suggested that two distinct types of olivine grains exist in kimberlites, xenocrystic grains and 'fine-grained phenocrysts'. Recent studies (Kamenetsky *et al.*, 2007; Nielsen & Sand, 2008; Brett *et al.*, 2009; Patterson & Francis, 2009; Patterson *et al.*, 2009; Arndt *et al.*, 2010), however, have demonstrated that most olivine grains in kimberlite are xenocrystic, regardless of their size or shape, and are presumed to be derived via the disaggregation of lithospheric mantle. A fundamental consequence of this observation is that the bulk-rock compositions of kimberlite cannot be used as a proxy for their magma composition. Consequently, a common approach to constraining the composition of kimberlite magma is to attempt to remove the xenocrystic component from the bulk-rock (Kopylova *et al.*, 2007; Kjarsgaard *et al.*, 2009; Patterson *et al.*, 2009). The amount of xenocrystic material removed is based on the estimated percentage of the total olivine that is xenocrystic, which varies between 30 to 100 %, depending on the study. Furthermore, since the composition of sub-lithospheric mantle is almost identical in every craton on Earth, any regional differences in the composition of kimberlite magmas is likely due to the carbonate-rich melts rising from the asthenosphere (Francis & Patterson, 2009).

In the last decade, the calculated compositions for kimberlite magma using the xenocrystic mantle extraction method fall into two categories; volatile-rich ultramafic silicate melts or silico-carbonatite melts (table 2-1). The calculated volatile-rich ultramafic silicate melts (Price *et al.*, 2000; le Roex *et al.*, 2003; Harris *et al.*, 2004; Becker & Le Roex, 2006b; Kopylova *et al.*, 2007; Kjarsgaard *et al.*, 2009) are characterized by high MgO contents (25-34 wt%) and low CO_2 contents (5-15 wt%). In contrast the calculated silico-carbonatite melts (Nielsen & Sand, 2008; Patterson *et* al., 2009) have low SiO_2 (18-24 wt%) and MgO (15 wt%) contents and high

CO_2 contents (17-21 wt%).

The high MgO compositions proposed in volatile-rich ultramafic silicate melts scenario, however, are problematic in light of experimental evidence from studies (Parman *et al.*, 1997; Canil & Bellis, 2008; Sparks *et al.*, 2009) that indicate MgO-rich compositions require high liquidus temperatures (>1350 °C) that are inconsistent with the lower estimated kimberlite magma temperatures (<1200 °C; (Mitchell, 2008)). Furthermore, melting experiments conducted on MgO-rich compositions (25-35 wt%) indicate that the residual melts do not have compositions that are consistent with the groundmass mineralogy of kimberlites (Sparks *et al.*, 2009). These studies have demonstrated that melts formed near the mantle solidus are carbonatitic and only develop silica-rich kimberlite affinities at higher temperatures, for example at 1460-1500 °C for 6 GPa (Dalton & Presnall, 1998). Experiments at 100 and 200 MPa in the CaO-MgO-SiO_2-H_2O-CO_2 system indicate that carbonatitic melts can exist to temperatures as low as 700 °C (Wyllie & Tuttle, 1960; Ootto & Wyllie, 1993).

Olivine Margins

The presence of zoned margins on olivine in kimberlite has been recognized for some time (Skinner & Clement, 1979; Bailey, 1984). Moore (1988) first used the composition of such margins to conclude that the majority of olivines in kimberlite are cognate phenocrysts, although numerous subsequent studies have shown this conclusion unlikely due to the high forsterite content (>Fo_{92}) of olivine in kimberlite (Kamenetsky *et al.*, 2007; Brett *et al.*, 2009; Patterson *et al.*, 2009; Arndt *et al.*, 2010). A number of studies of olivine in kimberlite have demonstrated that the olivine rims are magmatic with forsterite contents ranging between 87 and 91 (Moore, 1988; Kamenetsky *et al.*, 2007; Brett *et al.*, 2009; Arndt *et al.*, 2010). These forsterite contents are too low to be in equilibrium with the proposed MgO-rich silicate magmas if a $k_{D(Fe/Mg)}$ of 0.3 is used. There is, however, a large range (0.15 to 0.80) in the estimated $k_{D(Fe/Mg)}$ in CO_2-rich systems (Canil & Bellis, 2008). Furthermore, the foregoing assumes that all the iron in parental kimberlite magma would be Fe^{2+}. The presence of any Fe^{3+} would lower the Fe^{2+}/Mg ratio of the magma and require a higher $k_{D(Fe/Mg)}$ to crystallize the olivine margin. A number of studies have demonstrated that the cratonic mantle in which kimberlites are sourced is relatively reduced, with oxygen fugacities as low as -3 to -5 $\Delta\log fO_2$NNO (Fedortchouk & Canil, 2004; Canil & Bellis, 2007). It seems likely that the fO_2 of kimberlite would also be relatively reduced since their xenolith load requires that they have interacted extensively with the cratonic mantle and therefore have a low Fe^{3+}/Fe(total). However, the fO_2 estimations for kimberlite magmas are difficult to constrain and often range over many orders of magnitude (NNO -5 to NNO +6; Canil & Bellis, 2007), the largest extreme observed in any magma type. In consideration of the aforementioned difficulty, we do not attempt to incorporate fO_2estimations into our model and assume that kimberlite magmas are relatively reduced, with low Fe^{3+}/Fe(total).

In this study, we use the compositions of olivine margins, and the bulk-rock composition of the Nikos and Nanuq kimberlite rocks of Northern Canada, to estimate the composition of the kimberlite magma from which they crystallized. In addition, we use the results of previous studies (Udachnaya – Kamenetsky *et al*., 2007; Diavik – Brett *et al*., 2009; and Orapa and Benfontien– Arndt *et al*., 2010) to estimate the compositions of the kimberlite magma in other suites.

Methods

Bulk-rock compositional data was collected on blocks (~100–400 cm^3) cut from the freshest kimberlite rocks available to minimize the effect of alteration and/or contamination. These blocks were then crushed to approximately 10 mm and fresh inclusion-free fragments were picked using a binocular microscope to avoid xenolith contamination and serpentinization. The samples were dried at 60 °C, pulverized to 150 µm using an alumina ring -and-puck grinder and analyzed for whole rock geochemistry by X-ray fluorescence using fused bead (major elements) and pressed-pellet techniques (select trace elements) developed at McGill University. Olivine mineral analyses were carried out using WDS (wave dispersive spectrometry) on a JEOL 8900EMP (electron microprobe) at McGill University, Montréal, Canada. Two calibration setups where used, the first used a broad beam (5 µm) to characterize the composition of the olivine cores and margins, the second used a smaller beam size (2 µm) to analyze transects from the olivine cores across the olivine margins. For the first setup, an accelerating voltage of 15KeV (20 KeV for Ni) and a beam current of 60 nA with a 5 µm spot size were used. Fe, Mg and Ti were measured with peak counting times of 10s; Si with 20s; Ca with 40s; and Ni and Mn with 120 s. In the second setup, an accelerating voltage of 15KeV (20 KeV for Ni) and a beam current of 60 nA with a 2 µm spot size was used at a 5 µm spacing. Fe, Mg and Ti were measured with peak counting times of 10s; Si with 20s; Ca with 40s; and Ni and Mn with 60 s. In-house natural and artificial silicate and oxide standards were used for both calibration setups.

Geological Setting

Nikos kimberlite

The Nikos kimberlites belong to the Somerset Island kimberlite field that is situated within the Innuitian tectonic province on the northern margin of the North American continent (Trettin *et al.*, 1972; Frisch & Hunt, 1993; Pell, 1993). The local stratigraphy comprises middle Proterozoic to early Paleozoic sedimentary sequences that overlie the crystalline Precambrian basement of the Boothia Uplift (Steward, 1987). The Precambrian basement represents a northward salient of the Canadian Shield that was deformed and faulted in the late Proterozoic to early Paleozoic, possibly related to compression associated with the Caledonian Orogeny in northern Europe and Greenland (Okulitch & Trettin, 1991). Granulite facies gneisses from the crystalline basement of the Boothia Uplift yield zircon dates between 2.5 and 2.2 Ga for their protoliths, while Sm–Nd model ages of 3.0 to 2.2 Ga suggest the presence of reworked Archean crustal material in these gneisses (Frisch & Hunt, 1993).

U-Pb dating of perovskite indicates Cretaceous emplacement ages between 90 to 105 Ma for the Somerset Island kimberlites (Heaman, 1989; Smith *et al.*, 1989). An Rb-Sr bulk-rock isochron for the Nikos kimberlites yields an emplacement age of 97 ± 17 Ma, in good agreement with the U-Pb ages. Kimberlite emplacement coincided with major compressive deformation in the southeastern Arctic Islands induced by rifting that preceded sea-floor spreading in the Labrador Sea and Baffin Bay, and the associated rotation of Greenland away from the North American continent that began in the early Cretaceous (Okulitch & Trettin, 1991). Early field work and petrographic studies have shown that the majority of the Somerset kimberlites are brecciated diatremes or hypabyssal root zones (Mitchell & Meyer, 1980), consisting of fragments of kimberlite host, country rock, and mantle-derived xenocrysts and xenoliths. Magmatic kimberlite is rare on Somerset Island (Mitchell & Meyer, 1980; Mitchell, 1986), however, the Nikos kimberlites (Pell, 1993) consists of three individual pipes containing magmatic kimberlite that outcrop along a steep cliff on the eastern coast of Somerset Island (Schmidberger & Francis, 1999).

Nanuq kimberlite

The Nanuq property lies within the Rae domain of the Western Churchill Craton, which is dominated by Neoarchean (2.8-2.5 Ga) amphibolite to granulite grade granitoid gneisses and greenstone belts that are overlain by 2.45-1.75 Ga volcano-sedimentary sequences, and intruded by 1.83 and 1.75 Ga granitic suites(Pell *et al.*, 2009). The Nanuq property occurs at the intersection of the Wager Bay Shear Zone, a major east-west structure, and the Keewatin Arch, a major long-lived crustal uplift along which kimberlites at Rankin Inlet, Repulse Bay and on Melville Peninsula also occur. Although three kimberlite bodies (Naturalik, Kayuu and Tuklik) have been sampled, only the Naturalik pipe contains significant amounts of magmatic kimberlite. Intersections in one vertical and five inclined drill cores have been used to construct a three dimensional model of the pipe morphology that suggests the existence of a single conduit with a steep sided crater that shallows to the South (Pell *et al.*, 2009). The pipe is filled by two contrasting textural varieties: coherent magmatic kimberlite and subordinate fragmental volcaniclastic kimberlite. Preliminary U-Pb isotopic analyses performed on perovskite separated from one sample of Naturalik and one of Kayuu yielded ages of 79.6 ± 5.2 Ma and 70.4 ± 5.4 Ma, respectively (Pell *et al.*, 2009). These data are consistent with palynology results and reveal that the Nanuq kimberlites are the youngest kimberlites documented in the Churchill province (Heaman *et al.*, 2003; Pell *et al.*, 2009).

Petrography

Petrographic observations indicate the southernmost of the three individual Nikos pipes (NK3) is characterized by a non-fragmental, coherent texture that has been interpreted to represent magmatic kimberlite (Schmidberger & Francis, 1999). The magmatic kimberlite exhibits a macrocrystic texture of olivine in a microcrystalline matrix rich in carbonate with minor amounts of phlogopite, garnet and spinel. The modal abundance of olivine is approximately 40%. Olivine grains are primarily <15 mm in size and exhibit rounded, irregular, and euhedral habits. Although serpentinization is pervasive in olivine of all sizes, many of the smaller grains have fresh cores surrounded by serpentine. The microcrystalline groundmass consists primarily of calcite (40%) with minor amounts of perovskite, apatite and dolomite. Calcite occurs as aggregates of tabular euhedral crystals or as sub-parallel laths, which flow around large olivine crystals, indicating their primary magmatic nature.

The Nanuq kimberlite pipes contain a non-fragmental, coherent textured kimberlite that has been interpreted to represent magmatic kimberlite (Pell *et al.*, 2009). Fresh samples of magmatic kimberlite contain more olivine (50-60 %) than those of the Nikos kimberlite. Although serpentinization is common in the Nanuq kimberlite, it is less pervasive than that found in the Nikos kimberlite. The Nanuq magmatic kimberlite exhibits a macrocrystic texture comprising larger olivines (<15 mm) set in a microcrystalline carbonate matrix with abundant apatite, and minor amounts of phlogopite and spinel. Locally, where carbonate content is low, significant monticellite is present (15-20 %) in the matrix. Olivine primarily occurs as rounded to irregular-shaped larger grains (>2 mm) and varies to smaller rounded to euhedral grains.

Although both the Nikos and Nanuq kimberlite suites have similar olivine core compositions (~Fo_{92}), their magmatic rims converge to different compositions (~Fo_{89} and ~Fo_{90} respectively). The cores of the olivines are typically 100's of microns in size, whereas the widths of their margins typically measure 10's of microns. The boundary between the core and margin is sharp when observed in electron backscatter images. The shapes of the cores are commonly rounded or irregular. Although serpentinization typically truncates the olivine margins towards the outer edge of grains, it appears that the margin were continuous before alteration (figure 2-1). Typically, when viewed as a whole grain (i.e. core, margin and alteration together), these olivines have a relatively euhedral shape. The similarity of the rounded habits of the olivine cores to those of xenocrystic olivine, and their high forsterite contents (~Fo_{92} suggests that they are xenocrysts. The euhedral habitsof the olivine margins suggest that they represent magmatic overgrowths.

Electron Microprobe Analysis

High precision EMP analyses of olivine grains in the Nikos kimberlite indicates that three types of cores are present (figure 2-2): (1) high forsterite (~Fo_{92}) and high Ni (~2500 ppm), (2) low forsterite (~Fo_{82-84}) and low Ni (~1000 ppm), (3) low forsterite (~Fo_{84}) and high Ni (~2000 ppm). Type 1 olivine cores comprise >80% of all analyzed olivine grains in the Nikos kimberlite, whereas Types 2 and 3 represent <20%; although the latter two are over - represented because we deliberately searched for reversely-zoned grains. EMP analyses of olivine in the Nanuq kimberlite indicate that only Type 1 cores are present (figure 2-2) with high forsterite (~Fo_{92}) and high Ni (~2700 ppm) contents similar to the Type 1 cores in the Nikos kimberlite.

Regardless of the olivine core compositions, the olivine margins are characterized by relatively constant forsterite content (Nikos – $Fo_{87\text{-}88}$ and Nanuq – $Fo_{90.5\text{-}91.5}$; figure 2-3). Ni is more complicated, but is radially zoned in all cases. Margins on Type 1 olivine cores from the Nikos kimberlite have an initial sharp decrease in Ni content and followed by a slower outward decrease (~2000-800 ppm; figure 2-3). In contrast, margins on Type 1 olivine cores from the Nanuq kimberlite exhibit an initial outward increase in Ni contents, followed by a rapid outward decrease in (within ~25 µm) and then develops a slower outward decrease, similar to the pattern exhibited by that of the Nikos data (~3000-900 ppm; figure 2-3). The variation of the Ni contents in margins developed on Type 2 olivine cores exhibit a similar pattern as those developed on Type 1 olivine cores (~1000-800 ppm; figure 2-3).

All types of olivine cores are homogeneous within individual grains in terms of forsterite, Ni, and Ca content (figure 2-3). The majority of the Nikos, and all of the Nanuq olivines, have Type 1 cores with restricted core compositions of $Fo_{92\pm0.5}$. The low forsterite ($Fo_{82\text{-}84}$) Type 2 and 3 olivine cores in the Nikos kimberlites are also internally homogeneous in composition Type 2 olivine cores have higher Ni contents (~2500±250 ppm), similar to Type 1 cores, while Type 3 cores have lower Ni contents (~800-900 ppm). In all core types, the Ca content is very low, <0.05 wt%.

The boundary between the olivine cores and the margins appears as a step function in terms of Fe/Mg in all olivine grains, regardless of the olivine core composition. The forsterite content changes sharply at the boundary between core and margin (within 10 µm) to a lower but constant forsterite content across the margin (Nikos – Fo_{87-88} and Nanuq – $Fo_{90.5-91.5}$). Ni exhibits a similar initial sharp change (decrease in Nikos but increase in Nanuq), however in both the Nikos and Nanuq margins then smoothly decreases outwards across the margin. Nickel profiles for the Nanuq zoned olivine margins differ from those of the Nikos olivine in that the Ni content increases by 200-500 ppm within the first 20 µm of the margin, but then decreases across the olivine margin as in the Nikos margins. Although the Ca content of the magmatic olivine margins is somewhat variable, it is approximately double (>0.5 wt%) that of the olivine cores(<0.3 wt%).

Discussion

The fact that the majority of the olivine core compositions from both the Nikos and Nanuq kimberlite suites are un-zoned and virtually identical (Fo_{92}, Ni ~ 3000 ppm and low Ca <0.3 wt%) to that of cratonic mantle olivine is consistent with the majority of the olivine in kimberlite being xenocrystic (Brett *et al.*, 2009; Patterson *et al.*, 2009; Arndt *et al.*, 2010). The low forsterite olivine cores, however, are more enigmatic, but similar olivines have previously been suggested to be part of the megacryst mineral suite common to kimberlites (Gurney *et al.*, 1979). Arndt et al (2010) emphasized that the low-Fo olivines may not be xenocrysts from normal lithospheric peridotite, but may instead be derived from dunite composed of olivine with a range of forsterite contents. That being said, the origin of the relatively minor low forsteritic olivine cores is outside the scope of this paper.

The sharp changes in forsterite, Ni and Ca contents at the boundary between the olivine core and their margin indicate that the margins and cores formed through different processes. The very low calcium contents in both high and low forsteritic olivine cores suggests that all the cores are mantle-derived, whereas the higher calcium contents of the olivine margins, and their convergent compositions, indicate that the margins are magmatic overgrowths. The constant forsterite content of the olivine margins of a given kimberlite suite, regardless of core type, suggests that the composition of the olivine margins is a function of that suite's magma composition, and that this composition is buffered in terms of Mg and Fe. The forsterite contents of the olivine margins for the Nikos and Nanuq kimberlite, however, are very different -Fo_{87-88} and $Fo_{90.5-91.5}$, respectively. The compositional profiles seen in the margins of Nikos and Nanuq olivine are also observed in other kimberlite suites (Moore, 1988; Kamenetsky *et al.*, 2007; Brett *et al.*, 2009; Arndt *et al.*, 2010), with each suite being characterized by olivine margins with distinct forsterite contents (Orapa -Fo_{87}, Udacnaya -Fo_{89}, Diavik -Fo_{91}, and Benfontien -Fo_{89} respectively). The compositional variation of Ni at constant forsterite content across olivine margin (figure 2-3) is enigmatic, since Ni content is typically positively correlated with forsterite content in olivine, as is evident in olivine phenocrysts from basaltic rocks (Francis, 1985). In contrast, figure 2-3 clearly illustrates that the forsterite contents in the olivine margins remains constant as Ni decreases systematically outwards. The initial sharp increase or decrease in Ni contents at the boundary between the olivine cores and margins, followed by a gradual decrease outwards (figure 2-2) might represent a diffusion profile, but this would suggest that the diffusion of Fe and Mg is faster than that of Ni. Recent experimental work on the diffusion of Ni in olivine indicates, however, that the diffusion rate for Mg, Fe, and Ni are similar (Petry *et al.*, 2004; Qian *et al.*, 2010). This suggests that magmatic crystallization rather than diffusion was responsible for the composition profiles of the olivine margins. In such an interpretation, the constant forsterite content of the magmatic margins reflects the Fe/Mg ratio of the kimberlite magma.

A common approach to constraining the composition of kimberlite parental magma is the ‘xenocrystic mantle extraction method’ (XMEM). This method involves the mathematical removal of a mantle ‘contaminant’ from bulk kimberlite compositions in order to obtain an estimate of the composition of their parental magma. This approach is beset with difficulties, not the least of which is how much xenocrystic material to remove and of what composition. Although the proportion of xenocrystic to phenocrystic olivine in kimberlite is still debated, there is general agreement that the xenocrystic olivine represents the disaggregation of cratonic mantle. The absence of xenocrystic mantle orthopyroxene in kimberlite has been attributed to its instability in hydrous carbonate-rich fluids (Arndt, 2003; Mitchell, 2008; Francis & Patterson, 2009), and silica-undersaturated magmas (Luth, 2009) in general, and is consistent with orthopyroxene having been assimilated by the kimberlite magma. The possibility of orthopyroxene assimilation by kimberlite magmas has been recognized since its instability in carbon-rich hydrous magmas was first demonstrated (Eggler, 1973; Edgar & Charbonneau, 1993; Ulmer & Sweeney, 2002; le Roex *et al.*, 2003). An investigation of olivine margin compositions in the Diavik kimberlite suggests that the latent heat released as olivine crystallizes provides the latent heat required to assimilate the orthopyroxene (Brett *et al.*, 2009). The Diavik kimberlite study also concluded that olivine crystallization/orthopyroxene assimilation would drive extensive dissolution of orthopyroxene without requiring any significant temperature change in the melt. The compositions of olivine margins in the Majugaa kimberlite of the Manitsoq region in Greenland indicate that their crystallization was coupled with assimilation of xenocrystic orthopyroxene (Pilbeam *et al.*, 2011). Pilbeam *et al*. (2011) proposed that the compositions of the olivine magmatic margins are best explained by the interaction of an asthenospheric carbonatite melt with lithospheric mantle. Furthermore, high-temperature experiments demonstrate that the increase in SiO_2 provided by the assimilation of orthopyroxene will result in the exsolution of CO_2, providing a driving mechanism for eruption of the dense and crystal-rich kimberlite magmas (Russell et al., 2012). Most recent studies of kimberlite magma consider the xenolithic component to be either a mixture of olivine + orthopyroxene or simply bulk cratonic mantle (Kopylova *et al.*, 2007; Kjarsgaard *et al.*, 2009; Patterson *et al.*, 2009). There is thus consensus on the composition of the xenocrystic component, but there is still debate as to how much of the olivine in a kimberlite is xenocrystic, and therefore what proportion of cratonic mantle should be removed from the bulk kimberlite composition.

Previously, the amount of xenocrystic component removed has been largely based on the estimated modal abundance of xenocrystic olivine content, but these estimates vary between workers from 100% (Brett *et al.*, 2009; Patterson *et al.*, 2009) to 30% (Mitchell, 2008; Kjarsgaard *et al.*, 2009). In this study, we use a different approach; the mantle component is removed until the Fe/Mg ratio of the residual composition is in equilibrium with the forsterite content of the magmatic olivine margins. We used this technique to constrain the magma compositions for the Nikos and Nanuq kimberlites, as well as for four other kimberlite suites using the olivine data from previous studies (Diavik – Brett *et al*., 2009; Udachnaya – Kamenetsky *et al*., 2008; Benfontein and Orapa (AK6) – Arndt *et al*., 2010). The starting bulk-rock compositions for our XMEM calculation are taken from the literature except for the Nanuq kimberlite which is presented in this study for the first time (table 2-2). Studies of sub-continental lithospheric mantle (SCLM) indicates that the SCLM has a relatively restricted harzburgite composition (table 2-3), we used a cratonic mantle composition relevant to each locality in our calculations (Nikos and Nanuq – (Schmidberger & Francis, 1999); South Africa – (Boyd & Mertzman, 1987); Siberia – (Boyd *et al.*, 1997); Slave Province – (Kopylova & Russell, 2000).

Previous studies have employed high olivine-liquid $k_{D(Fe/Mg)}$ (i.e. 0.36 -Kopylova *et al*, 2007; 0.5 -Arndt *et* al., 2010) based on the high $k_{D(Fe/Mg)}$ observed in carbonate rich systems to explain the low forsterite content of kimberlite olivine (Fo_{91-92}), given the high Mg# (0.87) of their estimated magma compositions. A compilation of experimental results (figure 2-4) indicates, however, that for the range of CO_2 contents (10-25 wt%) estimated for kimberlite magmas a $k_{D(Fe/Mg)}$ of ~0.3 is more appropriate.

All six calculated kimberlite magma compositions (table 2-4) are low in SiO_2 (0-15 wt%), high in CO_2 (25-35 wt%; Nanuq is an exception at 9 wt%) and CaO contents (25-34 wt%). They have very low MgO contents (9-18 wt%; table 2-4) in comparison to previously proposed kimberlite magma compositions (15-31 wt%; table 2-1), whereas the FeO contents are similar (7-13 wt% and 6-11 wt% respectively). With the exception of the Nanuq kimberlite, the normative mineralogy of the calculated magma compositions (table 2-4) have high carbonate contents (55-75 %), primarily calcite, but also with varying proportion of magnesian carbonate. The high normative carbonate contents (55-75%) clearly demonstrate the silico-carbonatite nature of kimberlite magmas. The low normative olivine content of these calculated magmas, on the other hand, indicates that kimberlite magmas cannot crystallize significant olivine.

The observed ratio of mantle-derived orthopyroxene to olivine xenocrysts is very low in kimberlite relative to the ratio of orthopyroxene to olivine in cratonic mantle xenoliths (i.e. Nikos -Schmidtberger & Francis, 1999). The low abundance of orthopyroxene in kimberlite has been ascribed to rapid dissolution of orthopyroxene in the kimberlite magmas (Edgar and Charbonneau, 1993; Ulmer and Sweeney, 2002; Le Roex *et al*., 2003). Orthopyroxene assimilation would be accompanied by the concomitant crystallization of olivine and an increased silica content of the kimberlite magma:

$$Mg_2Si_2O_6 \Leftrightarrow Mg_2SiO_4 + SiO_2$$

To test the possibility that orthopyroxene assimilation is responsible for the unusual zoning pattern in the magmatic olivine margins, we have modeled the effects of combined orthopyroxene assimilation and olivine crystallization (figure 2-5). The model forces the fractionation of olivine using the solid solution expressions of Beattie *et* al. (1991), along with trace element K_d values from the Geochemical Earth Reference Model (GERM), and uses an orthopyroxene composition consistent with that of SCLM orthopyroxene ($En_{92}$and Ni 300-800 ppm) as the contaminant. In each kimberlite suite, the starting liquid composition for the models was the kimberlite liquid composition calculated by the XMEM (table 2-4). We adjusted the Ni content of the initial magma such that the Ni content of the first olivine composition matched that of the olivine margins closest to the core/margin boundary. Our model indicates that the Ni content in the outermost olivine margins is sensitive to the Ni content of the assimilated orthopyroxene. We adjusted the Ni content of the assimilated orthopyroxene to match the Ni content observed in the outermost olivine margins. In all cases, the assumed Ni content of assimilated orthopyroxene is within the range of cratonic orthopyroxene (300-800 ppm). We found that the zoning observed across the magmatic olivine margins is best fit by models in which there is an one-to-one molar ratio of orthopyroxene assimilation relative to olivine crystallization, which corresponds to approximately 0.7 by weight.

Although the forsterite content of the olivine margins is quite restricted in individual kimberlite suites (i.e the Nikos = $Fo_{88.5}$), it is evident that there are significant differences between kimberlite suites (Fo_{86-91}). Although the assimilation / crystallization model reproduces the compositional trend of the margins in each kimberlite suite, kimberlite magmas with different Fe/Mg ratios are required to explain the different trends. Although the different compositions appear to be regionally specific, it is unlikely that they reflect differing lithospheric composition, since SCLM has a relatively restricted Mg# of 0.92±0.01 (Boyd & Mertzman, 1987; Boyd *et al.*, 1997; Schmidberger & Francis, 1999; Kopylova & Russell, 2000). However, to explain unusual characteristic of high enrichment of the incompatible trace element contents of kimberlites is commonly attributed to a carbonate-rich asthenospheric component (Kramers *et al.*, 1981; Smith, 1983; Smith *et al.*, 1985; Le Roex, 1986; Bizzarro *et al.*, 2002; Nowell *et al.*, 2004; Patterson *et al.*, 2009). The variation in the forsterite contents of magmatic olivine margins between different kimberlites suggests that the Fe/Mg ratio of the carbonate-rich asthenospheric component may be heterogeneous on a regional scale. The fact that magmatic olivine margins in many South African kimberlites (Moore, 1988) have a distinctive Fo88 composition suggests a regional ‘flavor’ to the carbonate-rich asthenospheric component beneath the Kaapvaal craton. Most importantly, however, is that the magmatic margins on kimberlite olivine indicate that kimberlite liquids are carbonate-rich (55-75 %) and relatively MgO (9-18 wt%) and SiO_2 (0-15 wt%) poor.

Conclusions

The majority of the olivine core compositions from both the Nikos and Nanuq kimberlite suites are un-zoned and virtually identical (Fo_{92}, Ni ~ 3000 ppm and low Ca <0.3 wt%) to that of cratonic mantle olivine, an observation that is consistent with the majority of the olivine in kimberlite being xenocrystic. The compositional variation of Ni at constant forsterite content across olivine margin indicates that magmatic crystallization rather than diffusion is controlling the compositional profiles of the olivine margins. We conclude from the foregoing that although the olivine cores have xenocrystic origins, the olivine margins are in fact magmatic overgrowths.

The estimated proportion of the component removed in the xenocrystic mantle extraction method (XMEM) is much improved if based on removal until the Fe/Mg ratio of the residual composition is in equilibrium with the forsterite content of the magmatic olivine margins. A compilation of experimental results indicates that, for the range of proposed kimberlite CO_2 contents (10-25 wt%), a $k_{D(Fe/Mg)}$ of ~0.3 is the appropriate value to be used in the foregoing method. The normative mineralogy of the calculated magma compositions resulting from XMEM calculations have high carbonate contents (55-75 %), clearly demonstrating the silico-carbonatitic nature of kimberlite magmas. Although the normative olivine content of these calculated kimberlite magmas is significant (16-33%), the liquid represents only 20-50% of the bulk-rock volume, thus magmatic olivine accounts for only 5-15% of the kimberlite modal mineralogy, consistent with previous studies indicating low abundance of magmatic olivine in kimberlite (Brett *et al.*, 2009; Patterson *et al.*, 2009; Arndt *et al.*, 2010).

The zoning observed across the magmatic margins on kimberlite olivine is best fit by models in which there a one-to-one molar ratio of orthopyroxene assimilation relative to olivine crystallization. Although the forsterite content of the olivine margins is quite restricted in individual kimberlite suites (i.e the Nikos = $Fo_{88.5}$), there are significant differences between kimberlite suites (Fo86-91) requiring different Fe/Mg ratios in their kimberlite liquids. It is unlikely that these different Fe/Mg ratios can be ascribed to the assimilation of differing SCLM composition (or differing orthopyroxene compositions), since SCLM has a relatively restricted Mg# of 0.92±0.01. The variation in the forsterite contents of magmatic olivine margins in different kimberlites suggests that the Fe/Mg ratio of the carbonate-rich asthenospheric component may be heterogeneous on a regional scale.

References

Arndt, N. (2003). Komatiites, kimberlites, and boninites. *Journal of Geophysical Research: Solid Earth* **108**, 2293.

Arndt, N. T., Guitreau, M., Boullier, A.-M., Le Roex, A., Tommasi, A., Cordier, P. & Sobolev, A. (2010). Olivine, and the Origin of Kimberlite. *Journal of Petrology* **51**, 573-602.

Bailey, D. K. (1984). Kimberlite: "The mantle sample' formed by ultrametasomatism. In: Kornprobst, J. (ed.) *3rd International Kimberlite Conference*, 323-333.

Beattie, P., Ford, C. & Russell, D. (1991). Partition coefficients for olivine-melt and orthopyroxene-melt systems. *Contributions to Mineralogy and Petrology* **109**, 212-224.

Becker, M. & le Roex, A. P. (2006a). Geochemistry and petrogenesis of South African isotopically transitional kimberlites located on and off the Kaapvaal Craton. *Lithos*.

Becker, M. & Le Roex, A. P. (2006b). Geochemistry of South African on- and off-craton, group I and group II kimberlites: Petrogenesis and source region evolution. *Journal of Petrology* **47**, 673-703.

Bizzarro, M., Simonetti, A., Stevenson, R. K. & David, J. (2002). Hf isotope evidence for a hidden mantle reservoir. *Geology* **30**, 771-774.

Boyd, F. R. & Mertzman, S. A. (1987). Composition and structure of the Kaapvaal lithosphere, southern Africa. *Magmatic Processes: Physicochemical Principles*, 13-24.

Boyd, F. R., Pokhilenko, N. P., Pearson, D. G., Mertzman, S. A., Sobolev, N. V. & Finger, L. W. (1997). Composition of the Siberian cratonic mantle: evidence from Udachnaya peridotite xenoliths. *Contributions to Mineralogy and Petrology* **128**, 228-246.

Brett, R. C., Russell, J. K. & Moss, S. (2009). Origin of olivine in kimberlite: Phenocryst or impostor? *Lithos* **112, Supplement 1**, 201-212.

Canil, D. & Bellis, A. J. (2007). Ferric Iron in CaTiO3 Perovskite as an Oxygen Barometer for Kimberlite Magmas II: Applications. *Journal of Petrology* **48**, 231-252.

Canil, D. & Bellis, A. J. (2008). Phase equilibria in a volatile-free kimberlite at 0.1 MPa and the search for primary kimberlite magma. *Lithos* **105**, 111-117.

Dalton, J. A. & Presnall, D. G. (1998). The continuum of primary carbonatitic-kimberlitic melt compositions in equilibrium with lherzolite: Data from the system CaO-MgO-Al_2O_3-SiO_2-CO_2 at 6 GPa. *Journal of Petrology* **39**, 1953-1964.

Dawson, J. B. & Hawthorne, J. B. (1973). Magmatic sedimentation and carbonatitic differentiation in kimberlite sills at Benfontein, South Africa. *Journal of the Geological Society* **129**, 61-85.

Edgar, A. D. & Charbonneau, H. E. (1993). Melting experiments on a SiO_2 -poor, CaO-rich aphanitic kimberlite from 5-10 GPa and their bearing on sources of kimberlite magmas. *American Mineralogist* **78**, 132-142.

Eggler, D. H. (1973). Role of CO_2 in melting processes in the mantle. *Carnegie Inst Wash Year Book* **72**, 457-467.

Fedortchouk, Y. & Canil, D. (2004). Intensive Variables in Kimberlite Magmas, Lac de Gras, Canada and Implications for Diamond Survival. *Journal of Petrology* **45**, 1725-1745.

Francis, D. (1985). The Baffin Bay lavas and the value of picrites as analogues of primary magmas. *Contributions to Mineralogy and Petrology* **89**, 144-154.

Francis, D. & Patterson, M. (2009). Kimberlites and aillikites as probes of the continental lithospheric mantle. *Lithos* **109**, 72-80.

Frisch, T. & Hunt, P. A. (1993). *Reconnaissance U–Pb geochronology of the crystalline core of the Boothia Uplift, District of Franklin, Northwest Territories*: Geological Survey of Canada.

Girnis, A. V. (2005). Transition from kimberlite to carbonatite melt under mantle parameters: An experimental study. *Petrology* **13**, 1-15.

Gurney, J. J., Jacob, W. R. O. & Dawson, J. B. (1979). *Megacrysts from the Monastery kimberlite pipe, South Africa.*: American Geophysical Union.

Harris, M., le Roex, A. & Class, C. (2004). Geochemistry of the Uintjiesberg kimberlite, South Africa: Petrogenesis of an off-craton, group I, kimberlite. *Lithos* **74**, 149-165.

Heaman, L. M. (1989). The nature of the subcontinental mantle from Sr-Nd-Pb isotopic studies on kimberlitic perovskite. *Earth and Planetary Science Letters* **92**, 323-334.

Heaman, L. M., Kjarsgaard, B. A. & Creaser, R. A. (2003). The timing of kimberlite magmatism in North America: implications for global kimberlite genesis and diamond exploration. *Lithos* **71**, 153-184.

Kamenetsky, V. S., Kamenetsky, M. B., Sharygin, V. V., Faure, K. & Golovin, A. V. (2007). Chloride and carbonate immiscible liquids at the closure of the kimberlite magma evolution (Udachnaya-East kimberlite, Siberia). *Chemical Geology* **237**, 384-400.

Kennedy, C. S. & Kennedy, G. C. (1976). The Equilibrium Boundary Between Graphite and Diamond. *J. Geophys. Res.* **81**, 2467-2470.

Kjarsgaard, B. A., Pearson, D. G., Tappe, S., Nowell, G. M. & Dowall, D. P. (2009). Geochemistry of hypabyssal kimberlites from Lac de Gras, Canada: Comparisons to a global database and applications to the parent magma problem. *Lithos* **112**, 236-248.

Kopylova, M. G., Matveev, S. & Raudsepp, M. (2007). Searching for parental kimberlite melt. *Geochimica et Cosmochimica Acta* **71**, 3616-3629.

Kopylova, M. G. & Russell, J. K. (2000). Chemical stratification of cratonic lithosphere: Constraints from the Northern Slave craton, Canada. *Earth and Planetary Science Letters* **181**, 71-87.

Kramers, J., Smith, C., Lock, N., Harmon, R. & Boyd, F. (1981). Can Kimberlites be generated from an ordinary mantle?

Le Roex, A. P. (1986). Geochemical correlation between Southern African kimberlites and South Atlantic hotspots. *Nature* **324**, 243-245.

le Roex, A. P., Bell, D. R. & Davis, P. (2003). Petrogenesis of Group I Kimberlites from Kimberley, South Africa: Evidence from Bulk-rock Geochemistry. *Journal of Petrology* **44**, 2261-2286.

Luth, R. (2009). The activity of silica in kimberlites, revisited. *Contributions to Mineralogy and Petrology* **158**, 283-294.

Mitchell, R. H. (1986). *Kimberlites : mineralogy, geochemistry, and petrology*. New York: Plenum.

Mitchell, R. H. (1995). *Kimberlites, Orangeites, and Related Rocks*.

Mitchell, R. H. (2008). Petrology of hypabyssal kimberlites: Relevance to primary magma compositions. *Journal of Volcanology and Geothermal Research* **174**, 1-8.

Mitchell, R. H. & Meyer, H. O. A. (1980). Mineralogy of micaceous kimberlite from the Jos Dyke, Somerset Island, N.W.T. *The Canadian Mineralogist* **18**, 241-250.

Moore, A. E. (1988). Olivine: a monitor of magma evolutionary paths in kimberlites and olivine melilitites. *Contributions to Mineralogy and Petrology* **99**, 238-248.

Nielsen, T. F. D. & Sand, K. K. (2008). The Majuagaa kimberlite dike, Maniitsoq region, West Greenland: Constraints on an Mg-rich silicocarbonatitic melt composition from groundmass mineralogy and bulk compositions. *Canadian Mineralogist* **46**, 1043-1061.

Nowell, G., Pearson, D., Bell, D., Carlson, R., Smith, C., Kempton, P. & Noble, S. (2004). Hf isotope systematics of kimberlites and their megacrysts: new constraints on their source regions. *Journal of Petrology* **45**, 1583-1612.

Okulitch, A. V. & Trettin, H. P. (1991). *Late Cretaceous — Early Tertiary deformation, Artic Islands*: Geological Survey of Canada.

Ootto, J. W. & Wyllie, P. J. (1993). Relationships between silicate melts and carbonate-precipitating melts in CaO-MgO-SiO2-CO2-H2O at 2 kbar. *Mineralogy and Petrology* **48**, 343-365.

Parman, S. W., Dann, J. C., Grove, T. L. & de Wit, M. J. (1997). Emplacement conditions of komatiite magmas from the 3.49 Ga Komati Formation, Barberton Greenstone Belt, South Africa. *Earth and Planetary Science Letters* **150**, 303-323.

Patterson, M. & Francis, D. (2009). Kimberlite degassing and paleoclimate. *American Geophysical Union, Fall Meeting*. San Francisco.

Patterson, M., Francis, D. & McCandless, T. (2009). Kimberlites: Magmas or mixtures? *Lithos* **112**, 191-200.

Pell, J. A. (1993). *New kimberlite discoveries on Somerset Island. Exploration Overview 1993*.

Pell, J. A., Holmes, P. K., Grenon, H., Sell, M. V. & Tam, L. (2009). Exploration and discovery of a new kimberlite cluster on the Nanuq Property, Western Churchill Province, Kivalliq area, Nunavut. *9th International Kimberlite Conference, Franfurt, Germany* **Long Abstracts**.

Petry, C., Chakraborty, S. & Palme, H. (2004). Experimental determination of Ni diffusion coefficients in olivine and their dependence on temperature, composition, oxygen fugacity, and crystallographic orientation. *Geochimica et Cosmochimica Acta* **68**, 4179-4188.

Pilbeam, L. H., Nielsen, T. F. D. & Waight, T. E. (2011). Melt compositions and processes in the kimberlite provience of southern West Greenland. *Goldschmidt*. Prague: Mineralogical Magazine, 1643.

Price, S. E., Russell, J. K. & Kopylova, M. G. (2000). Primitive magma from the Jericho Pipe, NWT, Canada: constraints on primary kimberlite melt chemistry. *Journal of Petrology* **41**, 789-808.

Qian, Q., O'Neill, H. S. C. & Hermann, J. (2010). Comparative diffusion coefficients of major and trace elements in olivine at ~950 °C from a xenocryst included in dioritic magma. *Geology* **38**, 331-334.

Ringwood, A. E., Kesson, S. E., Hibberson, W. & Ware, N. (1992). Origin of kimberlites and related magmas. *Earth and Planetary Science Letters* **113**, 521-538.

Russell, J. K., Porritt, L. A., Lavallee, Y. & Dingwell, D. B. (2012). Kimberlite ascent by assimilation-fuelled buoyancy. *Nature* **481**, 352-356.

Schmidberger, S. S. & Francis, D. (1999). Nature of the mantle roots beneath the North American craton: mantle xenolith evidence from Somerset Island kimberlites. *Lithos* **48**, 195-216.

Skinner, E. M. W. & Clement, C. R. (1979). Mineralogical classification of South African kimberlites. In: Boyd, F. R. & Meyer, H. A. (eds.) *3rd International Kimberlite Conference*. Washington: AGU, 129-139.

Smith, C. B. (1983). Pb, Sr and Nd isotopic evidence for sources of southern African Cretaceous kimberlites.

Smith, C. B., Allsopp, H. L., Garvie, O. G., Kramers, J. D., Jackson, P. F. S. & Clement, C. R. (1989). Note on the U-Pb perovskite method for dating kimberlites: Examples from the Wesselton and De Beers mines, South Africa, and Somerset Island, Canada. *Chemical Geology: Isotope Geoscience section* **79**, 137-145.

Smith, C. B., Gurney, J. J., Skinner, E. M. W., Clement, C. R. & Ebrahim, N. (1985). Geochemical character of southern African kimberlites: a new approach based on isotopic constraints. *Transactions of the Geological Society of South Africa* **88**, 267-280.

Sparks, R. S. J., Brooker, R. A., Field, M., Kavanagh, J., Schumacher, J. C., Walter, M. J. & White, J. (2009). The nature of erupting kimberlite melts. *Lithos* **112, Supplement 1**, 429-438.

Steward, W. D. (1987). Late Proterozoic to Early Tertiary stratigraphy of Somerset Island and northern Boothia Peninsula, District of Franklin. *Geological Survey of Canada Papers* **83**.

Trettin, H. P., Frisch, T. O., Sobczak, L. W., Weber, J. R., Niblett, E. R., Law, L. K., DeLaaurier, I. & Witham, K. (1972). *The Innuitian Province*: Geological Association of Canada.

Ulmer, P. & Sweeney, R. J. (2002). Generation and differentiation of group II kimberlites: constraints from a high-pressure experimental study to 10 GPa. *Geochimica et Cosmochimica Acta* **66**, 2139-2153.

Wyllie, P. J. & Tuttle, O. F. (1960). The System CaO–CO_2–H_2O and the Origin of Carbonatites. *Journal of Petrology* **1**, 1-46.

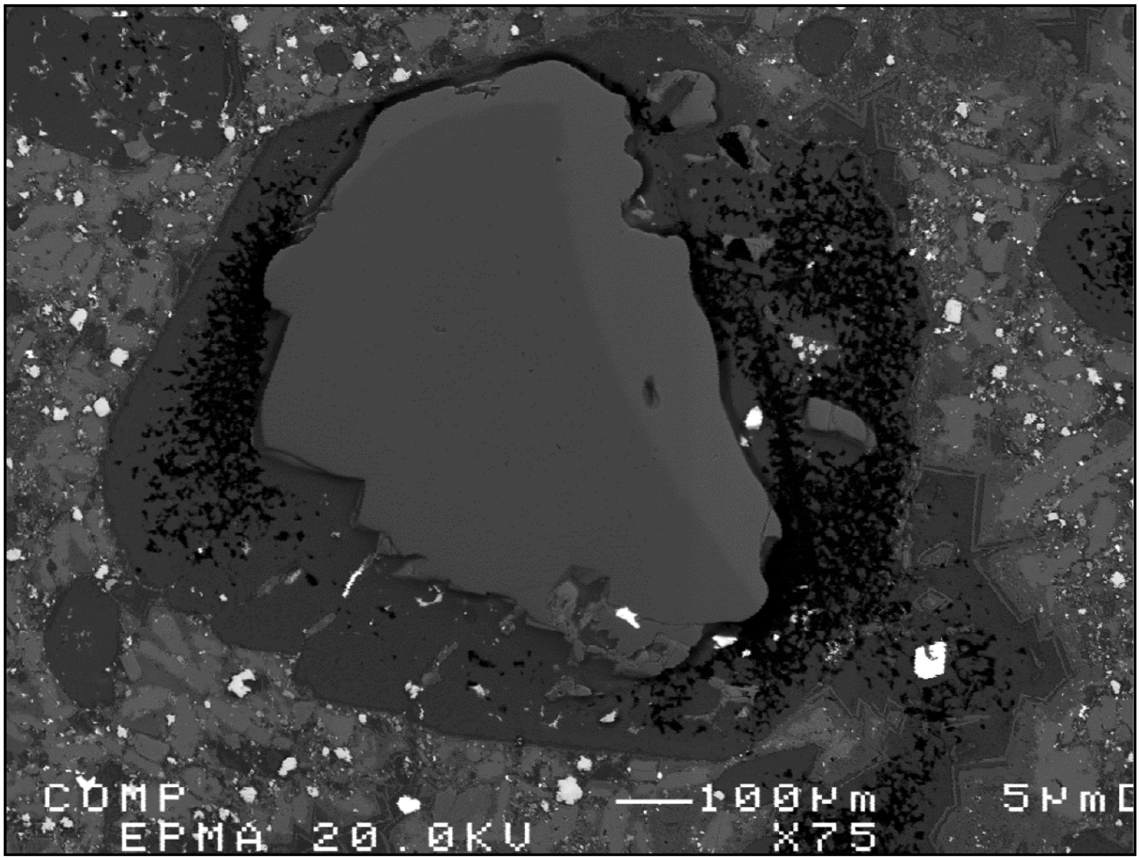

Figure 2-1: Backscatter image of zoned olivine from the Nikos kimberlite illustrating overall euhedral shape of the composite crystal (core + margin + serpentine alteration) and exhibiting the sharp boundary between the inner high forsterite core and lower forsterite margin.

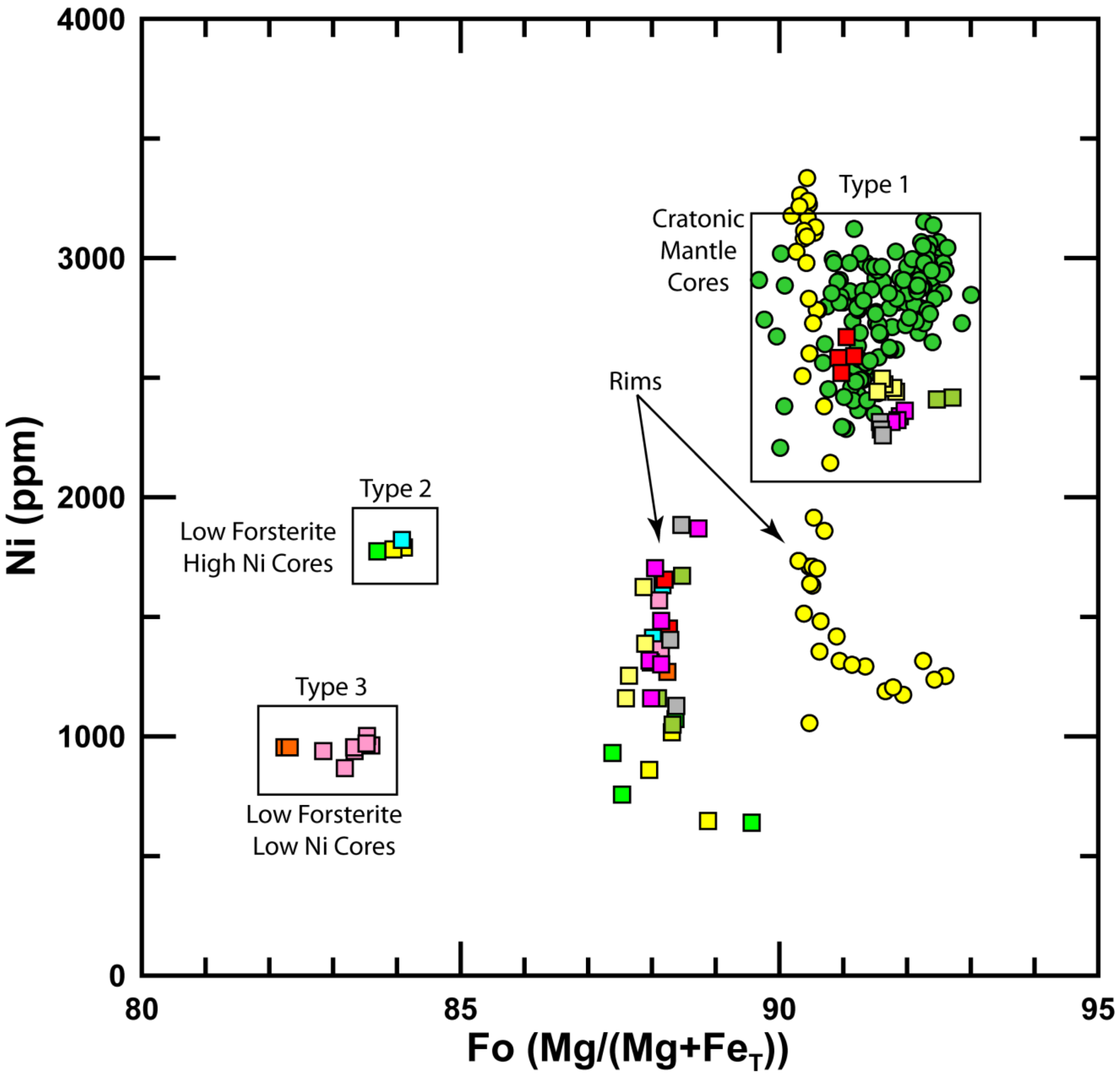

Figure 2-2: Ni versus forsterite diagram for high precision electron microprobe data. Types of core compositions and margin compositions indicated on diagram. Common grayscale indicates core/rim pairs (squares – Nikos kimberlite; circles – Nanuq kimberlite).

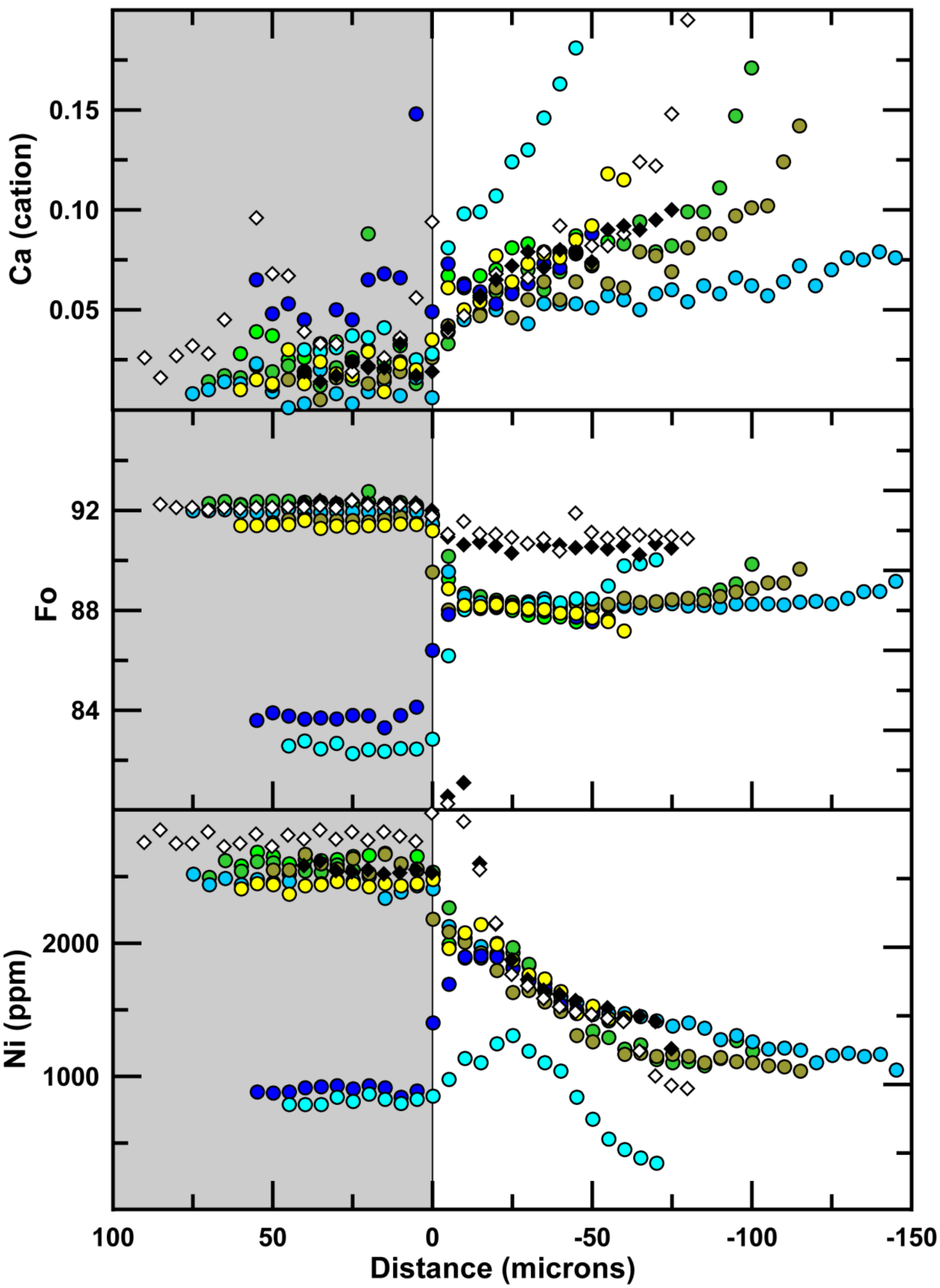

Figure 2-3: Profiles of calcium, forsterite and nickel contents versus distance (from core/margin boundary) for electron microprobe transect analysis of zoned olivine. Grey area indicates olivine core portion of transect and white area indicates olivine margin area. Circles are from the Nikos kimberlite and white/black diamonds are transects from the Nanuq kimberlite.

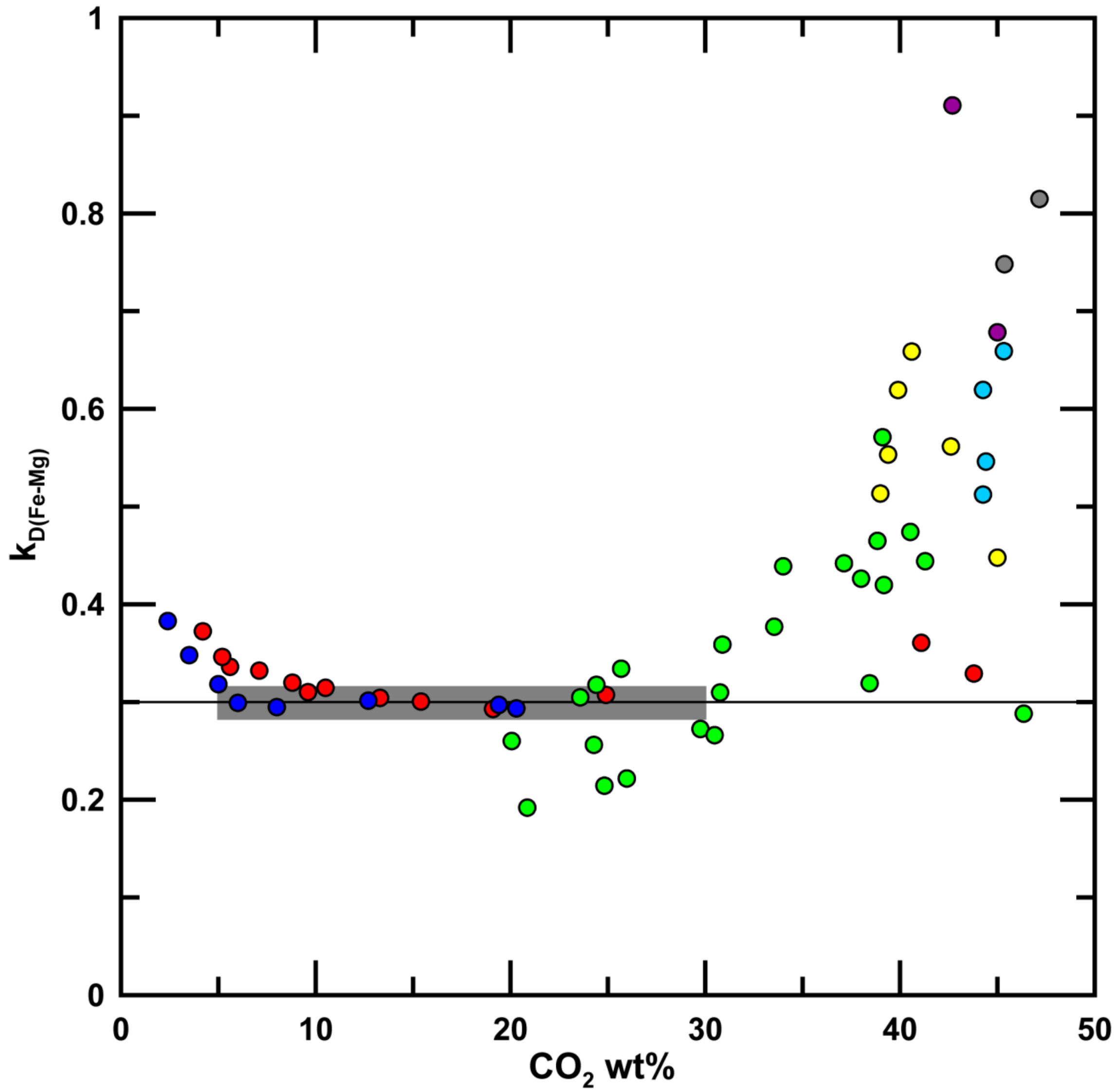

Figure 2-4: Fe/Mg partitioning coefficients ($k_{D(Fe/Mg)}$)) versus CO_2 wt% diagram plotting experimental melt data for kimberlite. (White and black grey circles – Dasgupta and Hirschmann (2007); grey circles – Brey et al. (2008); squares – Dasgupta et al. (2007); grey hexagons – Dalton and Wood (1993); white hexagons – Ghosh et al. (2009).

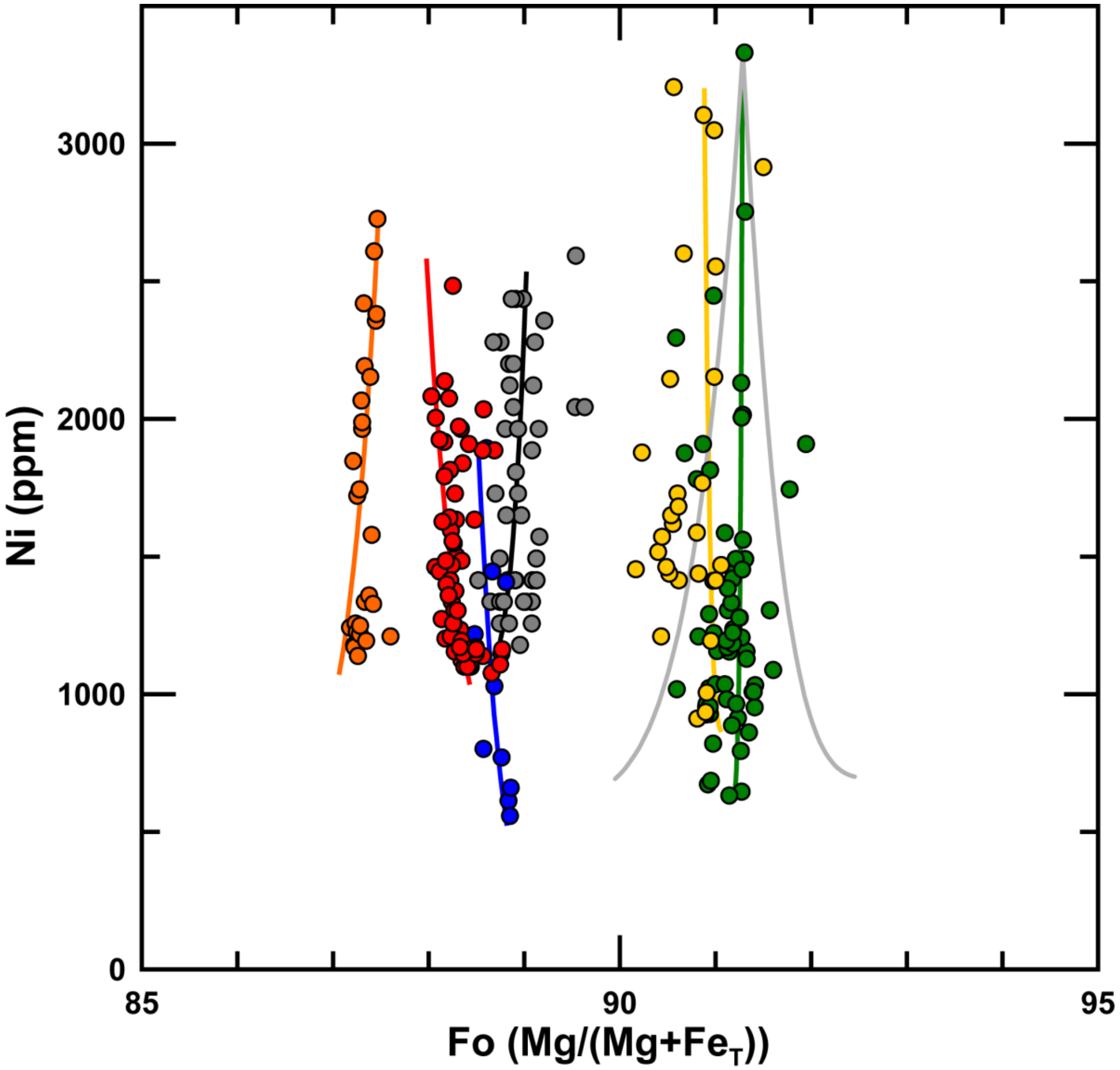

Figure 2-5: Ni versus forsterite diagram. Background symbols are measured and/or reported olivine overgrowth compositions (orange – Benfontien; red – Nikos; blue – Orapa; grey – Udachnaya; yellow – Nanuq; green – Diavik). Dark corresponding lines indicate the one-to-one molar assimilation/crystallization (OPX/OL) model trend and the light grey lines indicate 0.75 and 1.25 molar ratio for the Diavik data.

	Literature estimates of kimberlite magma						
	South Africa			**Slave**		**Superior**	**Greenland**
	AVG Group I	**Kimberley**	**Uintjiesberg**	**Jericho**	**Lac de Gras**	**Foxtrot**	**W. Greenland**
	BLR[1]	**Le ROEX**[2]	**HARRIS**[3]	**JD69**[4]	**Low TiO_2**[5]	**Renard**[6]	**Majaugaa**[7]
SiO_2	*29.38*	*30.57*	*27.31*	*29.77*	*34.82*	*24.33*	*17.66*
TiO_2	*2.90*	*2.54*	*3.53*	*0.55*	*0.79*	*2.91*	*5.04*
Al_2O_3	*3.10*	*2.54*	*2.53*	*1.43*	*3.37*	*5.92*	*2.29*
MgO	*28.34*	*30.56*	*28.50*	*24.69*	*33.71*	*15.15*	*24.24*
FeO	*10.85*	*10.15*	*10.01*	*5.94*	*9.07*	*8.90*	*10.72*
MnO	*0.21*	-	*0.21*	*0.15*	*0.21*	*0.22*	*0.24*
CaO	*14.90*	*13.84*	*16.38*	*21.40*	*10.11*	*22.23*	*17.46*
Na_2O	*0.18*	-	*0.07*	*0.17*	*0.11*	*0.10*	*0.13*
K_2O	*0.93*	*1.73*	*2.04*	*0.44*	*1.13*	*1.96*	*0.32*
P_2O_5	-	-	-	-	*1.06*	*1.03*	*0.82*
CO_2	*9.21*	*8.07*	*9.43*	*15.46*	*5.62*	*17.25*	*21.07*
	100	**100**	**100**	**100**	**100**	**100**	**100**
Mg#	***0.82***	***0.84***	***0.84***	***0.88***	***0.87***	***0.75***	***0.80***

[1] Becker and Le Roex, 2006
[2] Le Roex et al., 2003
[3] Harris et al., 2004
[4] Price et al., 2000
[5] Karsgaard et al., 2009
[6] Patterson et al., 2009
[7] Neilsen & Sand, 2008

Table 2-1: Previously proposed compositions of kimberlite parental magma

	Kimberlite bulk rock					
	Nikos	**Nanuq**	**Diavik**[1]	**Udachnaya**[2]	**Benfontein**[3]	**Orapa**[3]
SiO_2	*19.85*	*30.72*	*29.63*	*27.06*	*26.91*	*27.73*
TiO_2	*2.06*	*1.10*	*1.10*	*1.23*	*1.48*	*0.69*
Al_2O_3	*2.20*	*1.82*	*1.53*	*2.13*	*2.44*	*0.70*
FeO	*7.06*	*7.37*	*7.61*	*6.87*	*9.53*	*7.92*
MgO	*19.97*	*33.68*	*34.49*	*29.42*	*31.86*	*26.37*
MnO	*0.14*	*0.15*	*0.16*	*0.15*	*0.18*	*0.16*
CaO	*21.58*	*8.93*	*9.90*	*12.70*	*12.76*	*11.19*
Na_2O	*0.19*	*0.18*	*0.05*	*0.69*	*0.11*	*0.31*
K_2O	*1.00*	*0.27*	*0.36*	*1.06*	*0.10*	*0.26*
P_2O_5	*0.64*	*3.78*	*0.44*	*0.49*	*1.24*	*1.07*
CO_2	*22.78*	*1.99*	*8.83*	*9.83*	*10.91*	*12.10*
Total	*97.47*	*89.99*	*94.10*	*91.63*	*97.52*	*88.50*
Ni	661	1466	n/a	n/a	n/a	n/a

[1] Brett et al., 2009
[2] Kamenetsky et al., 2007
[3] Hawthorne, 1968

Table 2-2: Bulk rock compositions of kimberlite investigated.

	Mantle xenolith bulk rock					
	Nikos[1]	**Nanuq[1]**	**Diavik[2]**	**Udachnaya[3]**	**Benfontein[4]**	**Orapa[4]**
SiO_2	*41.83*	*41.83*	*43.49*	*39.95*	*45.51*	*45.51*
TiO_2	*0.05*	*0.05*	*0.04*	*0.04*	*0.08*	*0.08*
Al_2O_3	*1.80*	*1.80*	*0.92*	*1.04*	*1.29*	*1.29*
FeO	*7.31*	*7.31*	*6.74*	*6.49*	*6.39*	*6.39*
MgO	*42.68*	*42.68*	*43.97*	*40.82*	*43.37*	*43.37*
MnO	*0.12*	*0.12*	*0.11*	*0.12*	*0.11*	*0.11*
CaO	*1.27*	*1.27*	*0.75*	*0.85*	*0.92*	*0.92*
Na_2O	*0.08*	*0.08*	*0.16*	*0.06*	*0.07*	*0.07*
K_2O	*0.07*	*0.07*	*0.14*	*0.12*	*0.14*	*0.14*
P_2O_5	*0.02*	*0.02*	*0.03*	*0.01*	*0.01*	*0.01*
CO_2	*0.00*	*0.00*	*0.00*	*0.00*	*0.00*	*0.00*
Total	*95.23*	*95.23*	*96.36*	*89.50*	*97.91*	*97.91*

[1] Schmidtbeger and Francis, 1999

[2] Kopylova and Russell, 2000; Kopylova and Caro, 2004

[3] Boyd et al., 1997

[4] Boyd, 1987

Table 2-3: Bulk rock compositions of cratonic mantle used in xenocrystic mantle extraction method.

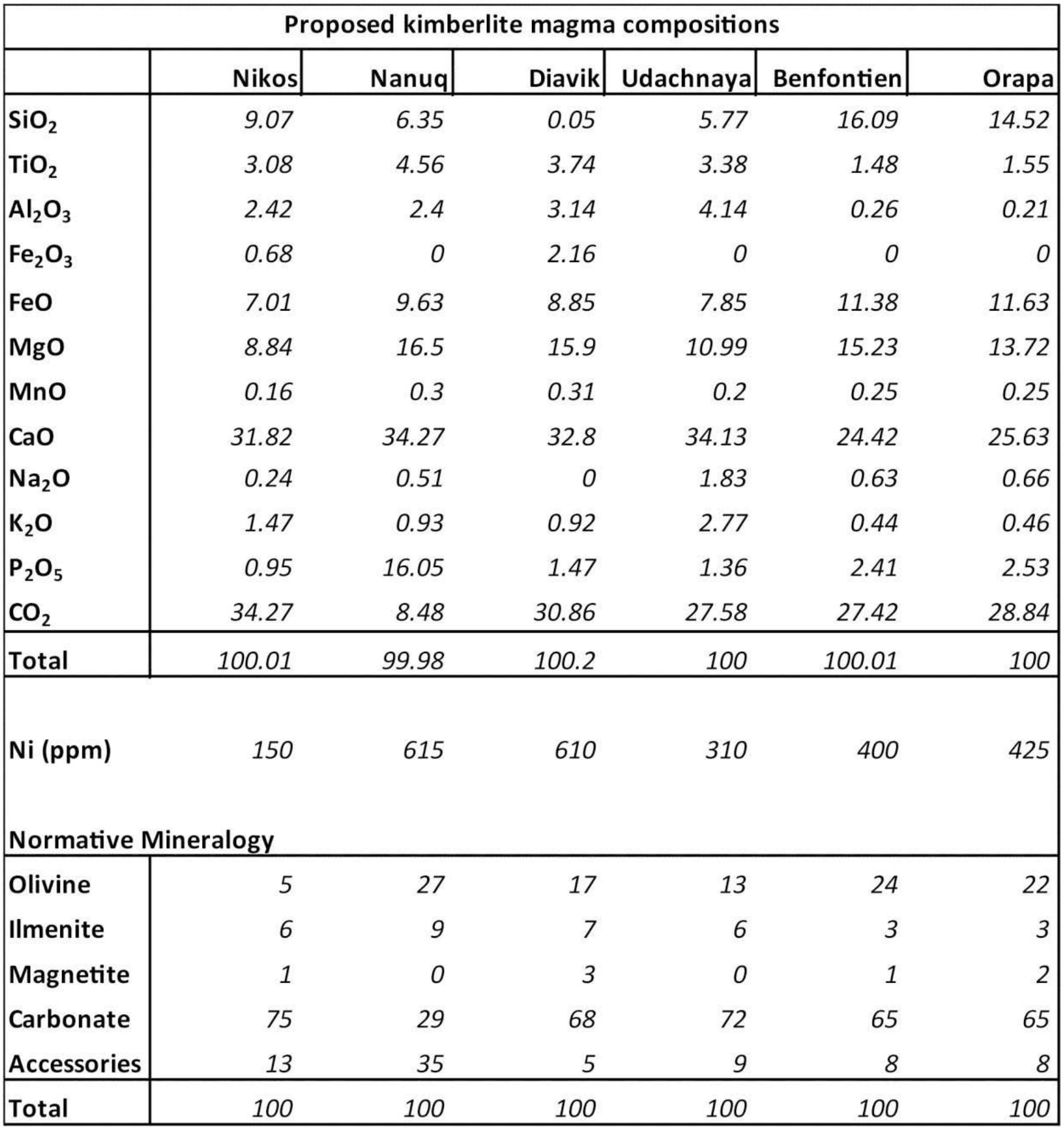

Proposed kimberlite magma compositions

	Nikos	Nanuq	Diavik	Udachnaya	Benfontien	Orapa
SiO_2	9.07	6.35	0.05	5.77	16.09	14.52
TiO_2	3.08	4.56	3.74	3.38	1.48	1.55
Al_2O_3	2.42	2.4	3.14	4.14	0.26	0.21
Fe_2O_3	0.68	0	2.16	0	0	0
FeO	7.01	9.63	8.85	7.85	11.38	11.63
MgO	8.84	16.5	15.9	10.99	15.23	13.72
MnO	0.16	0.3	0.31	0.2	0.25	0.25
CaO	31.82	34.27	32.8	34.13	24.42	25.63
Na_2O	0.24	0.51	0	1.83	0.63	0.66
K_2O	1.47	0.93	0.92	2.77	0.44	0.46
P_2O_5	0.95	16.05	1.47	1.36	2.41	2.53
CO_2	34.27	8.48	30.86	27.58	27.42	28.84
Total	100.01	99.98	100.2	100	100.01	100
Ni (ppm)	150	615	610	310	400	425
Normative Mineralogy						
Olivine	5	27	17	13	24	22
Ilmenite	6	9	7	6	3	3
Magnetite	1	0	3	0	1	2
Carbonate	75	29	68	72	65	65
Accessories	13	35	5	9	8	8
Total	100	100	100	100	100	100

Table 2-4: Proposed parental magma compositions of kimberlites investigated.

CHAPTER 3

Constraining the compositions of kimberlite magma using pelletal lapilli

Chapter 2 investigated the composition of kimberlite magma utilizing a tenet of igneous petrology, equilibrium crystallization; and in this case olivine crystallization from kimberlite magma. Equilibrium crystallization requires that the composition of the mineral is related, by partition coefficients, to the composition of the liquid or melt from which it is crystalizing. Therefore the composition of kimberlite magma can be calculated using the composition of magmatic olivine in kimberlite. Chapter 3 approaches the same question, what is the composition of kimberlite magma, utilizing a different component of kimberlite: pelletal lapilli. Lapilli are common in volcanic rocks and are understood to form through the successive coating of a fragment by the magma, thus representing direct samples of that magma.

Abstract

Pelletal lapilli have long been recognized as droplets of magma formed during the eruption of a variety of volcanic suites, including kimberlites. The compositions of kimberlite pelletal lapilli have, however, received little attention due to the difficulty of analyzing such small volumes of rock. The major element compositions of pelletal lapilli from three kimberlite occurrences obtained using both broad beam electron microprobe analysis and bulk X-ray fluorescence analysis indicate that the results of both techniques are indistinguishable. Thus data gathered from small pelletal lapilli with an electron microprobe not only accurately reflects the composition of pelletal lapilli, but can be used to reconstruct the composition of the kimberlite liquid. Kimberlite whole-rock data and pelletal lapilli data both exhibit well-developed, but distinct, compositional arrays in binary plots (Mg versus Si, Ca, C) that intersect at a common Mg content. The kimberlite whole-rock compositional array is assumed to reflect the variation due to entrainment of variable amounts of xenocrystic mantle. The pelletal lapilli compositional array differs systematically from those of their host kimberlite whole-rocks and appears to reflect the variable modal abundance of carbonate and serpentine. The composition at the intersection of the lapilli and the whole-rock arrays is similar to the carbonate- rich and silica-poor kimberlite magma compositions obtained via the mantle xenocryst extraction method, confirming that the compositions of kimberlite pelletal lapilli can be utilized to constrain the composition of kimberlite magma.

Introduction

The composition of kimberlite magma has been debated for many years, with little consensus. Xenocrystic material (principally disaggregated harzburgite) is a fundamental component of kimberlite and must be excluded in order to estimate the composition of the kimberlite liquid. However, the accurate determination of the amount of xenocrystic component in kimberlite is difficult, if not impossible, due to the millimeter scale of xenocrysts and xenoliths. Compounding this difficulty is the hybrid, contaminated, and altered nature of most kimberlite rocks. Therefore, we are left with a dearth of samples that can be confidently considered to be representative of kimberlite liquids, and their composition remains difficult to constrain.

In an effort to approach this problem from a fresh perspective, we utilize the compositions of the fine-grain pelletal lapilli that are a common feature of kimberlite. Pelletal lapilli in kimberlite are ovoid shaped inclusions that have an outer mantle of fine-grained material, and commonly a nucleus consisting of a single mantle xenocryst or, rarely, a crustal lithic fragment (Mitchell, 1986; Mitchell, 1997). Pelletal lapilli have been interpreted to be a juvenile component of ultrabasic, ultramafic and/or carbonatitic diatremes that form during fragmentation at the interface between the erupting magma and a volatile phase (Lloyd and Stoppa, 2003). Pelletal lapilli have been considered as proxies of juvenile magma in a number of different volcanic suites (Lloyd and Stoppa, 2003; Stoppa *et al.*, 2011), and thus pelletal lapilli may provide constraints on the juvenile composition of kimberlite magma. However, in addition to the usual difficulties regarding kimberlite compositional studies (alteration and contamination), obtaining the composition of pelletal lapilli from kimberlite is hampered by the small size (typically <20 mm) of most pelletal lapilli in kimberlite rocks. To address this difficulty, we have developed new techniques to not only analyze kimberlite pelletal lapilli of sufficient size by traditional analysis (X-ray fluorescence and thermocombustion), but also analyze the composition of smaller pelletal lapilli using an electron microprobe (EMP) broad beam technique. The compositions obtained from the smaller pelletal lapilli using the EMP are similar with those obtained by traditional analytical methods on larger samples (figures 3-1 – 3-3).

In this paper we use the composition of pelletal lapilli in kimberlite to demonstrate that they exhibit a compositional array that is distinct from that of the compositional array exhibited by their host kimberlite whole-rock data. The compositional variation of kimberlite whole-rock data is thought to be the result of mixing of primary kimberlite magma with varying amounts of cratonic mantle. However, much of the cratonic mantle olivine is present as xenocrysts, but the orthopyroxene is occult and has presumably been assimilated (Francis and Patterson, 2009). The compositional arrays exhibited by the pelletal lapilli compositions are interpreted to represent varying amounts of orthopyroxene assimilation, thus also exhibit an evolving compositional array. We further show that the two distinct arrays intersect at a common Mg content in binary plots (Mg versus Si, Ca and C) and that the composition of this intersection point is similar to the carbonate rich and silica poor magma compositions obtained via the xenocrystic mantle extraction method. Thus, the compositions of kimberlite pelletal lapilli can be utilized to constrain the composition of kimberlite magma.

Materials and Methods

The pelletal lapilli in this study are taken from three kimberlite localities; the Buffalo Head Hills (BHH) kimberlite cluster in Northern Alberta, the Foxtrot kimberlite field (FKF) in Northern Québec, and the Nikos kimberlite from Somerset Island in Northern Canada. The compositions of pelletal lapilli mantles were analyzed for major elements by both electron microprobe (EMP) and x-ray fluorescence (XRF) techniques. EMP analysis was conducted on a 500 µm area using a 20 kV and $2x10^{-8}$ nA defocused broad beam. At least five areas were analyzed per lapillus and then averaged to construct a composition for the entire lapillus mantle. Wavelength-dispersive spectroscopy (WDS) analyses of major elements have totals between 75 and 85 wt %, with the deficit assumed to be CO_2 and H_2O, present in carbonates and hydrous minerals. Analyses of serpentine from within the pelletal lapilli mantles were used to estimate the water content by allocating the mass balance deficit of the serpentine as H_2O. Both petrographic observation and image analysis were used to estimate the modal abundance of serpentine in the pelletal lapilli mantles, which were then used to estimate the bulk H_2O content of the pelletal lapilli. Any remaining mass deficit was assumed to be CO_2.

The advantage of the EMP technique is the ability to analyze very thin pelletal lapilli mantles. The disadvantage of the EMP technique is that CO_2 contents must be estimated by means of image analysis and subsequent calculation. Combined, XRF and thermo-combustion analysis do provide robust major element and CO_2 results, but is restricted to larger, less common pelletal lapilli. Pelletal lapilli (n=7) with sufficient mass (>3 g) for XRF and thermo-combustion analyses were ground out of their host using a micro drill. The samples were cut to maximize the pelletal mantle area in polished thin section for EMP analysis, and then the remaining pelletal lapilli mantle was removed from both the section blank and hand sample, ensuring the olivine nucleus was completely removed. The extracted samples were dried at 60 °C, pulverized to 150 µm using an alumina ring-and-puck grinder, and analyzed by X-ray fluorescence using fused bead (major elements) and thermo-combustion for CO_2 at McGill University.

Results

Pelletal lapilli petrography

The pelletal lapilli in this study are removed from the fine-grained serpentine/carbonate matrix of macrocrystic brecciated kimberlite and vary in size from 1 to 10's of mm. The pelletal lapilli tend to have ovoid shapes that do not reflect the shape of the nuclei, which are often angular. The width of mantles of pelletal lapilli can vary from <0.25 mm to 10 mm with little correlation with the overall size of the pelletal lapilli. The mantles of pelletal lapilli are composed of fine-grain serpentine (<200 µm) and finer-grain carbonate (<10 µm), with rare olivine, chlorite, perovskite, ilmenite, magnetite and apatite (<10 µm) crystals. Carbonate composes 30-45% of the pelletal lapilli mantle, whereas serpentine composes 65-50%, and accessory oxides ~ 5% (illmenite, magnetite, perovskite, rutile, apatite). Serpentine in the mantles of pelletal lapilli occur as subhedral to euhedral prismatic grains. The carbonate is primarily calcite, however, the pelletal lapilli in the Renard kimberlite have a notable dolomite abundance (<10%), which occurs in the matrix both as irregular aggregates composed of subhedral to euhedral crystals, and as single, anhedral crystals.

Electron Microprobe Analysis

EMP analysis was conducted on five to twenty spots in each lapillus depending on the size of the pelletal lapilli and the width of their mantles. These analyses have low totals (64-85%), which is attributed to CO_2 in carbonates and H_20 in serpentine (table 3-1). The spot analyses in any given lapillus exhibit a large compositional variation, with CaO contents ranging from 7 to 40 wt%, SiO_2 contents 10 to 29 wt%, and MgO contents 11 to 28 wt% (i.e. sample Renard 067A-A1 to A10). Despite this wide variation for individual elements, the data exhibit good correlations between major elements (Ca, Mg, Si and C), with CaO and CO_2 being negatively correlated with SiO_2. In contrast, MgO exhibits a positive correlation with SiO_2 (figures 3-1 – 3-3). The compositional variations exhibited by the major elements of the pelletal lapilli within an individual kimberlite suite all lay on a common compositional array. Minor elements (Al, Fe, Ti, Na, K and Mn), however, exhibit more scatter when plotted against SiO_2. The compositions of pelletal lapilli mantles in the Nikos and Renard kimberlites lay on similar compositional arrays, however, those of the BHH kimberlite lay on an array with distinctly higher SiO_2 contents (2-3 wt%), at similar MgO, CaO and CO_2 contents. Despite these differences, all three pelletal lapilli compositional arrays from the three kimberlite suites exhibit parallel trends. Serpentine in the lapilli mantles has a maximum grain size of approximately 200 µm and the analyzed spot size is 500 µm, therefore the large compositional range within the spot analyses of individual pelletal lapilli likely reflects the differing proportions of serpentine and carbonate within each analysis (figure 3-4).

Analysis of carbon by EMP is not possible, therefore CO_2 contents were estimated by exploiting the fact that both calcium and carbon are primarily present as calcite. The cation ratio of Ca and C in calcite is one-to-one, therefore for every mole of calcium in the analysis there should be a corresponding mole of carbon, thus the carbon content of each analysis can be calculated. Image analysis estimations of the proportion of carbonate versus non-carbonate minerals (mainly serpentine pseudomorphs) in backscattered electron images provides an independent check of CO_2 contents (figure 3-4). The combination of the estimated CO_2 and amount of H_20 contained in the serpentine closely matches the mass deficit in the EMP analysis of pelletal lapilli (figure 3-4).

X-ray Fluorescence Analysis (plus thermo-combustion)

Seven pelletal lapilli (4-BHH, 2-Nikos and 1-Renard) were large enough to extract for XRF analysis for major elements and thermo-combustion (TC) for CO_2 (table 3-2). The compositions obtained with this technique plot along the compositional trends obtained by EMP analysis (figures 3-1B – 3-3B). In addition, there is a good correspondence between the average composition of the EMP analyses and the XRF analysis for the same lapilli (table 3-2 and figure 3-5). However, the CO_2 contents estimated from the EMP analyses were typically 1-2 wt% higher than those obtained by thermo-combustion. The agreement between the results from both methods indicates that EMP analyses of smaller pelletal lapilli can be used to obtain an estimate of the bulk pelletal lapilli composition.

Comparison of pelletal lapilli and kimberlite whole-rock compositions

The composition of pelletal lapilli obtained in this study are lower in MgO contents than those of the published whole-rock compositions of their host kimberlites (BHH - (Eccles *et al.*, 2004); Renard -(Patterson *et al.*, 2009); Nikos - (Schmidberger and Francis, 1999). The compositional variation of the pelletal lapilli define distinct linear arrays in plots of Mg versus Si, Ca and C, that intersect the arrays of their host kimberlite whole-rock (figures 3-6 – 3-8). The SiO_2 content of the intersection ranges from 10 to 20 wt% (BHH – 15 wt%, Nikos – 10 wt% and Renard – 20 wt%) and the MgO content ranges from 15 to 30 wt% (BHH and Nikos – 15 wt% and Renard – 30 wt%). CaO and range from 20 to 30 wt% (BHH – 25 wt%, Nikos – 30 wt% and Renard – 20 wt%). Although, the composition of the intersection point differs slightly in each of the three kimberlite suites, all three share similarly low SiO_2 and MgO contents plus high CaO and CO_2 contents.

The Nikos data is enigmatic given that in a plot of Mg versus C (figure 3-6) the intersection point is at a low-C content (~10 cations) and a high-Mg content (~40 cation). However, in terms of Mg versus Si and Ca, the intersection point exhibits a lower Mg content of ~20 cations. Therefore the trend in the Mg versus C plot appears to be an artifact of the whole-rock data distribution that may be the result of the limited sample population size. The low CO_2 content of the intersection in the Nikos suite is inconsistent with the high carbonate contents of the Nikos samples. The Buffalo Head Hills kimberlite suite exhibits a large deviation in MgO contents between the pelletal lapilli and whole-rock compositional arrays that produces a clear intersection point (figure 3-7). The BHH intersection point has low SiO_2 and MgO contents (~15 cation respectively) and high CaO and CO_2 contents (~25 cation respectively). Although the Renard kimberlite suite exhibits less deviation between the pelletal lapilli and whole-rock array than the BHH kimberlite suite does, the intersection point is still distinctive (figure 3-8). The composition of the Renard kimberlite intersection point also has a low SiO_2 content (~20 cation), however, its MgO content is the highest of the three kimberlite suites (~30 cations) and has high CaO and CO_2 contents (~20 cation respectively).

Calculated Magma Composition

The composition of the Nikos kimberlite magma has been previously estimated using the xenocrystic mantle extraction method (Patterson and Francis, 2013). The xenocrystic mantle extraction method extracts an average cratonic mantle composition from the average kimberlite whole-rock composition until the forsterite content of an olivine that would crystalize from the residual composition is equal to the forsterite content of magmatic olivine overgrowths on xenocrystic olivine cores, i.e. Fo_{89} in the case of the Nikos kimberlite. In this study, we calculated the magma compositions for both the BHH and Renard kimberlite suites employing a similar methodology to that used for the Nikos suites (Table 3-3). Magmatic overgrowth compositions are not known for the BHH or Renard, therefore Fo_{89} was also used for these kimberlite suites. The calculated compositions have low SiO_2 contents (9-22 wt %), low MgO (9-20 wt%), and have Mg#'s between 0.69-0.79. Their CaO and CO_2 contents, however, are high (22-32 and 18-34 wt% respectively) which results in high carbonate contents, in agreement with the normative mineralogy calculated on each of the magma compositions. The compositions of the intersection point and calculated magma are very similar in terms of SiO_2 and CO_2. The low CO_2 content of the Nikos intersection point is in contrast to the high CO_2 contents of both the whole-rock and pelletal lapilli data.

Discussion

Recent studies of pelletal lapilli in kimberlite have described them as discrete, smooth, spherical to elliptical inclusions that are commonly comprised of a xenocrystic crystal at their center, which is mantled by micro-porphyritic juvenile material (Stoppa *et al.*, 2011). Pelletal lapilli are thought to be the products of volatile-rich magmatism that are genetically related to magma fluidization and/or fragmentation. As the melt temperature approaches the liquidus, gas foaming (CO_2 and H_2O) occurs (Hampton and Bailey, 1984; Wilson and Head III, 2007) and leads to extensive fragmentation in a gas-fluidized system (Lloyd and Stoppa, 2003; Stoppa *et al.*, 2011). Kimberlite magmas have very high initial CO_2 contents (40 wt%) and the assimilation of orthopyroxene during ascent has been proposed to promote the release of large volumes of CO_2 (Bailey, 1984; Russell *et al.*, 2012). The evidence that pelletal lapilli form at the stage of magma fragmentation suggests that kimberlite lapilli form during the gas foaming stage in kimberlite ascent. Russell et al. (2012) indicates that the kimberlite magma composition at the time of the fragmentation, therefore at the time of pelletal lapilli formation, will contain a considerable assimilated orthopyroxene component (~20 wt % of the entrained mantle composition). In addition, the fact that the most common nuclei in kimberlite pelletal lapilli are mantle olivine (Fo_{90-93}) and not crustal fragments that are common in kimberlite breccia suggests that the lapilli formed at depth before crustal contamination.

The composition of primary kimberlite magma has proven to be a difficult and an elusive entity to constrain, thus leaving a clear vacancy in the kimberlite community's understanding of kimberlites. A common approach to estimating the composition of parental kimberlite magma is to mathematically extract a proportion of cratonic mantle composition from kimberlite whole-rock composition (Kopylova *et al.*, 2007; Kjarsgaard *et al.*, 2009; Patterson *et al.*, 2009). This approach has been adopted because the abundance of xenocrystic olivine in kimberlite is thought to be sourced from disaggregated cratonic mantle. It is further assumed that the cratonic orthopyroxene (notably missing from kimberlite mineralogy) has been assimilated. The proportion of cratonic mantle composition to is based on the proportion of xenocrystic olivine thought to be present in the kimberlites modal mineralogy. The preceding extraction method has yielded a range of estimated kimberlite magma compositions (Kopylova *et al.*, 2007; Kjarsgaard *et al.*, 2009; Patterson *et al.*, 2009) reflecting the amount of cratonic mantle that has been extracted. Many of the proposed kimberlite magma composition have Fe/Mg ratios that would crystallize very high magnesian olivine ($Fo_{>95}$), which are unrepresentative of kimberlite olivine populations. Moreover, most of the high-magnesian olivine in kimberlite is considered to be xenocrystic, and therefore unrelated to the composition of the primary kimberlite magma.

Kimberlite whole-rock data exhibits well developed compositional arrays that are assumed to reflect the compositional variation imparted on kimberlite magma by the entrainment of variable amounts of xenocrystic mantle. Further support for the xenocrystic mantle extraction method is evidenced by the fact that the well-developed compositional trends exhibited by the kimberlite whole-rock data can be projected to higher magnesium contents that coincide with the composition of cratonic mantle. The ideology of the xenocrystic mantle extraction method demands that the composition of primary kimberlite magma also resides at lower magnesium contents on the trend formed by kimberlite whole-rock data and that of cratonic mantle.

The xenocrystic nuclei of pelletal lapilli are most frequently single olivine grains with compositions greater than Fo_{90}. The rarity of crustal lithic nuclei, despite the abundance of crustal lithic fragments in host kimberlites, suggests that pelletal lapilli form before substantial crustal contamination. However, magma fragmentation is a key requirement for pelletal lapilli formation (Lloyd and Stoppa, 2003), therefore early pelletal lapilli formation suggests that kimberlite magma may undergo fragmentation at depth. The assimilation of orthopyroxene in kimberlite magma may, however, explain this fragmentation enigma. The absence of xenocrystic orthopyroxene in kimberlite is attributed to its instability in kimberlite magma (Luth, 2009). A consequence of orthopyroxene assimilation is to decrease the solubility of CO_2 in the melt, thereby driving deep-seated exsolution and effervescence of a CO_2-rich volatile phase (Russell *et al.*, 2012). Thus, the compositions of pelletal lapilli mantles may represent that of kimberlite liquids before crustal contamination and possibly as early as orthopyroxene assimilation in the evolving kimberlite magma.

Kimberlite pelletal lapilli exhibit well-developed compositional arrays in plots of Mg versus Si, Ca and CO_2 (figures 3-6 – 3-8) that are distinct from those of the kimberlite whole-rocks and project toward the composition of serpentine from the composition of calcite in the carbon-rich direction. This trend is also exhibited in the compositional arrays formed by the individual spot analyses data within single pelletal lapilli. The compositional variation of the foregoing simply reflects the relationship between serpentine and carbonate mineral abundance in areas analyzed and is evident in the image analysis of the areas (figure 3-4). The breadth of the variation in the pelletal lapilli data is similar to that exhibited by their host kimberlite whole-rock data; for instance the SiO_2 content of lapilli in the BHH kimberlite varies from 26 to 35 wt% and CO_2 content from 3 to 14 wt%. The compositional variation exhibited by the kimberlite whole-rock data is assumed to reflect the entrainment of variable amounts of xenocrystic mantle, thus it is likely that the similar variation exhibited by the pelletal lapilli data has a similar explanation, but the projection toward serpentine is perplexing.

Serpentine in kimberlite typically occurs as retrograde deuteric reaction rims on relict olivine cores (Mitchell, 2008). The ubiquitous serpentine found in the mantles of pelletal lapilli, however, is unlikely to be the products of serpentinization because the lapilli often have unaltered olivine nuclei. The existence of magmatic serpentine in kimberlite magmas has been proposed (Mitchell and Putnis, 1988; Mitchell, 2008) and been demonstrated experimentally to form at very low temperatures (300 °C) from Mg–Si-gels (Devouard *et al.*, 1997). Magmatic serpentine is commonly a very fine-grained mixture of chrysotile and polygonal serpentine intergrown with calcite and/or dolomite (Mitchell and Putnis, 1988). The subhedral to euhedral serpentine within finer grained calcite found in the mantles of the pelletal lapilli is thus consistent with magmatic origin. The proposed crystallization sequence for kimberlites is (>1200 °C) olivine (as overgrowths on olivine xenocrysts; (Patterson and Francis, 2013) and Cr-rich spinel, followed by (1000–800 °C) groundmass Ti–Mg–Fe-rich spinels, perovskite, monticellite, apatite, phlogopite, (>650 °C) calcite or dolomite, and (>300 °C) serpentine (Canil and Bellis, 2008; Mitchell, 2008). Crystallization of kimberlite magma is thought to be driven by the assimilation of orthopyroxene (Mitchell, 2008; Brett *et al.*, 2009; Pilbeam *et al.*, 2011; Patterson and Francis, 2013).

The compositional arrays exhibited by the pelletal lapilli and kimberlite whole-rock data intersect (figures 3-6 – 3-8) at a composition that is similar to the estimated magma compositions from the xenocrystic mantle extraction method in terms of the major elements (SiO_2, CaO, MgO and CO_2). The calculated magma compositions for the Nikos kimberlite is in equilibrium with the magmatic olivine overgrowths found in the Nikos kimberlite (Patterson and Francis, 2013). The similarity of the composition of the intersection of the lapilli and whole rock arrays to the kimberlite magma composition calculated by the xenolith extraction techniques suggest that the intersection represents the composition of kimberlite magma for each suite.

Conclusions

Pelletal lapilli are often too small for conventional XRF analysis, however, a comparison of the results of EMP and XRF (plus thermo-combustion) analysis indicates that representative compositions of small pelletal lapilli can be obtained using averaged EMP analyses. The compositional variation of pelletal lapilli reflects the variable amounts of serpentine and carbonate not only within single spot analyses, but also in the bulk mineralogy of the lapilli mantle. The compositional arrays kimberlite whole-rock and pelletal lapilli data intersect in binary plots at compositions that are similar to that of the magma composition estimated by the mantle xenocryst extraction method. Our estimates of kimberlite magma compositions are significantly poorer in MgO (~11-13 wt%) and higher in CO_2 (~25-32 wt%) than previous estimates.

References

Bailey, D. K. (1984). Kimberlite: "The mantle sample' formed by ultrametasomatism. 3rd International Kimberlite Conference.

Brett, R. C., J. K. Russell and S. Moss (2009). Origin of olivine in kimberlite: Phenocryst or impostor? Lithos **112, Supplement 1**(0): 201-212.

Canil, D. and A. J. Bellis (2008). Phase equilibria in a volatile-free kimberlite at 0.1 MPa and the search for primary kimberlite magma. Lithos **105**(1-2): 111-117.

Devouard, B., A. Baronnet, G. van Tendeloo and S. Amelinckx (1997). First evidence of synthetic polygonal serpentines. European Journal of Mineralogy **9**(3): 539-546.

Eccles, D. R., L. M. Heaman, R. W. Luth and R. A. Creaser (2004). Petrogenesis of the Late Cretaceous northern Alberta kimberlite province. Lithos **76**(1): 435-459.

Hampton, C. M. and D. K. Bailey (1984). Gas extraction experiments on volcanic glasses. Journal of Non-Crystalline Solids **67**(1–3): 147-168.

Kjarsgaard, B. A., D. G. Pearson, S. Tappe, G. M. Nowell and D. P. Dowall (2009). Geochemistry of hypabyssal kimberlites from Lac de Gras, Canada: Comparisons to a global database and applications to the parent magma problem. Lithos **112**(Supplement 1): 236-248.

Kopylova, M. G., S. Matveev and M. Raudsepp (2007). Searching for parental kimberlite melt. Geochimica et Cosmochimica Acta **71**(14): 3616-3629.

Lloyd, F. E. and F. Stoppa (2003). Pelletal lapilli in diatremes—some inspiration from the old masters. Geolines **15**: 65-71.

Luth, R. (2009). The activity of silica in kimberlites, revisited. Contributions to Mineralogy and Petrology **158**(2): 283-294.

Mitchell, R. H. (1986). Kimberlites : mineralogy, geochemistry, and petrology. New York, Plenum.

Mitchell, R. H. (1997). Kimberlites, orangeites, lamproites, melilitites and minettes: a petrographic atlas, Almaz Press.

Mitchell, R. H. (2008). Petrology of hypabyssal kimberlites: Relevance to primary magma compositions. Journal of Volcanology and Geothermal Research **174**(1-3): 1-8.

Mitchell, R. H. and A. Putnis (1988). Polygonal serpentine in segregation-textured kimberlite. The Canadian Mineralogist **26**(4): 991-997.

Patterson, M. and D. Francis (2013). The implications of magmatic margins on xenocrystic olivine for kimberlite magma
composition. Journal of Petrology.

Patterson, M., D. Francis and T. McCandless (2009). Kimberlites: Magmas or mixtures? Lithos **112**(Supplement 1): 191-200.

Pilbeam, L. H., T. F. D. Nielsen and T. E. Waight (2011). Melt compositions and processes in the kimberlite provience of southern West Greenland. Goldschmidt. Prague, Mineralogical Magazine. **75:** 1643.

Russell, J. K., L. A. Porritt, Y. Lavallee and D. B. Dingwell (2012). Kimberlite ascent by assimilation-fuelled buoyancy. Nature **481**(7381): 352-356.

Schmidberger, S. S. and D. Francis (1999). Nature of the mantle roots beneath the North American craton: mantle xenolith evidence from Somerset Island kimberlites. Lithos **48**(1–4): 195-216.

Stoppa, F., F. E. Lloyd, A. Tranquilli and M. Schiazza (2011). Comment on: Development of spheroid “composite” bombs by welding of juvenile spinning and isotropic droplets inside a mafic “eruption” column by Carracedo Sánchez et al. (2009). Journal of Volcanology and Geothermal Research **204**(1–4): 107-116.

Wilson, L. and J. W. Head III (2007). An integrated model of kimberlite ascent and eruption. Nature **447**(7140): 53-57.

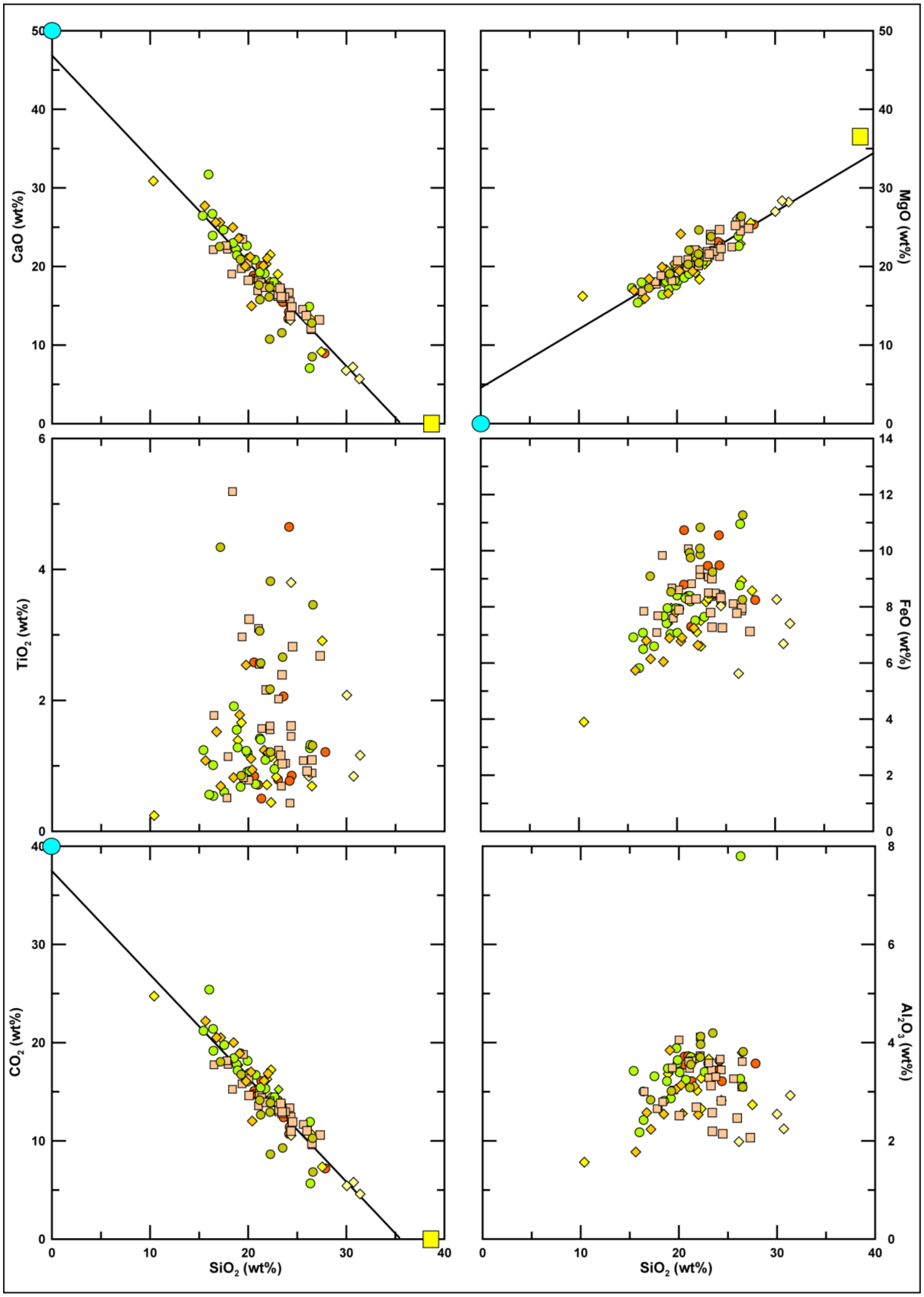

Figure 3-1A: Nikos kimberlite pelletal lapilli EMP data presented in Harker type diagrams comparing major elements with SiO_2. Different symbols and colors for each lapillus analyzed. Large cyan circle and yellow square represent calcite and serpentine respectively.

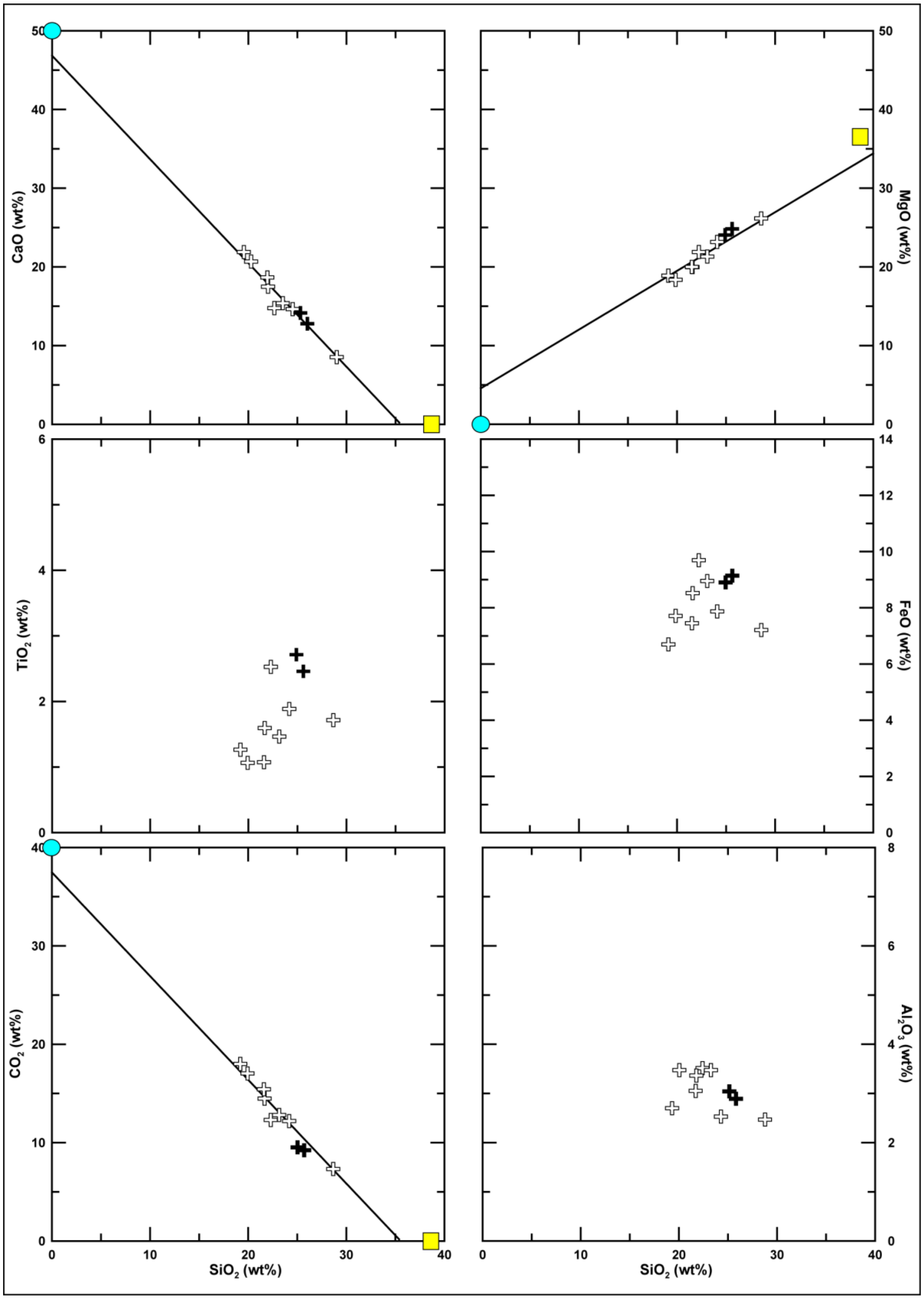

Figure 3-1B: Average Nikos kimberlite pelletal lapilli EMP data (open crosses) and XRF data (filled crosses) presented in Harker type diagrams comparing major elements with SiO_2. Large cyan circle and yellow square represent calcite and serpentine respectively.

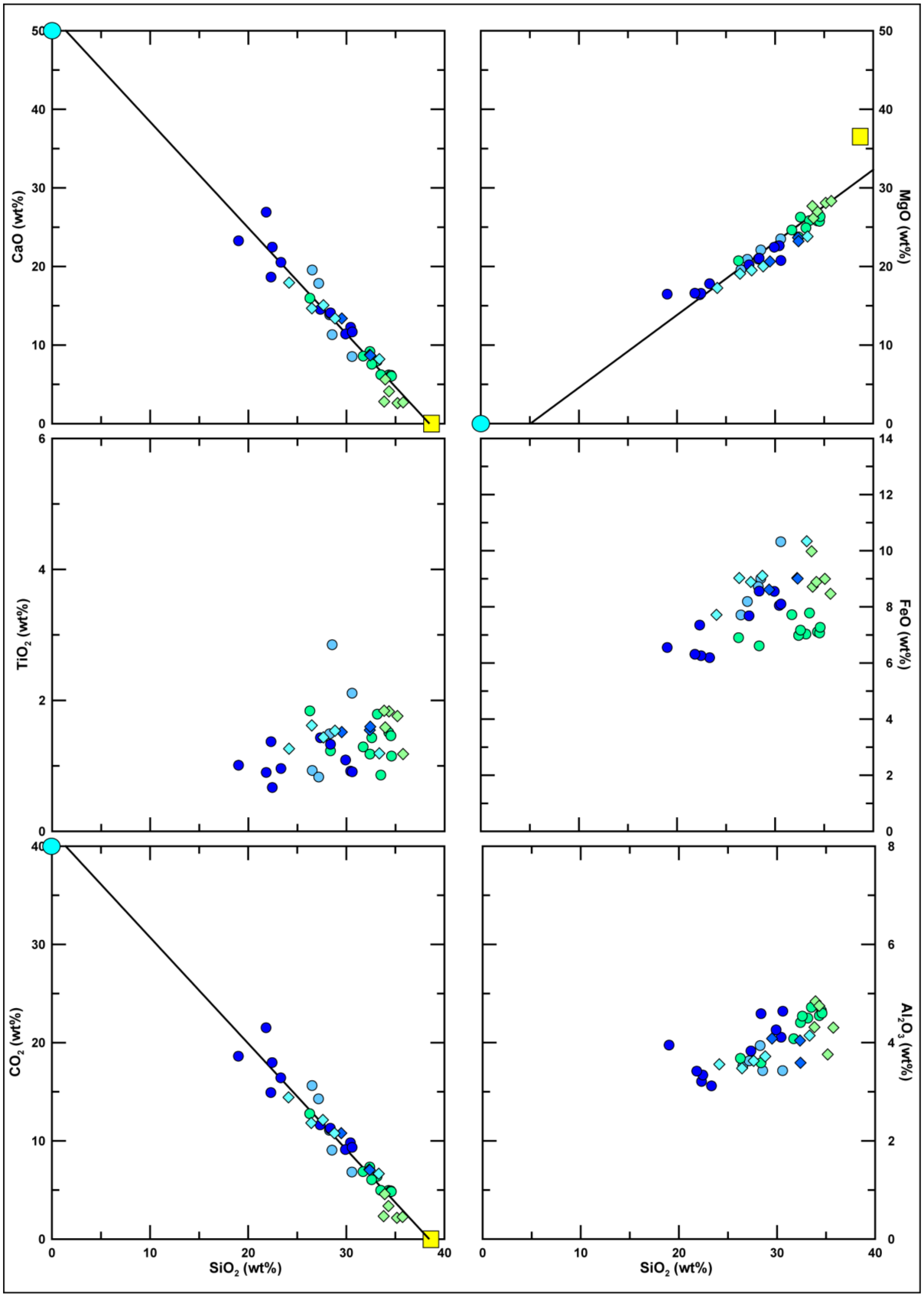

Figure 3-2A: Buffalo Head Hills kimberlite pelletal lapilli EMP data presented in Harker type diagrams comparing major elements with SiO_2. Different symbols and colors for each lapillus analyzed. Large cyan circle and yellow square represent calcite and serpentine respectively.

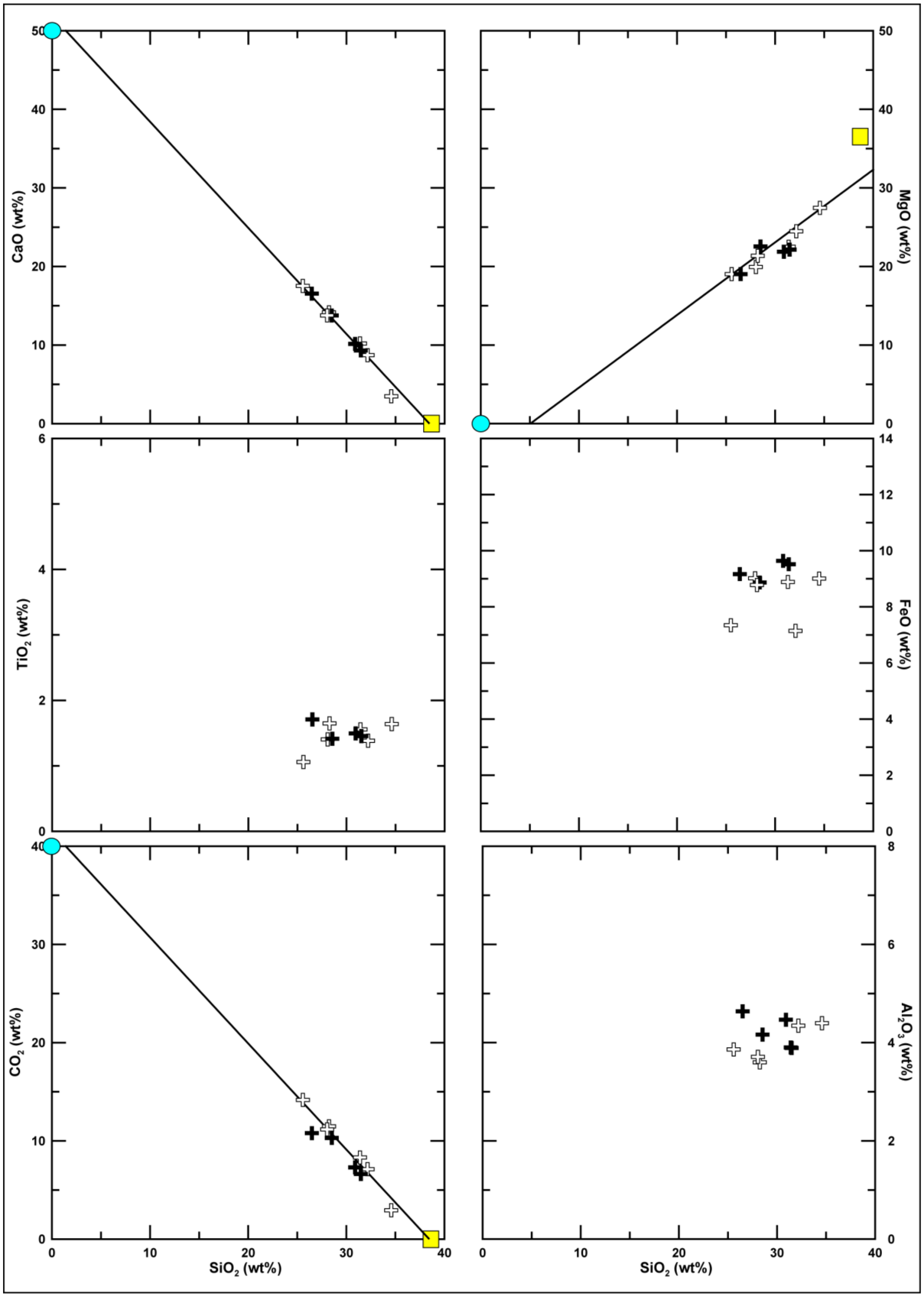

Figure 3-2B: Average BHH kimberlite pelletal lapilli EMP data (open crosses) and XRF data (filled crosses) presented in Harker type diagrams comparing major elements with SiO_2. Large cyan circle and yellow square represent calcite and serpentine respectively.

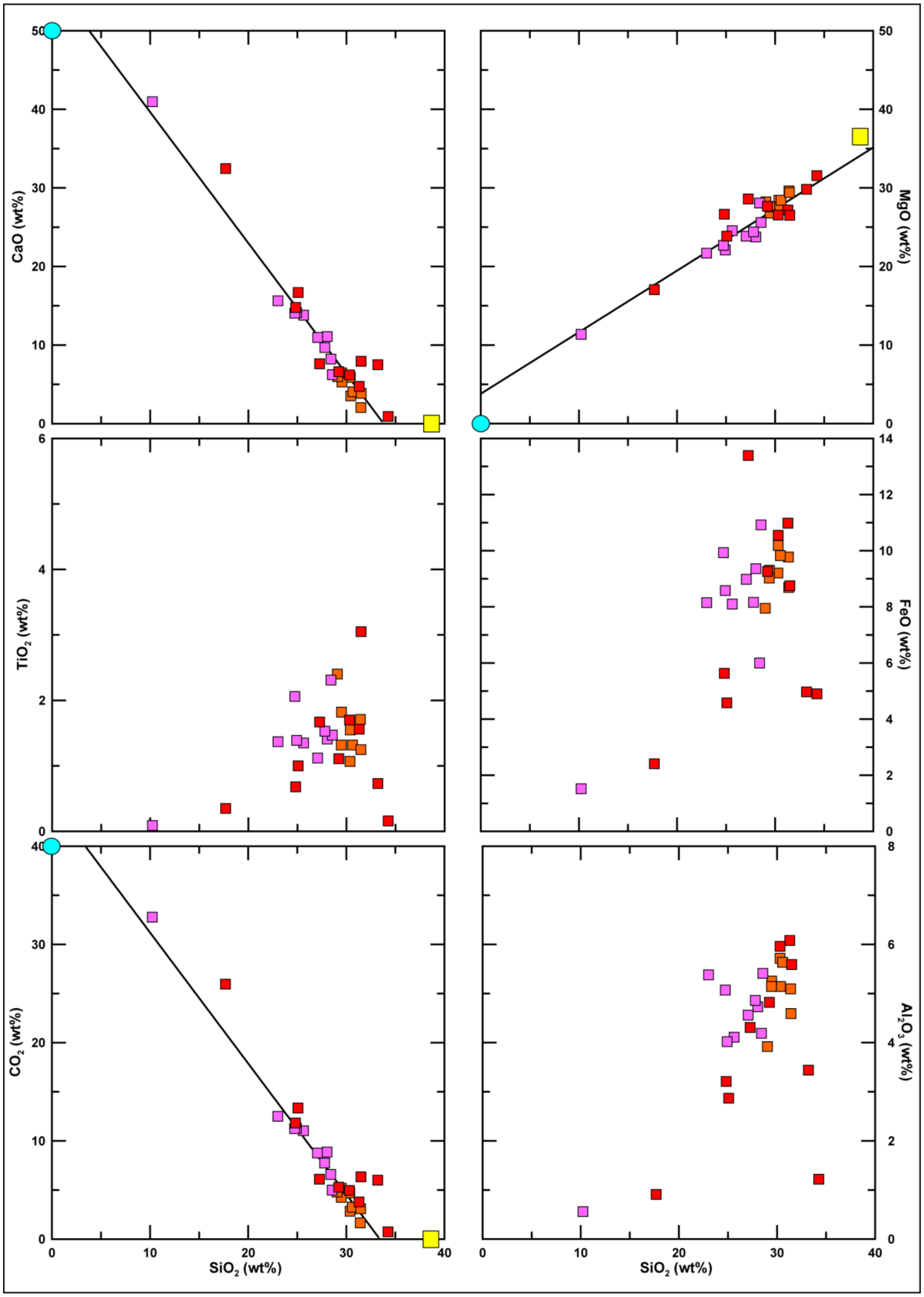

Figure 3-3A: Renard kimberlite pelletal lapilli EMP data presented in Harker type diagrams comparing major elements with SiO_2. Different symbols and colors for each lapillus analyzed. Large cyan circle and yellow square represent calcite and serpentine respectively.

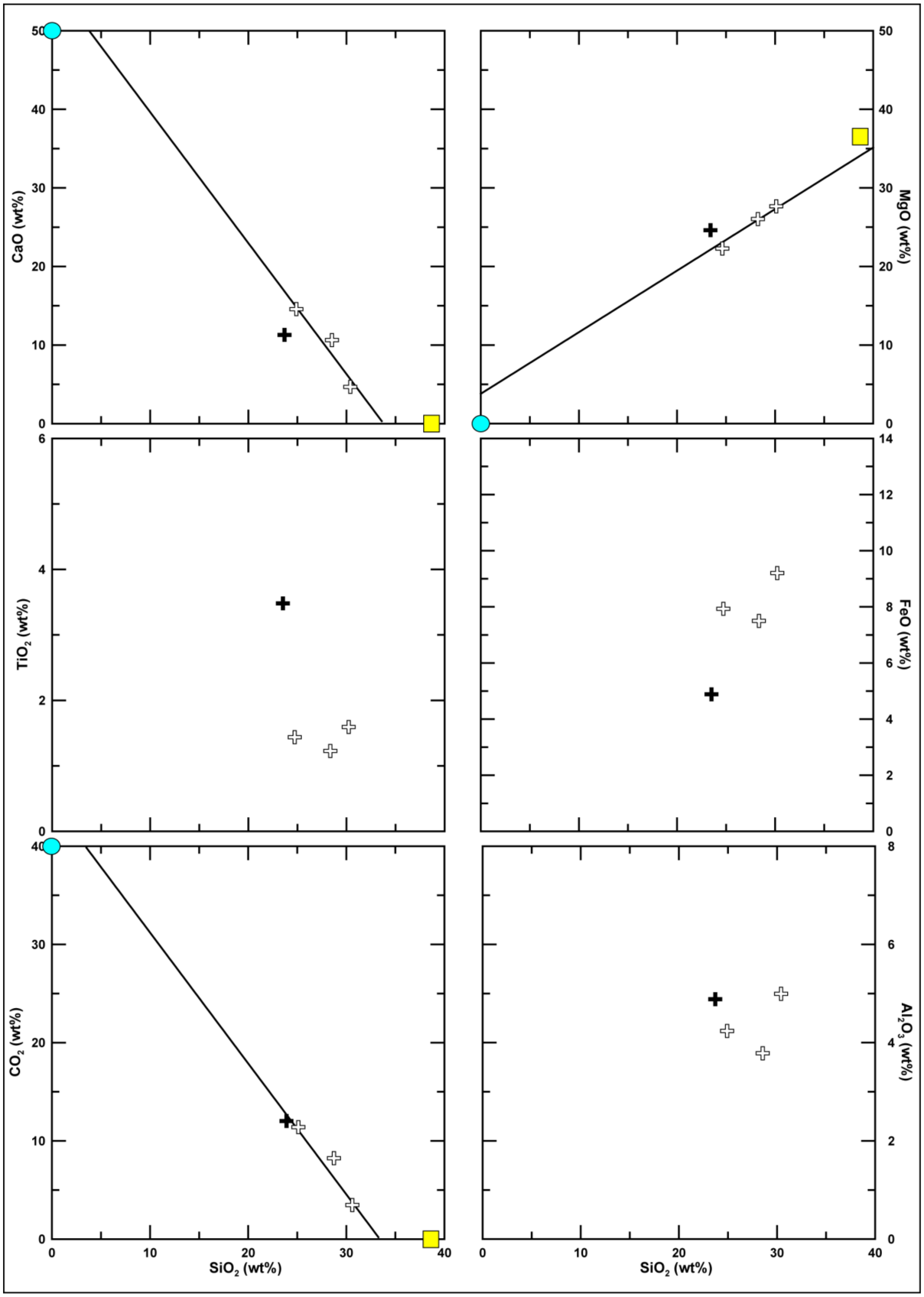

Figure 3-3B: Average Renard kimberlite pelletal lapilli EMP data (open crosses) and XRF data (filled crosses) presented in Harker type diagrams comparing major elements with SiO_2. Large cyan circle and yellow square represent calcite and serpentine respectively.

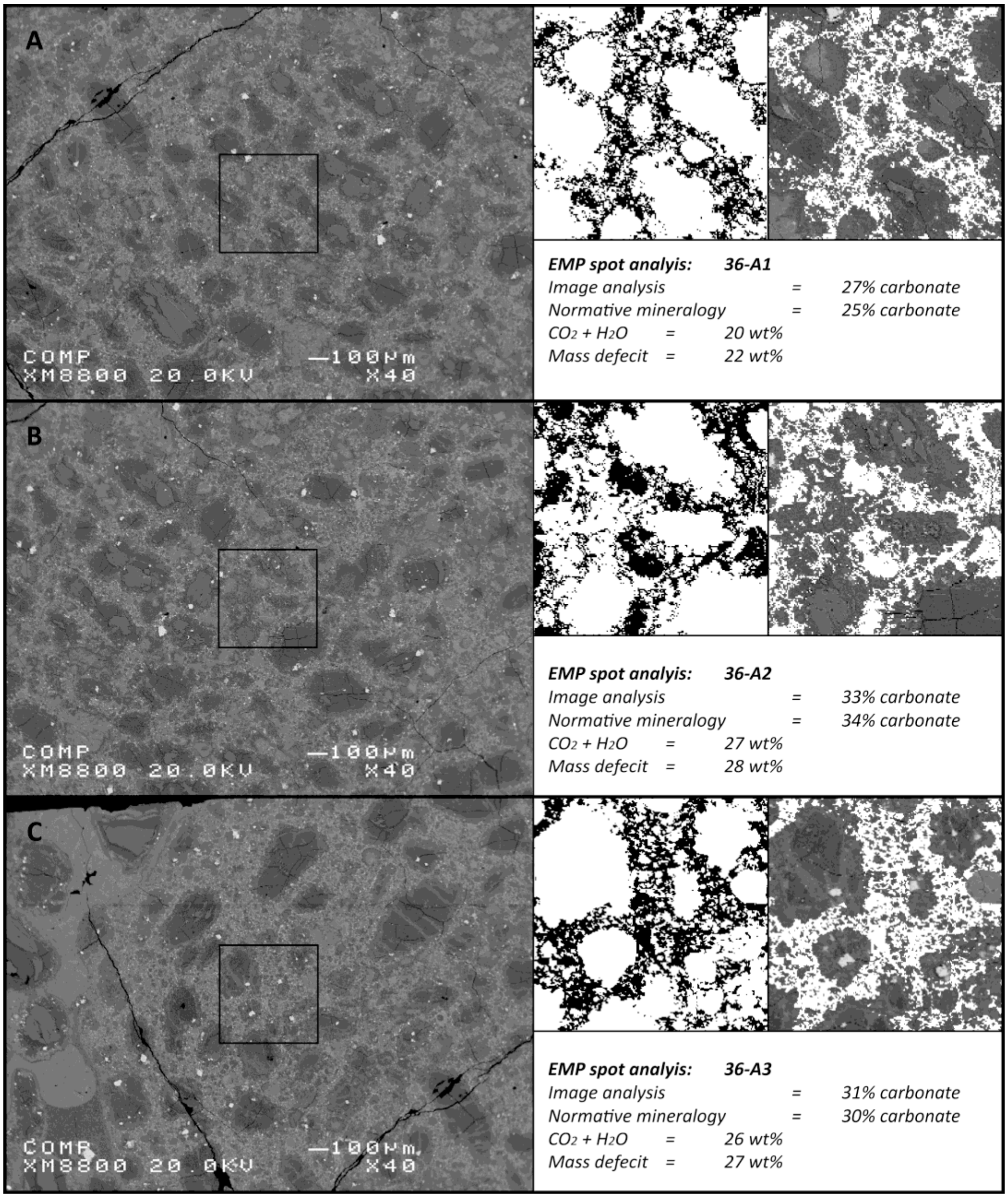

Figure 3-4: Carbonate estimation by image analysis compared with calculated normative carbonate contents and calculated $CO_2 + H_2O$ contents comparison with mass deficit of average EMP analyses.

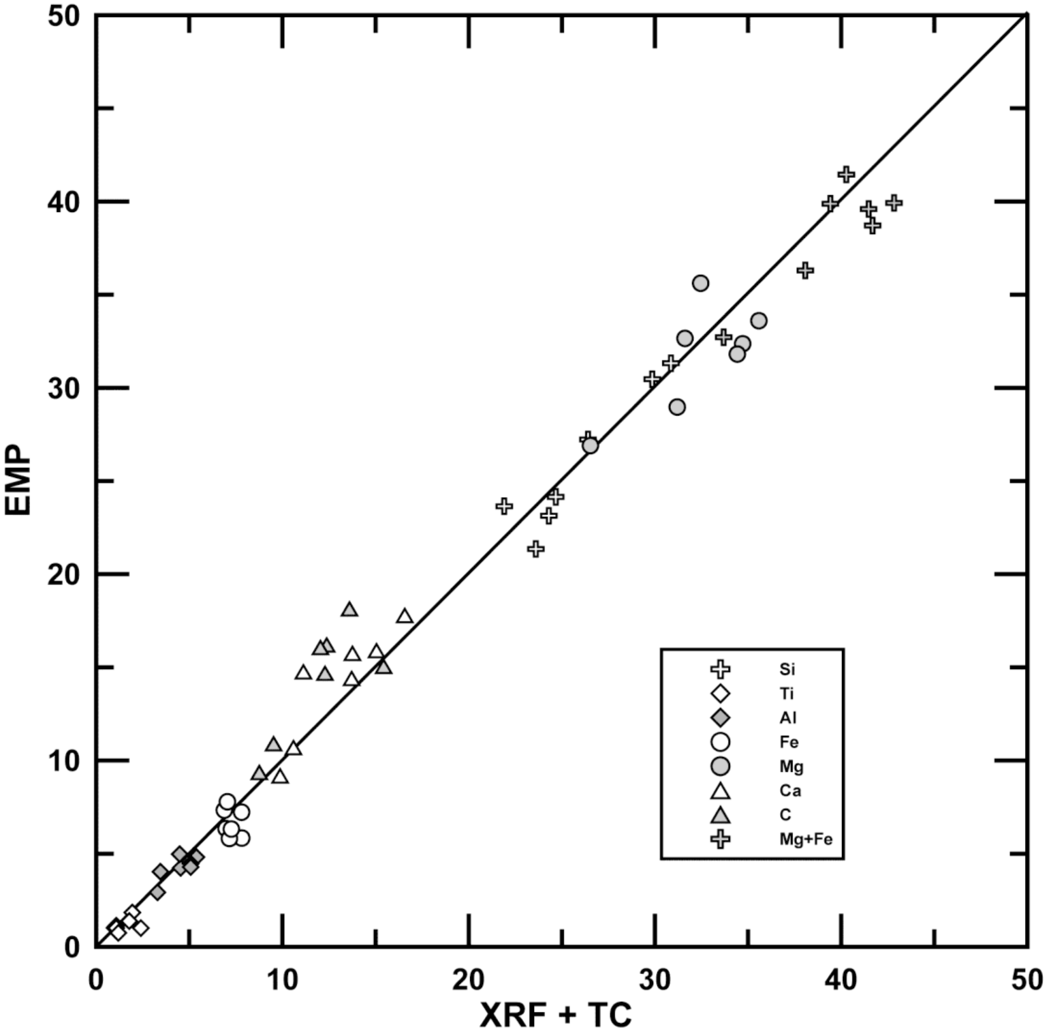

Figure 3-5: Comparing averaged EMP analyses with XRF+TC results for same lapilli. Diagonal line represents one-to-one ratio.

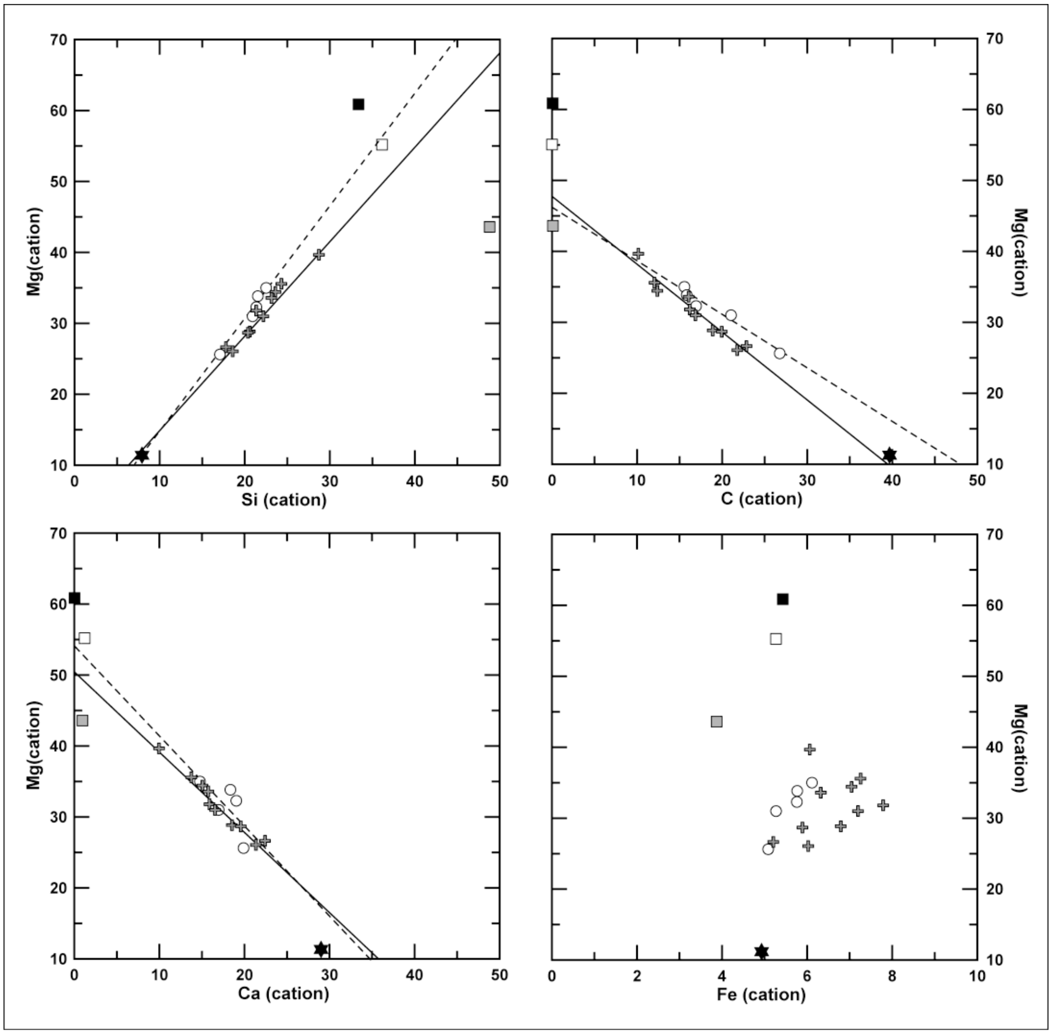

Figure 3-6: Binary plots for the Nikos kimberlite. Circles are kimberlite whole-rock data, crosses are lapilli data (averaged EMP and XRF+TC), stars are calculated magma compositions, black square – olivine, white square – cratonic mantle, grey square – orthopyroxene.

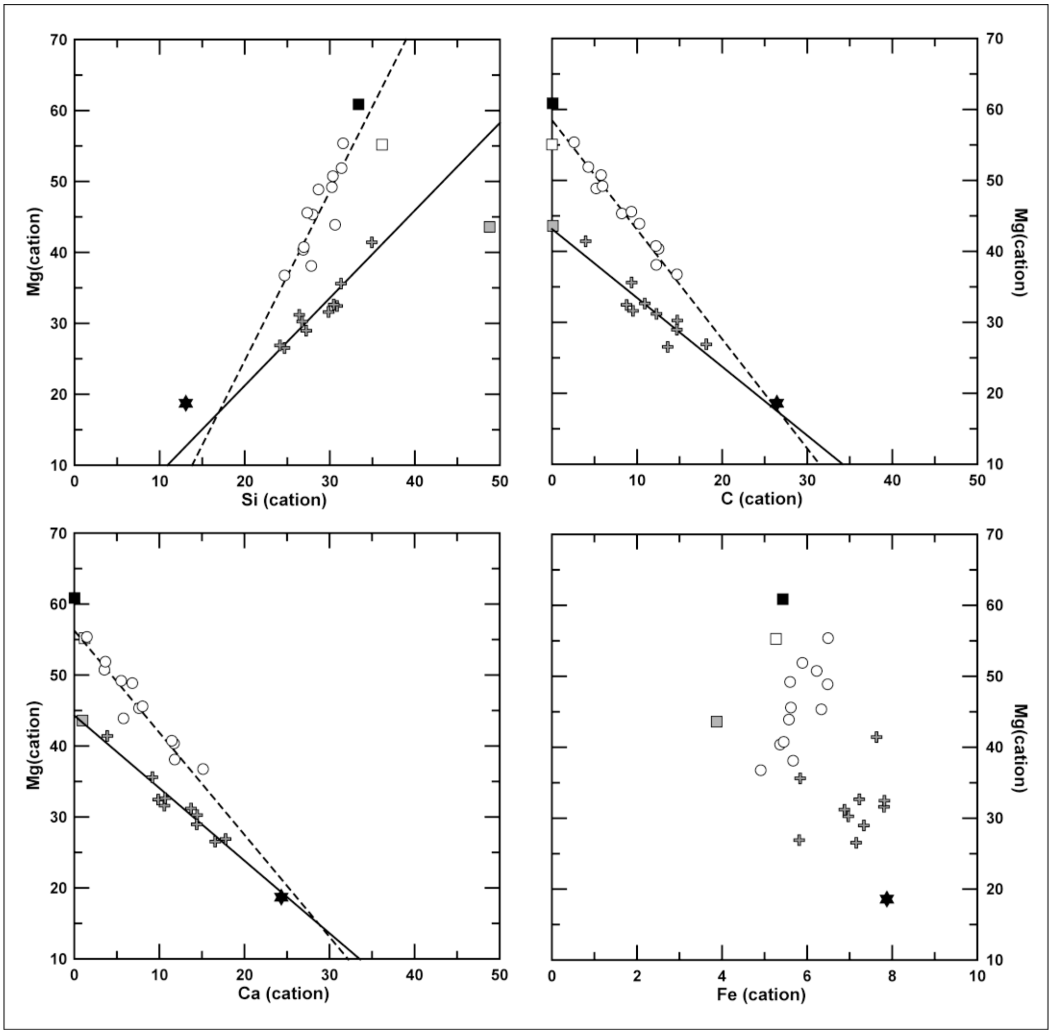

Figure 3-7: Binary plots for the Buffalo Head Hills kimberlite. Circles are kimberlite whole-rock data, crosses are lapilli data (averaged EMP and XRF+TC), stars are calculated magma compositions, black square – olivine, white square – cratonic mantle, grey square – orthopyroxene.

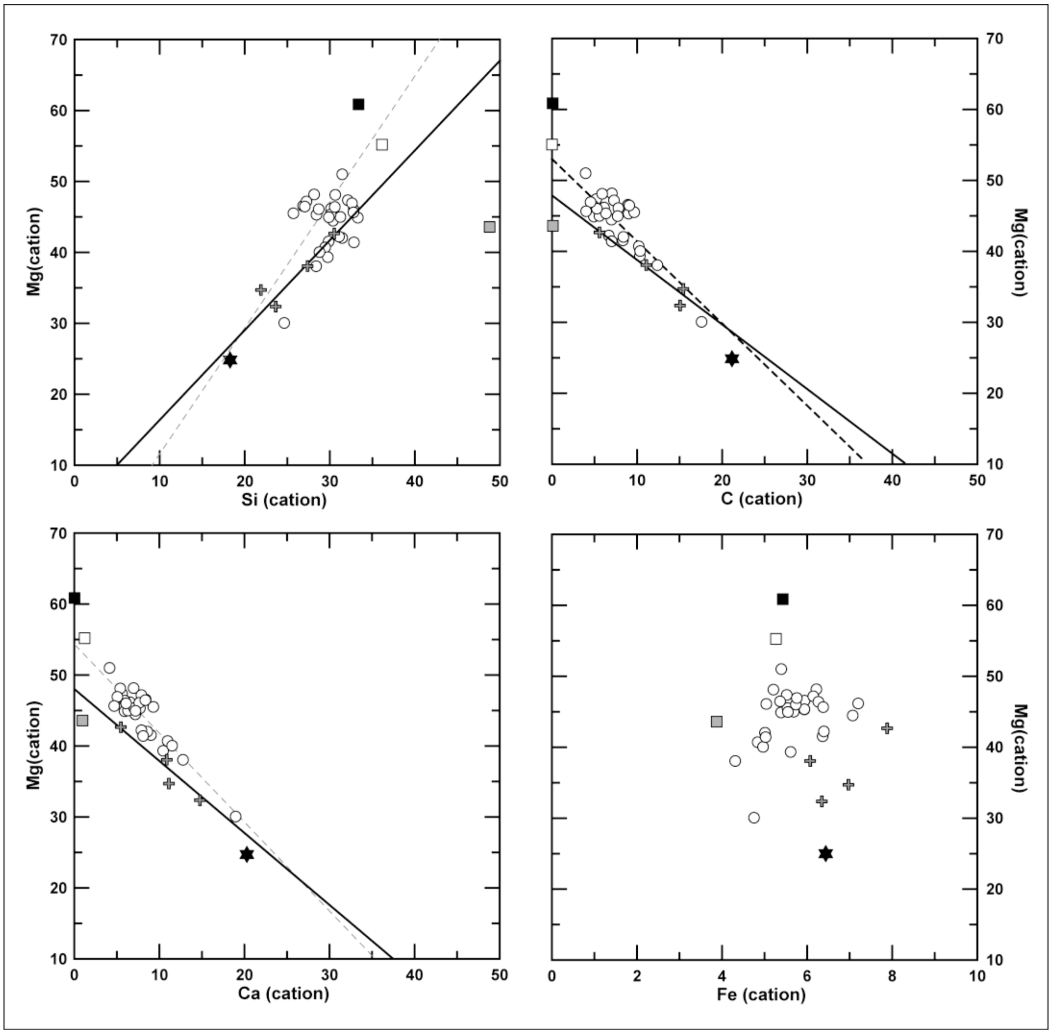

Figure 3-8: Binary plots for the Renard kimberlite Circles are kimberlite whole-rock data, crosses are lapilli data (averaged EMP and XRF+TC), stars are calculated magma compositions, black square – olivine, white square – cratonic mantle, grey square – orthopyroxene.

Table 1: EMP analysis (individual spot analyses and averages)

Spot	Sample	SiO_2	TiO_2	Al_2O_3	FeO	MgO	MnO	CaO	Na_2O	K_2O	CO_2	Total
Buffalo Head Hills												
L27	42B-A1	33.1	1.8	4.5	7.0	24.9	0.2	8.0	0.2	1.9	6.4	88.0
L28	42B-A2	33.5	0.9	4.7	7.8	25.8	0.2	6.2	0.1	1.4	5.0	85.6
L29	42B-A3	32.4	1.2	4.4	7.0	23.8	0.2	9.2	0.2	1.9	7.3	87.5
L30	42B-A4	31.7	1.3	4.1	7.7	24.6	0.2	8.6	0.1	1.5	6.9	86.6
L31	42B-A5	32.6	1.4	4.5	7.2	26.3	0.2	7.6	0.1	1.5	6.1	87.3
L32	42B-A6	34.3	1.5	4.6	7.1	25.8	0.2	6.2	0.2	2.1	5.0	86.9
L33	42B-A7	34.5	1.5	4.7	7.1	25.8	0.2	6.2	0.3	2.0	4.9	87.0
L34	42B-A8	28.4	1.2	3.6	6.6	21.1	0.2	14.0	0.2	2.4	11.2	88.8
L35	42B-A9	26.3	1.8	3.7	6.9	20.7	0.2	16.0	0.2	1.8	12.8	90.3
L36	42B-A10	34.6	1.2	4.6	7.3	26.4	0.2	6.0	0.2	1.8	4.8	86.9
L37	42B-B1	35.1	1.8	3.8	9.0	28.1	0.2	2.6	0.1	0.9	2.1	83.7
L38	42B-B2	33.9	1.6	4.8	8.7	26.2	0.2	5.6	0.1	1.4	4.5	86.9
L39	42B-B3	34.3	1.8	4.7	8.9	27.0	0.2	4.1	0.1	1.2	3.3	85.6
L40	42B-B4	35.7	1.2	4.3	8.5	28.3	0.2	2.7	0.1	0.8	2.2	84.0
L41	42B-B5	33.8	1.8	4.3	10.0	27.7	0.2	2.8	0.1	0.7	2.3	83.7
L47	37-A1	30.6	2.1	3.4	10.3	23.5	0.2	8.5	0.1	1.3	6.8	86.9
L48	37-A2	28.5	2.9	3.4	9.0	22.1	0.1	11.3	0.1	1.0	9.1	87.5
L49	37-A3	26.5	0.9	3.5	7.7	19.6	0.1	19.6	0.1	1.2	15.6	94.8
L50	37-A4	27.2	0.8	3.6	8.2	20.9	0.1	17.9	0.1	0.8	14.3	93.8
L51	37-A5	28.3	1.5	3.9	8.7	20.9	0.1	13.9	0.2	1.5	11.1	90.1
L57	36-A1	28.4	1.3	4.6	8.6	21.0	0.2	14.1	0.2	1.7	11.3	91.3
L58	36-A2	19.0	1.0	4.0	6.6	16.5	0.2	23.3	0.1	1.5	18.6	90.7
L59	36-A3	23.3	1.0	3.1	6.2	17.8	0.2	20.5	0.1	1.2	16.4	89.8
L60	36-A4	30.4	0.9	4.1	8.1	22.6	0.2	12.3	0.1	1.2	9.8	89.7
L61	36-A5	22.3	1.4	3.2	7.4	16.4	0.2	18.7	0.1	1.1	14.9	85.6
L62	36-A6	22.4	0.7	3.3	6.3	16.6	0.2	22.5	0.1	1.4	18.0	91.4
L63	36-A7	27.3	1.4	3.8	7.7	20.2	0.2	14.5	0.1	1.2	11.6	88.1
L64	36-A8	29.9	1.1	4.3	8.6	22.5	0.2	11.4	0.2	1.6	9.1	88.7
L65	36-A9	21.8	0.9	3.4	6.3	16.6	0.2	26.9	0.1	1.5	21.5	99.2
L66	36-A10	30.6	0.9	4.6	8.1	20.8	0.2	11.7	0.3	2.6	9.3	89.1

Spot	Sample	SiO_2	TiO_2	Al_2O_3	FeO	MgO	MnO	CaO	Na_2O	K_2O	CO_2	Total
L67	*36-B1*	26.4	1.6	3.5	9.0	19.2	0.2	14.7	0.1	1.2	11.7	87.6
L68	*36-B2*	24.1	1.3	3.6	7.7	17.4	0.2	17.9	0.1	1.6	14.3	88.1
L69	*36-B3*	33.3	1.2	4.1	10.4	23.9	0.2	8.2	0.1	1.5	6.6	89.4
L70	*36-B4*	27.6	1.4	3.6	8.9	19.6	0.2	15.0	0.2	1.3	12.0	89.8
L71	*36-B5*	28.8	1.5	3.7	9.1	20.1	0.2	13.4	0.1	1.4	10.7	88.9
L72	*36-C1*	32.3	1.5	4.0	9.0	23.7	0.2	8.8	0.2	1.4	7.0	88.1
L73	*36-C2*	32.4	1.6	3.6	9.0	23.3	0.2	8.7	0.2	1.1	7.0	86.9
L74	*36-C3*	29.5	1.5	4.1	8.6	20.7	0.2	13.4	0.3	2.2	10.7	91.0
Nikos												
L75	*NK1-A-A1*	22.3	1.2	4.1	9.9	20.5	0.2	17.3	0.1	0.8	13.9	90.2
L76	*NK1-A-A2*	21.2	3.1	3.1	9.9	20.3	0.2	17.7	0.1	0.5	14.1	90.2
L77	*NK1-A-A3*	22.2	2.2	3.7	10.1	21.6	0.2	16.2	0.1	0.5	12.9	89.7
L78	*NK1-A-A4*	22.3	3.8	4.0	10.8	24.6	0.3	10.8	0.2	0.5	8.6	85.9
L79	*NK1-A-A5*	23.5	2.7	4.2	9.2	23.8	0.2	11.6	0.2	0.9	9.3	85.5
L80	*NK1-A-A6*	21.3	2.6	3.6	9.8	22.1	0.3	15.8	0.1	0.4	12.7	88.5
L81	*NK1-A-A7*	19.3	0.9	3.0	8.5	19.1	0.2	20.9	0.1	0.5	16.7	89.2
L82	*NK1-A-A8*	26.5	1.3	3.1	8.3	26.4	0.2	12.8	0.0	0.5	10.3	89.4
L83	*NK1-A-A9*	17.2	4.3	2.9	9.1	17.3	0.3	22.5	0.1	0.5	18.0	92.3
L84	*NK1-A-A10*	26.6	3.5	3.8	11.3	26.4	0.3	8.6	0.0	0.8	6.8	88.0
L85	*NK1-A-B1*	21.8	2.2	2.7	8.3	22.1	0.2	17.4	0.1	0.5	13.9	89.1
L86	*NK1-A-B2*	23.5	1.0	2.2	7.3	24.1	0.2	16.0	0.0	0.4	12.8	87.4
L87	*NK1-A-B3*	26.5	1.1	3.1	8.0	25.7	0.2	12.2	0.1	0.7	9.7	87.2
L88	*NK1-A-B4*	26.0	0.9	2.5	7.8	25.2	0.1	13.8	0.1	0.5	11.0	87.8
L89	*NK1-A-B5*	23.4	2.4	2.6	9.0	23.4	0.3	16.2	0.0	0.4	13.0	90.7
L90	*NK1-A-B6*	20.1	3.2	2.5	7.9	20.7	0.2	18.3	0.0	0.5	14.6	88.1
L91	*NK1-A-B7*	27.3	2.7	2.1	7.1	24.8	0.2	13.2	0.1	0.3	10.6	88.3
L92	*NK1-A-B8*	24.4	1.6	2.8	8.3	24.7	0.2	13.7	0.1	0.5	11.0	87.2
L93	*NK1-A-B9*	23.3	1.2	3.1	7.8	21.6	0.1	17.3	0.1	0.6	13.8	88.9
L94	*NK1-A-B10*	24.5	2.8	2.2	7.3	22.3	0.2	14.9	0.0	0.4	11.9	86.4
L95	*NK1-A-C1*	19.8	2.5	3.1	7.8	20.4	0.2	20.1	0.1	0.6	16.1	90.5
L96	*NK1-A-C2*	20.3	1.1	3.2	6.8	19.4	0.2	21.2	0.1	0.8	17.0	90.1
L97	*NK1-A-C3*	21.6	1.2	3.1	7.2	19.4	0.2	20.1	0.1	0.8	16.1	90.0

Spot	Sample	SiO_2	TiO_2	Al_2O_3	FeO	MgO	MnO	CaO	Na_2O	K_2O	CO_2	Total
L98	NK1-A-C4	17.2	0.7	2.3	6.1	18.4	0.2	25.6	0.1	0.5	20.5	91.5
L99	NK1-A-C5	15.7	1.1	1.8	5.7	17.0	0.2	27.7	0.1	0.4	22.2	91.7
L100	NK1-A-C6	16.8	1.5	2.6	6.8	16.0	0.2	25.6	0.1	0.7	20.5	90.7
L101	NK1-A-C7	22.0	1.2	2.6	6.6	21.0	0.2	21.1	0.1	0.8	16.8	92.3
L102	NK1-A-C8	19.1	1.8	3.9	6.9	16.6	0.2	23.6	0.1	1.6	18.9	92.6
L103	NK1-A-C9	20.4	0.9	2.6	6.9	24.1	0.2	15.0	0.0	0.6	12.0	82.8
L104	NK1-A-C10	18.5	0.8	2.6	6.0	19.9	0.1	25.0	0.0	0.6	20.0	93.6
L105	NK1-E-A1	16.5	1.8	3.0	7.8	16.8	0.2	22.2	0.1	0.8	17.7	87.0
L106	NK1-E-A2	18.0	1.1	2.7	7.7	17.7	0.2	22.2	0.1	0.7	17.8	88.1
L107	NK1-E-A3	23.4	0.7	3.5	8.5	21.4	0.2	17.0	0.1	0.8	13.6	89.1
L108	NK1-E-A4	17.8	0.5	2.7	7.1	18.1	0.2	22.7	0.1	0.6	18.1	87.9
L109	NK1-E-A5	23.1	1.2	3.3	9.1	21.9	0.2	16.2	0.1	0.8	13.0	88.8
L110	NK1-E-A6	24.2	0.4	3.7	8.4	21.9	0.1	16.7	0.1	0.8	13.4	89.7
L111	NK1-E-A7	25.6	1.1	3.3	8.1	22.5	0.1	14.6	0.1	0.9	11.7	87.9
L112	NK1-E-A8	21.1	2.6	3.5	8.3	20.9	0.2	18.2	0.1	0.9	14.6	90.3
L113	NK1-E-A9	24.4	1.5	3.5	8.4	21.2	0.2	15.6	0.1	1.0	12.5	88.2
L114	NK1-E-A10	26.5	0.9	3.6	7.9	24.5	0.1	12.0	0.1	1.0	9.6	86.1
L115	NK1-E-A11	23.8	1.0	3.3	8.5	21.9	0.2	16.2	0.1	0.7	13.0	88.6
L116	NK1-E-A12	20.1	0.8	4.1	8.6	20.0	0.2	20.4	0.2	0.8	16.3	91.3
L117	NK1-E-A13	21.4	1.6	3.7	8.8	20.2	0.2	18.0	0.1	0.9	14.4	89.1
L118	NK1-E-A14	18.4	5.2	2.8	9.8	18.8	0.3	19.1	0.1	0.7	15.2	90.4
L119	NK1-E-A15	22.2	1.6	3.8	9.1	20.2	0.2	17.6	0.1	0.9	14.1	89.6
L120	NK1-E-A16	21.0	3.1	3.6	10.1	19.9	0.2	16.9	0.1	0.8	13.6	89.4
L121	NK1-E-A17	19.4	3.0	3.5	8.7	18.5	0.3	19.7	0.1	0.9	15.8	89.9
L122	NK1-E-A18	19.5	0.8	3.1	7.6	18.2	0.2	23.5	0.1	0.7	18.8	92.3
L123	NK1-E-A19	22.2	1.6	4.1	9.3	20.1	0.2	17.3	0.1	0.9	13.9	89.7
L124	NK1-E-A20	23.1	2.0	3.6	8.5	21.2	0.2	16.4	0.2	1.0	13.1	89.3
L125	NK1-B-A1	18.8	1.6	3.2	7.4	17.9	0.2	22.2	0.2	0.9	17.8	90.1
L126	NK1-B-A2	19.2	0.7	2.9	7.0	17.2	0.1	23.6	0.1	0.8	18.9	90.6
L127	NK1-B-A3	16.4	1.0	3.0	7.1	18.0	0.2	26.7	0.1	0.7	21.4	94.5
L128	NK1-B-A4	19.9	0.9	3.6	8.4	20.0	0.2	20.0	0.2	0.8	16.0	90.0
L129	NK1-B-A5	21.2	1.4	3.7	8.4	20.3	0.2	18.9	0.2	1.0	15.1	90.3
L130	NK1-B-A6	19.9	1.2	3.7	7.1	17.6	0.2	22.7	0.2	1.3	18.1	91.9
L131	NK1-B-A7	22.7	1.0	3.4	7.6	20.7	0.2	18.1	0.3	0.6	14.5	88.9
L132	NK1-B-A8	18.9	1.3	3.5	8.0	18.1	0.2	21.5	0.1	1.1	17.2	89.8

Spot	Sample	SiO_2	TiO_2	Al_2O_3	FeO	MgO	MnO	CaO	Na_2O	K_2O	CO_2	Total
L133	NK1-B-A9	21.7	1.1	3.7	7.5	21.0	0.2	19.1	0.1	1.0	15.3	90.8
L134	NK1-B-A10	26.3	1.3	3.3	8.8	23.9	0.2	14.9	0.1	0.8	11.9	91.4
L135	NK1-B-A11	16.5	0.5	2.4	6.5	15.8	0.2	23.9	0.1	0.6	19.2	85.7
L136	NK1-B-A12	18.5	1.9	2.8	7.7	16.4	0.2	23.0	0.1	0.9	18.4	90.0
L137	NK1-B-A13	16.0	0.6	2.2	5.8	15.4	0.3	31.7	0.1	0.4	25.4	97.9
L138	NK1-B-A14	20.1	0.9	3.4	7.9	18.2	0.1	21.1	0.1	0.9	16.9	89.7
L139	NK1-B-A15	26.3	1.3	7.8	11.0	22.6	0.2	7.1	0.2	3.1	5.7	85.2
L140	NK1-B-A16	19.8	1.2	3.9	8.0	18.2	0.2	20.2	0.3	1.1	16.2	89.0
L141	NK1-B-A17	20.8	0.7	3.3	8.3	18.6	0.2	20.9	0.1	0.9	16.7	90.3
L142	NK1-B-A18	15.5	1.2	3.4	6.9	17.3	0.2	26.5	0.1	0.7	21.2	93.0
L143	NK1-B-A19	17.6	0.6	3.3	6.6	17.7	0.1	24.7	0.1	1.0	19.7	91.4
L144	NK1-B-A20	21.3	1.4	3.7	8.2	19.1	0.2	19.3	0.1	0.9	15.4	89.5
L198	NK1-D-A1	23.6	2.1	3.4	8.4	22.0	0.2	15.5	0.1	0.9	12.4	88.5
L199	NK1-D-A2	27.8	1.2	3.6	8.2	25.3	0.2	9.0	0.1	0.7	7.2	83.4
L200	NK1-D-A3	24.2	4.7	3.7	10.6	23.1	0.2	13.4	0.1	0.9	10.7	91.3
L201	NK1-D-A4	24.4	0.9	3.2	8.1	22.9	0.2	15.0	0.1	0.7	12.0	87.5
L202	NK1-D-A5	21.3	0.5	3.2	7.3	20.3	0.2	20.1	0.1	0.7	16.1	89.7
L203	NK1-D-A6	23.0	0.8	3.6	9.5	20.7	0.1	17.6	0.1	0.4	14.1	89.9
L204	NK1-D-A7	24.2	0.8	3.5	9.5	23.1	0.2	14.2	0.1	0.6	11.4	87.4
L205	NK1-D-A8	20.6	0.8	3.7	10.7	19.2	0.2	18.9	0.1	0.5	15.1	89.9
L206	NK1-D-A9	20.6	2.6	3.6	8.8	19.8	0.2	18.4	0.1	0.9	14.7	89.7
L207	NK1-D-A10	21.0	0.7	3.7	8.4	19.7	0.1	18.3	0.1	0.6	14.7	87.3
L208	NK1-D-B1	19.0	1.4	3.4	7.4	19.6	0.2	22.1	0.1	0.7	17.7	91.6
L209	NK1-D-B2	22.3	0.4	2.7	6.6	18.4	0.2	21.5	0.1	0.6	17.2	89.9
L210	NK1-D-B3	10.4	0.2	1.6	3.9	16.2	0.3	30.9	0.0	0.3	24.7	88.5
L211	NK1-D-B4	19.3	1.7	3.5	8.0	18.5	0.2	21.1	0.1	0.7	16.9	89.9
L212	NK1-D-B5	22.9	0.8	3.3	8.2	20.3	0.2	17.4	0.2	0.9	13.9	88.0
L213	NK1-D-B6	26.5	0.7	3.8	8.9	22.9	0.1	13.3	0.1	1.0	10.6	87.9
L214	NK1-D-B7	27.5	2.9	2.8	8.6	25.5	0.2	9.2	0.1	0.9	7.4	85.0
L215	NK1-D-B8	21.9	0.7	3.0	7.1	19.2	0.2	20.3	0.1	1.0	16.3	89.8
L216	NK1-D-B9	22.3	1.1	3.3	7.5	21.9	0.2	18.1	0.1	0.9	14.4	89.9
L217	NK1-D-B10	23.1	1.0	3.7	8.3	20.6	0.2	19.0	0.1	0.9	15.2	92.1
L218	NK1-D-C1	26.1	0.8	2.0	5.6	26.0	0.1	13.1	0.0	0.5	10.5	84.9
L219	NK1-D-C2	31.4	1.2	2.9	7.4	28.2	0.1	5.8	0.1	0.9	4.6	82.5

Spot	Sample	SiO_2	TiO_2	Al_2O_3	FeO	MgO	MnO	CaO	Na_2O	K_2O	CO_2	Total
L220	NK1-D-C3	30.7	0.8	2.3	6.7	28.4	0.1	7.3	-	0.5	5.8	82.5
L221	NK1-D-C4	30.0	2.1	2.6	8.3	27.0	0.2	6.8	0.1	0.7	5.4	83.1
L222	NK1-D-C5	24.4	3.8	2.8	8.0	22.6	0.3	13.2	0.1	0.8	10.6	86.5
Renard												
L19	67A-A1	30.4	1.6	5.1	10.2	28.3	0.1	3.5	0.0	0.6	2.8	82.6
L20	67A-A2	31.5	1.7	5.1	9.8	29.5	0.1	2.0	0.1	0.6	1.6	81.9
L21	67A-A3	30.4	1.1	5.7	9.2	27.4	0.1	5.8	0.1	1.4	4.7	85.9
L22	67A-A4	29.5	1.8	5.2	9.3	26.7	0.1	5.3	0.1	1.2	4.2	83.4
L23	67A-A5	30.6	1.3	5.6	9.8	28.3	0.1	4.0	0.1	1.1	3.2	84.2
L24	67A-A6	29.5	1.3	5.1	9.0	27.5	0.1	6.4	0.1	1.1	5.1	85.3
L25	67A-A7	31.5	1.3	4.6	8.7	29.3	0.1	3.8	0.0	0.7	3.1	83.0
L26	67A-A8	29.1	2.4	3.9	8.0	28.1	0.1	5.9	0.1	0.6	4.8	82.9
L153	067A-A1	23.0	1.4	5.4	8.2	21.7	0.1	15.6	0.1	2.5	12.5	90.5
L154	067A-A2	25.6	1.4	4.1	8.1	24.6	0.1	13.8	0.1	1.2	11.0	90.0
L155	067A-A3	24.9	1.4	4.0	8.6	22.1	0.2	14.1	0.1	1.6	11.3	88.2
L156	067A-A4	28.0	1.4	4.7	9.4	23.8	0.2	11.1	0.1	1.7	8.9	89.2
L158	067A-A5	24.7	2.1	5.1	9.9	22.7	0.2	14.1	0.1	2.1	11.3	92.2
L159	067A-A6	28.6	1.5	5.4	10.9	25.6	0.2	6.2	0.1	2.0	5.0	85.5
L160	067A-A7	27.1	1.1	4.6	9.0	23.9	0.1	11.0	0.1	1.6	8.8	87.2
L161	067A-A8	27.8	1.5	4.9	8.2	24.4	0.1	9.7	0.1	1.2	7.8	85.6
L162	067A-A9	28.4	2.3	4.2	6.0	28.1	0.1	8.2	0.1	0.2	6.6	84.1
L157	067A-A10	10.2	0.1	0.6	1.5	11.4	0.1	41.0	0.0	0.3	32.8	97.8
L163	067A-B1	17.7	0.4	0.9	2.4	17.1	0.0	32.5	0.0	0.0	26.0	96.9
L164	067A-B2	29.2	1.1	4.8	9.3	27.7	0.1	6.6	0.1	1.2	5.3	85.4
L165	067A-B3	31.3	1.6	6.1	11.0	27.2	0.1	4.7	0.1	1.8	3.8	87.7
L166	067A-B4	27.3	1.7	4.3	13.4	28.6	0.2	7.6	0.1	0.9	6.1	90.1
L167	067A-B5	30.3	1.7	6.0	10.6	26.6	0.1	6.2	0.1	1.8	5.0	88.3
L168	067A-B6	25.1	1.0	2.9	4.6	23.9	0.0	16.7	0.0	0.4	13.4	87.9
L169	067A-B7	24.8	0.7	3.2	5.6	26.7	0.1	14.8	0.0	0.3	11.8	88.0
L170	067A-B8	31.5	3.1	5.6	8.8	26.5	0.1	7.9	0.1	1.9	6.3	91.8
L171	067A-B9	33.2	0.7	3.4	5.0	29.8	0.1	7.5	0.1	0.4	6.0	86.2
L172	067A-B10	34.3	0.2	1.2	4.9	31.6	0.0	0.9	0.0	0.1	0.7	73.9

Spot	**Sample**	**SiO_2**	**TiO_2**	**Al_2O_3**	**FeO**	**MgO**	**MnO**	**CaO**	**Na_2O**	**K_2O**	**CO_2**	**Total**
Averages												
	42B-A	32.1	1.4	4.3	7.2	24.5	0.2	8.8	0.2	1.8	7.0	87.5
	42B-B	34.5	1.6	4.4	9.0	27.5	0.2	3.6	0.1	1.0	2.9	84.8
	37-A	28.2	1.6	3.6	8.8	21.4	0.1	14.2	0.1	1.1	11.4	90.6
	36-A	25.6	1.1	3.8	7.4	19.1	0.2	17.6	0.1	1.5	14.1	90.4
	36-B	28.0	1.4	3.7	9.0	20.0	0.2	13.8	0.1	1.4	11.1	88.8
	36-C	31.4	1.5	3.9	8.9	22.6	0.2	10.3	0.2	1.6	8.2	88.7
	NK1-A-A	22.2	2.5	3.6	9.7	22.2	0.2	15.4	0.1	0.6	12.3	88.9
	NK1-A-B	24.1	1.9	2.6	7.9	23.5	0.2	15.3	0.1	0.5	12.2	88.1
	NK1-A-C	19.1	1.3	2.8	6.7	19.2	0.2	22.5	0.1	0.7	18.0	90.6
	NK1-E-A	21.6	1.6	3.4	8.5	20.3	0.2	18.1	0.1	0.8	14.5	89.1
	NK1-B-A	19.9	1.1	3.5	7.7	18.7	0.2	21.3	0.1	1.0	17.0	90.5
	NK1-D-A	23.1	1.5	3.5	8.9	21.6	0.2	16.0	0.1	0.7	12.8	88.4
	NK1-D-B	21.5	1.1	3.1	7.4	20.3	0.2	19.3	0.1	0.8	15.4	89.3
	NK1-D-C	28.5	1.7	2.5	7.2	26.4	0.1	9.2	0.1	0.7	7.4	83.9
	67A-A	30.3	1.6	5.0	9.2	28.1	0.1	4.6	0.1	0.9	3.7	83.7
	067A-A	24.8	1.4	4.3	8.0	22.8	0.1	14.5	0.1	1.4	11.6	89.0
	067A-B	28.5	1.2	3.8	7.5	26.5	0.1	10.5	0.1	0.9	8.4	87.6

Table 2: XRF and average EMP analyses of pelleral lapilli

Spot	Sample	SiO_2	TiO_2	Al_2O_3	FeO	MgO	MnO	CaO	Na_2O	K_2O	CO_2	Total
Buffalo Head Hills												
K6-2*	BHH^1	28.5	1.4	4.2	8.9	22.6	0.2	13.8	0.7	1.4	10.2	91.8
K6-3*	BHH^2	30.9	1.5	4.5	9.7	21.9	0.2	10.2	0.8	1.4	7.2	88.2
K6-5*	BHH^3	31.5	1.5	3.9	9.5	22.2	0.2	9.4	0.7	1.3	6.5	86.6
K6-6*	BHH^4	26.5	1.7	4.6	9.2	19.1	0.2	16.6	1.0	1.7	10.7	91.2
L234	36-B^1	28.0	1.4	3.7	9.0	20.0	0.2	13.8	0.1	1.4	11.1	88.7
L235	36-C^2	31.4	1.6	3.9	8.9	22.6	0.2	10.3	0.2	1.6	8.2	88.7
L228	42B-A^3	32.1	1.4	4.3	7.2	24.5	0.2	8.8	0.2	1.8	7.0	87.5
L233	36-A^4	25.6	1.1	3.9	7.4	19.1	0.2	17.6	0.1	1.5	14.1	90.4
L229	42B-B	34.5	1.6	4.4	9.0	27.5	0.2	3.6	0.1	1.0	2.9	84.8
L231	37-A	28.2	1.6	3.6	8.8	21.4	0.1	14.2	0.1	1.1	11.4	90.6
Nikos												
NK1-F*	Nikos^1	24.9	2.7	3.1	8.9	24.4	0.3	14.8	0.1	0.6	9.6	89.4
NK1-D*	Nikos^2	25.6	2.5	2.9	9.1	25.1	0.2	13.5	0.1	0.5	9.3	88.9
L236	NK1-A-A^1	22.2	2.6	3.6	9.7	22.2	0.2	15.4	0.1	0.6	12.3	88.9
L237	NK1-A-B^2	24.1	1.9	2.6	7.9	23.5	0.2	15.3	0.1	0.5	12.2	88.1
L238	NK1-A-C	19.1	1.3	2.8	6.7	19.2	0.2	22.5	0.1	0.7	18.0	90.6
L239	NK1-E-A	21.6	1.6	3.4	8.5	20.3	0.2	18.1	0.1	0.8	14.5	89.1
L240	NK1-B-A	19.9	1.1	3.5	7.7	18.7	0.2	21.3	0.1	1.0	17.0	90.5
L248	NK1-D-A	23.1	1.5	3.5	8.9	21.6	0.2	16.1	0.1	0.7	12.8	88.4
L249	NK1-D-B	21.5	1.1	3.1	7.4	20.3	0.2	19.3	0.1	0.8	15.4	89.3
L250	NK1-D-C	28.5	1.7	2.5	7.2	26.4	0.1	9.2	0.1	0.7	7.4	83.9
Renard												
11659A*	Renard^1	23.6	3.5	4.9	9.0	25.1	0.1	11.2	0.2	0.7	12.2	90.4
L243	067A-A^1	24.8	1.4	4.3	8.0	22.8	0.1	14.5	0.1	1.4	11.6	89.0
L244	067A-B	28.5	1.2	3.8	7.5	26.5	0.1	10.5	0.1	0.9	8.4	87.6
L225	67A-A	30.3	1.6	5.0	9.2	28.1	0.1	4.6	0.1	0.9	3.7	83.7

* indicates XRF analyses

^{1} superscripts indicate matching XRF to EMP analyses

Table 3: Intersection compositions and estimated magma compositions

	SiO_2	TiO_2	Al_2O_3	FeO	MgO	MnO	CaO	Na_2O	K_2O	CO_2	Total
Cratonic Mantle											
BHH[1]	44.1	0.03	0.8	7.8	46.7	0.1	0.6	0.02	0.01	0.0	100.2
NIK[2]	43.0	0.03	1.2	7.4	46.0	0.1	0.7	0.04	0.03	0.0	98.6
REN[2]	43.0	0.03	1.2	7.4	46.0	0.1	0.7	0.04	0.03	0.0	98.6
Intersection Compositions*											
Buffalo Head Hills	15.0				15.0		25.0			25.0	80.0
Nikos	10.0				15.0		30.0			30.0	85.0
Renard	20.0				30.0		20.0			20.0	90.0
Estimated Magma Compositions**											
Buffalo Head Hills	15.2	2.3	6.0	11.0	14.7	0.3	26.2	0.0	0.5	22.7	98.8
Nikos[3]	9.1	3.1	2.4	7.0	8.9	0.2	32.0	0.2	1.5	34.5	99.0
Renard	21.6	3.3	3.5	9.0	19.5	0.1	22.3	0.2	2.1	18.4	100.0

** estimated from binary plots (cation units)*

*** estimated magma compositions via the xenocrystic mantle extraction method*

[1] Aulbach et al., 2004

[2] Schmidberger and Francis, 1999

[3] Patterson et al., 2009

CHAPTER 4

Kimberlite eruptions as triggers for early Cenozoic hyperthermals

Chapter 2 and 3 establish the composition of kimberlite magma as being silico-carbonatite magmas and as such, have very high CO_2 contents, up to 35 wt%. However, kimberlite rocks rarely have bulk composition with CO_2 contents greater than 20 wt% and furthermore, volcano-clastic kimberlite rocks have less than 5 wt% CO_2. The major propellant of kimberlite eruption is thought to be exsolution of volatiles by the magma, mainly CO_2, during the ascent to the surface. Chapter 4 investigates the effect of kimberlite CO_2 degassing on the Earth's climate.

Abstract

The early Cenozoic experienced at least three short but major hyperthermals associated with disruptions of the global carbon cycle. The largest among those, the Paleocene-Eocene thermal maximum, was associated with a negative carbon isotopic excursion of ~ 2.5‰ that appears to be best explained by the thermal dissociation of methane hydrates due to an initial period of warming. The cause of the initial warming has been attributed to a massive injection of carbon (CO_2 and/or CH_4) into the atmosphere, however, the source of the carbon is as yet unknown. The emplacement of a large cluster of kimberlite pipes at ~56 Ma in the Lac de Gras region of northern Canada may have provided the carbon that triggered early warming in the form of exsolved magmatic CO_2. Our calculations indicate that the estimated 900-1,100 Pg of carbon required for the initial ~3 °C of ocean water warming associated with the Paleocene-Eocene thermal maximum could have been released during the emplacement of a large kimberlite cluster. The coeval ages of two other kimberlite clusters in the Lac de Gras field and two other early Cenozoic hyperthermals indicate that CO_2 degassing during kimberlite emplacement is a plausible source of the CO_2 responsible for these sudden global warming events.

Introduction

The Paleocene-Eocene thermal maximum (PETM) is an early Cenozoic hyperthermal that is recorded both on land and in the ocean. It is associated with a global disturbance in carbon isotopes and a global dissolution of $CaCO_3$ sediments. On the basis of these and other environmental changes, the PETM has been related to an enormous release of CO_2 and/or CH_4

[*Dickens et al.*, 1997]. Although the sequence of the events during the PETM are difficult to piece together, the available evidence indicates early warming, followed by a more drastic warming coincident with a negative shift in $\delta^{13}C$ [*Carozza et al.*, 2011; *Leon-Rodriguez and Dickens*, 2010; *Secord et al.*, 2010; *Sluijs et al.*, 2007; *D J Thomas et al.*, 2002]. Although the negative carbon isotopic excursion (CIE) associated with the PETM has been attributed to carbon released from methane hydrates on the sea floor, the source of carbon that produced the early warming that destabilized these hydrates is yet unknown [*Bowen et al.*, 2004; *Bralower et al.*, 1997; *Carozza et al.*, 2011; *Dickens*, 2000; *Dickens et al.*, 1997; *Dickens et al.*, 1995; *Hancock and Dickens*, 2005; *Kent*, 2003; *Lourens et al.*, 2005; *Moore and Kurtz*, 2008; *Panchuk et al.*, 2008; *Sluijs et al.*, 2007; *D J Thomas et al.*, 2002; *Ellen Thomas*, 2003; *E. Thomas and Shackleton*, 1996; *E. Thomas and Zachos*, 2000; *Tripati and Elderfield*, 2005; *J. C. Zachos*, 2003; 2004; *James C. Zachos et al.*, 1993; *J. C. Zachos et al.*, 2001; *James C Zachos et al.*, 2007; *J. C. Zachos et al.*, 2005; *Zeebe et al.*, 2009]. In this paper, we propose that the initial warming that occurred during the early stages of the PETM (and two other early Cenozoic hyperthermals) was caused by the release of CO_2 during the eruption of a large cluster of kimberlite pipes in the Lac de Gras kimberlite field of the Slave Province, Canada.

Background

Several proposals have been offered to explain the PETM including; comet impact [*Kent*, 2003], global wild fires [*Kurtz et al.*, 2003], volcanic activity [*Svensen*, 2004], and methane hydrate dissociation [*Dickens et al.*, 1997]. The lack of extra-terrestrial tracer material in CIE deposits, such as iridium anomalies, and the discovery that magnetotactic bacteria is the cause of magnetically anomalous clay layers renders the impact hypothesis unlikely [*Kopp et al.*, 2007]. The relative absence of anomalous graphitic black carbon in the PETM sediments argues against the possibility that global wildfires were the cause of the PETM [*Moore and Kurtz*, 2008]. Typical basaltic volcanic activity is also an unlikely source of this initial CO_2 because of the low CO_2 contents of basalts (< 1 wt %) associated with large igneous provinces (LIP) and their slow eruption rates [*Blundy et al.*, 2010; *Caldeira and Rampino*, 1991; *Gerlach et al.*, 2002; *Keeling et al.*, 1995; *Sobolev et al.*, 2011]. Furthermore, volcanic SO_2 released during LIP eruptions forms considerable amounts of atmospheric sulfate aerosols, which would cause global cooling [*Self et al.*, 2006]. The release of thermogenic methane produced by igneous intrusions into organic rich sediments would require that the CIE precedes the ocean water warming event, contrary to the observed isotopic data. Although methane from hydrate dissociation is thought to have played a pivotal role during the PETM, because it is highly depleted in ^{13}C and a strong greenhouse gas, its role is most consistent with having caused the CIE and not the initial warming.

The negative shift of $\delta^{13}C$ (CIE) during the PETM is thought to be related to a geologically rapid (<10 kyr) carbon release that was significantly depleted in ^{13}C [*Rohl et al.*, 2000; *James C Zachos et al.*, 2007]. Prior to the light carbon injection, a brief period of oceanic [*Sluijs et al.*, 2007; *D J Thomas et al.*, 2002] and continental [*Secord et al.*, 2010] warming, as well as dissolution of seafloor carbonates [*Leon-Rodriguez and Dickens*, 2010], is thought to have occurred, indicating that the carbon input that caused the CIE is unlikely to have produced the initial warming. Recent models of carbon emissions during the PETM indicate that it is characterized by an initial period of warming and carbonate dissolution requiring ~1000 Pg of carbon, which is then followed by a rapid input of depleted carbon that caused the CIE [*Carozza et al.*, 2011]. There are few carbon reservoirs available that could contribute to the early warming, without resulting in large $\delta^{13}C$ excursions, because organic matter and methane hydrates are strongly depleted in ^{13}C.

Observations

The Earth's mantle is a vast reservoir of carbon, likely equivalent to all other carbon reservoirs combined. Normally, mantle carbon leaks out slowly through mid ocean ridges and volcanoes, at rates of 10-3 Pg/yr of carbon [*Caldeira and Rampino*, 1991], three orders of magnitude lower than that required for hyperthermals (~1 Pg/yr; [*Zeebe et al.*, 2009]). However in rare circumstances, direct conduits between the deep mantle and the atmosphere are provided by rapid explosive kimberlite eruptions. In contrast, the CO_2 contents of basaltic magmas in large volcanic provinces (i.e. shield volcanoes or flood basalts) are estimated to be << 1 wt% [*Blundy et al.*, 2010; *Gerlach et al.*, 2002; *Keeling et al.*, 1995; *Sobolev et al.*, 2011] and although large volcanic provinces provide vast amounts of lava (10^5 - 10^6 km^3), thus vast amounts of CO_2, they are emplaced over time scales of millions of years [*Wignall*, 2001]. Kimberlite fields are found on every continent and throughout at least the last one billion years of the geological record and their emplacement is distinct in that they occur in discrete fields and during distinct episodes (Figure 4- 1).

Magmatic kimberlite rocks have very high carbonate contents (CO_2 ~20 wt %; [*Brooker et al.*, 2001; *Francis and Patterson*, 2009; *Nielsen and Jensen*, 2005; *Patterson et al.*, 2009; *Sparks et al.*, 2006], yet volcanoclastic kimberlite rocks are relatively carbonate-poor ($CO_2 < 5$ wt %) and characterized by the final crystallization of monticellite, phlogopite, and diopside at the expense of the typical carbonate-rich matrix that characterizes magmatic kimberlite [*Skinner and Marsh*, 2004; *Sparks et al.*, 2006]. That is as CO_2 degasses from the ascending magma, the $a\mathrm{SiO}_2$ of the melt increased to levels which favor crystallization of silicate minerals (i.e. monticellite, phlogopite and diopside) in the simple $CaO–MgO–SiO_2–CO_2$ system [*Canil and Bellis*, 2008; *Franz and Wyllie*, 1967; *Ootto and Wyllie*, 1993]. Thus, the transition from magmatic kimberlite to volcanoclastic kimberlite is associated with the release of CO_2. Kimberlite magma is estimated to rise to the surface in a matter of hours and have eruptions durations on the order of weeks, thus significant amounts of CO_2 can be released at high rates.

The ages of the three early Cenozoic hyperthermals (~59.2, 55.5 and 53.2; [*Charles et al.*, 2011; *Hancock and Dickens*, 2005; *Lourens et al.*, 2005; *E. Thomas and Zachos*, 2000]) are indistinguishable from three of the four ages of kimberlite clusters that comprise the Lac de Gras kimberlite field of Northern Canada. There are over 270 kimberlites in the Lac de Gras kimberlite field that range in age from 74 Ma to 45 Ma, with at least four distinct age and spatial clusters: 59.0±0.7 Ma, 55.5±0.7 Ma, 53.2±0.3 Ma, and 47.8±0.3 Ma [*Creaser et al.*, 2004; *Graham et al.*, 1999]. Reversals in magnetic polarity in the Lac de Gras kimberlites [*Cande and Kent*, 1995] provide substantially better temporal resolution than that obtained by radiometric dating [*Lockhart et al.*, 2004]. Seismic data indicate that the three younger kimberlite clusters appear to have been emplaced along distinct corridors that represent deep crustal or lithospheric dyke swarms composed of numerous dykes clustered within zones kilometres in width [*Snyder and Lockhart*, 2005]. Although only 50 of the over 270 Lac de Gas kimberlite pipes have precise ages [*Creaser et al.*, 2004; *Graham et al.*, 1999; *Heaman et al.*, 2003], their age data exhibits a clustered distribution (59.0±0.7 Ma, 55.5±0.7 Ma, 53.2±0.3 Ma, and 47.8±0.3 Ma).

Although the ages of the clusters within the Lac de Gras kimberlite field and those of the early Cenozoic hyperthermals have been previously reported, their striking correspondence is first demonstrated here (Figure 4- 2). The lack of age dates for most of the kimberlite pipes in the Lac de Gras field requires a reconstruction of an age distribution for the undated kimberlite pipes to estimate the total number of pipes within each cluster. We have approached this reconstruction by assuming that the unknown age data will have a similar, albeit smooth, distribution as the 50 known ages. Considering that three of the age clusters (55.5±0.7 Ma, 53.2±0.3 Ma, and 47.8±0.3 Ma) have been shown to be spatially clustered [i.e Figure 4- 3 in *Lockhart et al., 2004*], 29 additional undated kimberlites pipes that lie within these intrusive corridors were assigned the mean age for their respective clusters (55.5 = 19; 53.2 = 10). Although, age clusters have been demonstrated in the Lac de Gras kimberlite field, it may be reasonable to assume that the remaining kimberlites of unknown age are similarly clustered, we have chosen a simpler distribution approach (Figure 4- 3). The remaining kimberlites are distributed across 45-75 Ma with a similar distribution as the dated kimberlite which have a median age of 55.9. The three methods are then stacked in a histogram resulting with a prominent mode at 55.9 Ma. The modes corresponding to four kimberlite clusters are at 59.0 Ma (n= 12), 55.9 Ma (n= 50), 53.2 Ma (n= 33), and 47.8 Ma (n= 7). The three older kimberlite age clusters correspond within error to three early Cenozoic hyperthermals, one of which is the PETM at 55.5 Ma.

Volume Estimates

Kimberlite pipes in the Lac de Gras field have a cone morphology similar to that of the classic South African model [*Field and Scott Smith*, 1997], however, they tend to be shallow (~950 m; [*Moss et al.*, 2008; *Nowicki et al.*, 2008], thus they are volumetrically smaller. Phanerozoic strata are missing in the Lac de Gras area, although crustal xenoliths preserved within the kimberlite deposits suggest an original succession of Cretaceous marine shales, terrigenous arenite, and organic peat capping basement rocks during the Early Cenozoic, with variable estimates of thickness ranging from 100 m to 300 m [*Nowicki et al.*, 2004; *Pell*, 1997; *L D Stasiuk et al.*, 1999; *Sweet*, 2003]. Detailed studies of kimberlite pipes in the Lac de Gras area indicate that their present depths vary between 400-1,100 m [*Moss et al.*, 2008; *Nowicki et al.*, 2008], and thus emplacement depths of ~600-1,300 m. Pipe morphology is characterized by steeply dipping walls (~80°; [*Nowicki et al.*, 2008]), yielding an average volume of 3×10^7 m^3 of kimberlite per pipe. Although kimberlite pipes often deviate from a simplified cone shaped body [*Nowicki et al.*, 2004], such deviations tend to increase volume and thus the foregoing would be a minimum volume estimate. Furthermore, kimberlite pipes are typically excavated multiple times (3-5) by repeated eruption episodes [*Scott Smith*, 2008] and thus the volume of the erupted kimberlite is likely many times that of the observed pipes. The Lac de Gras kimberlite cluster that is coeval with the PETM comprises ~50 known pipes corresponding to a minimum volume of erupted magma of 5-8 x 10^9 m3.

The capacity of kimberlite magma to transport CO_2 is difficult to constrain because a gaseous CO_2 phase is likely to develop as the magma undergoes depressurization during ascent [*Russell et al.*, 2012; *Sparks et al.*, 2006]. Russell et al. [2012] demonstrates that the chemical assimilation of orthopyroxene by proto kimberlite magma (carbonatite) would release large amounts of CO_2 due to the decreasing solubility of CO_2 in a melt as the $a$$SiO_2$ increases, thus it is likely that an additional 25-30 wt% of free CO_2 gas accompanies kimberlite eruptions. The presence of this free gas phase was first demonstrated as a requirement for kimberlite dyke initiation and propagation to explain the ultra-rapid ascent of kimberlite from such great depths [*Wilson and Head III*, 2007]. Despite the foregoing, the volume of a free CO_2 gas phase is difficult to quantify, however, a minimum constraint on CO_2 in magmatic kimberlite is simply estimated by the stoichiometry of carbonate and the carbonate content of magmatic kimberlite, ~20% of CO_2 by weight [*Brooker et al.*, 2001; *Nielsen and Sand*, 2008; *Patterson et al.*, 2009; *Sparks et al.*, 2006]. The density of magmatic kimberlite is ~3.2 x 10^6 g/m^3 (80% Fo_{90} and 20% calcite), thus a volume of 5-8 x 10^9 m^3 yields 2-3 x 10^{16} g of kimberlite. Kimberlite pipes, however, are dominated by volcanoclastic kimberlite rocks, which form through explosive degassing that occurs during kimberlite pipe excavation and thus are CO_2 poor compared to magmatic kimberlite, typically <5% of CO_2 by weight. Calculating the mass of CO_2 degassed during emplacement as a 15% net weight loss, results in 2-4 x 10^{15} g of CO_2 or 6.0-10.0 x 10^{14} g of carbon per kimberlite cluster, using the observed pipe volume. Studies regarding kimberlite eruption dynamics suggest the range of magma supply rates is 500-10,000

m^3/s [*Sparks et al.*, 2006], thus a kimberlite cluster of 55 pipes would degas the above mass of carbon between 5 and 200 days. The eruption of a single kimberlite cluster eruption could release carbon at a rate of ~2-40 Pg/yr. As stated earlier, kimberlite pipes are typically excavated by repeated eruption episodes [*Scott Smith*, 2008], and erupt larger volumes of magma than what remains in the pipes, thus the calculated duration required to produce 1000 Pg of carbon is estimated to be 200-3,000 days (Figure 4- 4).

Discussion

Our calculations suggest that kimberlite eruptions release carbon at a rate that far exceeds 1 Pg/yr. Estimates of minimum kimberlite eruption volumes that range from 10^6 to 10^8 m^3 based on observable pipe volumes suggest durations of days to weeks dependant on the magma supply rate (500-10,000 m^3/s: [*Sparks et al.*, 2006]). These durations are, however, likely to be much shorter than the total duration of the eruptions; 1) the volume estimates are the lower bounds because they do not include the amount of magma ejected out of the kimberlite pipe, 2) driving pressure in the source region may decline as an eruption proceeds, thus leading to an exponential decrease of magma supply rate which results in lower estimated supply rates [*Sparks et al.*, 2006; *M V Stasiuk et al.*, 1993]. The inferred flow rate (500-10,000 m3/s) approach those typical of Plinian eruption columns that reach 10 to 35 km into the stratosphere [*Sparks et al.*, 1997; *Sparks et al.*, 2006]. The volume of kimberlite trapped in the pipe is only a small fraction of the total erupted magma and thus the eruptions are likely to be on the order of weeks to months in duration. Calculating the eruption duration if the magma supply rate is increased to 5,000 m^3/s, the duration required to produce 900-1,100 Pg of carbon is reduced to 300-200 days (Figure 4- 4). Furthermore, even these durations are considered longer than required due to the almost certain presence of a gaseous CO_2 phase that develops during magma ascent.

In addition to the much studied PETM, there are two other hyperthermals with dissolution horizons observed during the late Paleocene to mid Eocene period that are similar to that associated with the PETM (~55.6 Ma); during the mid-Paleocene at ~59.1 Ma [*Hancock and Dickens*, 2005] and the early-Eocene at ~53.2 Ma [*Lourens et al.*, 2005]. These horizons are similar to the horizon associated with the PETM and are characterized by the presence of a distinct reddish clay layer, an abrupt drop in carbonate content, and a pronounced peak in magnetic susceptibility that is thought to reflect increased clay content [*Bernaola et al.*, 2007]. These two dissolution horizons are characterized by decreased oxygen isotope ($\delta^{18}O$) and carbon isotope ($\delta^{13}C$) values similar to the anomalies associated with the PETM, although of smaller magnitudes [*Hancock and Dickens*, 2005; *Lourens et al.*, 2005]. The similarities between the three hyperthermals have led most workers to consider all three to be sedimentary responses to abrupt climatic change attributed to disruption of the carbon cycle.

The correspondence between the ages of three early Cenozoic hyperthermals and three kimberlite clusters in the Lac de Gras kimberlite field suggest that kimberlite eruption may have provided the CO_2 responsible for the initial global warming that destabilized marine methane hydrates. Although the analytical uncertainties associated with ages of the Lac de Gras kimberlites are relatively small (~1-2 Ma), it is difficult to discern whether individual kimberlites pipes in a cluster erupted concurrently or sporadically over longer time spans. The spatial trends of the clusters indicate that they belong to common dyke systems, which coupled with the high estimated ascent rates suggest that the magma of individual kimberlite clusters was delivered to the kimberlite pipes simultaneously. Furthermore, detailed facies studies of re-sedimented kimberlite in the A154 kimberlite pipe (coeval with the PETM) indicates that material from adjacent kimberlite pipes was deposited in the still open pipe [*Moss et al.*, 2008]. It is therefore likely that numerous kimberlite pipes composing a cluster erupt within relatively short time periods. Thus, our best estimates suggest that the eruption of a large kimberlite cluster is capable of delivering to the atmosphere the CO_2 required to produce the early initial warming associated with three early Cenozoic hyperthermals. We propose that the eruption of kimberlite cluster within the Lac de Gras kimberlite field produced the CO_2 responsible for the initial surface water warming associated with the early Cenozoic hyperthermals, that led to thermal dissociation of sea floor methane hydrates and the resultant CIE's.

Conclusions

The striking correspondence between the emplacement ages of three kimberlite clusters in the Lac de Gras field of the Slave Province and the three hyperthermals in the early Cenozoic suggests that they are genetically linked. Our calculations indicate that the eruption of three kimberlite clusters of the Lac de Gras field could have provided the CO_2 required for the initial warming of ocean water of the Paleocene-Eocene Thermal Maximum and two other early Cenozoic hyperthermals. As the global oceans buffered the increased atmospheric CO_2, ocean waters became increasingly acidified and produced the carbonate dissolution horizons. The transfer of warm surface ocean water to intermediate depths led to thermal dissociation of sea floor methane hydrates providing the isotopically depleted carbon that produced the carbon isotopic excursion. The rapid transfer of large amounts of CO_2 from the mantle to the atmosphere by kimberlite eruptions may thus provide a genetic link between mantle processes and enigmatic climatic events in the geologic record.

Acknowledgements

This paper arose out of discussions regarding paleo-climate with a number of colleagues at McGill University, mainly Al Mucci, Eric Galbraith, Dirk Schumann and David Carozza. In addition, the ideas in this paper have benefited from discussions with William Manarik and Boswell Wing as well as statistical advice from Vincent Van Hinsberg. We appreciate the rigorous and many reviews of our manuscript, the thoughtful and helpful comments from Dante Canil were greatly appreciated.

References

Bernaola, G., J. I. Baceta, X. Orue-Etxebarria, L. Alegret, M. Martin-Rubio, J. Arostegui, and J. Dinares-Turell (2007), Evidence of an abrupt environmental disruption during the mid-Paleocene biotic event (Zumaia section, western Pyrenees), *Geological Society of America Bulletin*, *119*(7-8), 785-795.

Blundy, J., K. V. Cashman, A. Rust, and F. Witham (2010), A case for CO_2-rich arc magmas, *Earth and Planetary Science Letters*, *290*(3-4), 289-301.

Bowen, G. J., D. J. Beerling, P. L. Koch, J. C. Zachos, and T. Quattlebaum (2004), A humid climate state during the Palaeocene/Eocene thermal maximum, *Nature*, *432*(7016), 495-256 499.

Bralower, T. J., D. J. Thomas, J. C. Zachos, M. M. Hirschmann, U. Rohl, H. Sigurdsson, E. Thomas, and D. L. Whitney (1997), High-resolution records of the late Paleocene thermal maximum and circum-Caribbean volcanism: Is there a causal link?, *Geology*, *25*(11), 963-966.

Brooker, R. A., S. C. Kohn, J. R. Holloway, and P. F. McMillan (2001), Structural controls on the solubility of CO_2 in silicate melts: Part I: bulk solubility data, *Chemical Geology*, *174*(1-3), 225-239.

Caldeira, K., and M. R. Rampino (1991), The Mid-Cretaceous Super Plume, carbon dioxide, and global warming, *Geophys. Res. Lett.*, *18*(6), 987-990.

Cande, S. C., and D. V. Kent (1995), Revised calibration of the geomagnetic polarity timescale for the Late Cretaceous and Cenozoic, *J. Geophys. Res.*, *100*(B4), 6093-6095.

Canil, D., and A. J. Bellis (2008), Phase equilibria in a volatile-free kimberlite at 0.1 MPa and the search for primary kimberlite magma, *Lithos*, *105*(1-2), 111-117.

Carozza, D. A., L. A. Mysak, and G. A. Schmidt (2011), Methane and environmental change during the Paleocene-Eocene thermal maximum (PETM): Modeling the PETM onset as a two-stage event, *Geophys. Res. Lett.*, *38*(5), L05702.

Charles, A. J., D. J. Condon, I. C. Harding, H. Pälike, J. E. A. Marshall, Y. Cui, L. Kump, and I. W. Croudace (2011), Constraints on the numerical age of the Paleocene-Eocene boundary, *Geochem. Geophys. Geosyst.*, *12*, Q0AA17.

Creaser, R. A., H. Grütter, J. Carlson, and B. Crawford (2004), Macrocrystal phlogopite Rb-Sr dates for the Ekati property kimberlites, Slave Province, Canada: evidence for multiple intrusive episodes in the Paleocene and Eocene, *Lithos*, *76*(1-4), 399-414.

Dickens, G. R. (2000), Methane oxidation during the Late Palaeocene Thermal Maximum, *Bull. Soc. Geol. Fr.*, *171*(1), 37-49.

Dickens, G. R., M. M. Castillo, and J. C. G. Walker (1997), A blast of gas in the latest Paleocene: Simulating first-order effects of massive dissociation of oceanic methane hydrate, *Geology*, *25*, 259-262.

Dickens, G. R., J. R. O'Neil, D. K. Rea, and R. M. Owen (1995), Dissociation of oceanic methane hydrate as a cause of the carbon isotope excursion at the end of the Paleocene, *Paleoceanography*, *10*, 965-971.

Faure, S. (2010), World Kimberlites CONSOREM Database (Version 3).

Field, M., and B. H. Scott Smith (1997), *Contrasting geology and near surface emplacement of kimberlite pipes in southern Africa and Canada*, Red Roof Design, Cape Town, South Africa.

Francis, D., and M. Patterson (2009), Kimberlites and aillikites as probes of the continental lithospheric mantle, *Lithos*, *109*(1–2), 72-80.

Franz, G. W., and P. J. Wyllie (1967), *Experimental studies in the system* $CaO–MgO–SiO_2–CO_2–H_2O$, Wiley and Sons, New York.

Gerlach, T. M., K. A. McGee, T. Elias, A. J. Sutton, and M. P. Doukas (2002), Carbon dioxide emission rate of Kilauea Volcano: Implications for primary magma and the summit reservoir, *J. Geophys. Res.*, *107*(B9), 2189.

Graham, I., J. L. Burgess, D. Bryan, P. J. Ravenscroft, E. Thomas, B. J. Doyle, R. Hopkings, and K. A. Armstrong (1999), Exploration history and geology of the Diavik kimberlites, Lac de Gras, Northwest Territories, Canada, *Seventh International Kimberlite Conference*, *1*, 262-279.

Hancock, H. J. L., and G. R. Dickens (2005), Carbonate dissolution episodes in Paleocene and Eocene sediment, Shatsky Rise, West-central Pacific, *Proceedings of the Ocean Drilling Program, Scientific Results*, *198*, 1-24.

Heaman, L. M., B. A. Kjarsgaard, and R. A. Creaser (2003), The timing of kimberlite magmatism in North America: implications for global kimberlite genesis and diamond exploration, *Lithos*, *71*(2-4), 153-184.

Keeling, C. D., T. P. Whorf, M. Wahlen, and J. van der Plichtt (1995), Interannual extremes in the rate of rise of atmospheric carbon dioxide since 1980, *Nature*, *375*(6533), 666-670.

Kent, D. V. (2003), A case for a comet impact trigger for the Paleocene/Eocene thermal maximum and carbon isotope excursion, *Earth Planet. Sci. Lett.*, *211*, 13-26.

Kopp, R. E., T. D. Raub, D. Schumann, H. Vali, A. V. Smirnov, and J. L. Kirschvink (2007), Magnetofossil spike during the Paleocene-Eocene thermal maximum: Ferromagnetic resonance, rock magnetic, and electron microscopy evidence from Ancora, New Jersey, United States, *Paleoceanography*, *22*(4), PA4103.

Kurtz, A. C., L. R. Kump, M. A. Arthur, J. C. Zachos, and A. Paytan (2003), Early Cenozoic decoupling of the global carbon and sulfur cycles, *Paleoceanography*, *18*(4), 1090.

Leon-Rodriguez, L., and G. R. Dickens (2010), Constraints on ocean acidification associated with rapid and massive carbon injections: The early Paleogene record at ocean drilling program site 1215, equatorial Pacific Ocean, *Palaeogeography, Palaeoclimatology, Palaeoecology*, *298*(3-4), 409-420.

Lockhart, G., H. Grütter, and J. Carlson (2004), Temporal, geomagnetic and related attributes of kimberlite magmatism at Ekati, Northwest Territories, Canada, *Lithos*, *77*(1-4), 665-682.

Lourens, L. J., A. Sluijs, D. Kroon, J. C. Zachos, E. Thomas, U. Rohl, J. Bowles, and I. Raffi (2005), Astronomical pacing of late Palaeocene to early Eocene global warming events, *Nature*, *435*(7045), 1083-1087.

McInerney, F. A., and S. L. Wing (2011), The Paleocene-Eocene Thermal Maximum: A Perturbation of Carbon Cycle, Climate, and Biosphere with Implications for the Future, *Annual Review of Earth and Planetary Sciences*, *39*(1), 489-516.

Moore, E. A., and A. C. Kurtz (2008), Black carbon in Paleocene-Eocene boundary sediments: A test of biomass combustion as the PETM trigger, *Palaeogeography, Palaeoclimatology, Palaeoecology*, *267*(1-2), 147-152.

Moss, S., J. K. Russell, and G. D. M. Andrews (2008), Progressive infilling of a kimberlite pipe at Diavik, Northwest Territories, Canada: Insights from volcanic facies architecture, textures, and granulometry, *Journal of Volcanology and Geothermal Research*, *174*(1-3), 103-116.

Nielsen, T. F. D., and S. M. Jensen (2005), The Majuagaa kimberlite dyke, Maniitsoq, southern West Greenland, *Geological Survey of Greenland and Denmark, Report 2005/43*.

Nielsen, T. F. D., and K. K. Sand (2008), The Majuagaa kimberlite dike, Maniitsoq region, West Greenland: Constraints on an Mg-rich silicocarbonatitic melt composition from groundmass mineralogy and bulk compositions, *Canadian Mineralogist*, *46*(4), 1043-1061.

Nowicki, T., L. Porritt, B. Crawford, and B. Kjarsgaard (2008), Geochemical trends in kimberlites of the Ekati property, Northwest Territories, Canada: Insights on volcanic and resedimentation processes, *Journal of Volcanology and Geothermal Research*, *174*(1-3), 117-127.

Nowicki, T., B. Crawford, D. Dyck, J. Carlson, R. McElroy, P. Oshust, and H. Helmstaedt (2004), The geology of kimberlite pipes of the Ekati property, Northwest Territories, Canada, *Lithos*, *76*(1-4), 1-27.

Ootto, J. W., and P. J. Wyllie (1993), Relationships between silicate melts and carbonate-precipitating melts in CaO-MgO-SiO_2-CO_2-H_2O at 2 kbar, *Mineralogy and Petrology*, *48*(2-4), 343-365.

Panchuk, K., A. Ridgwell, and L. R. Kump (2008), Sedimentary response to Paleocene-Eocene Thermal Maximum carbon release: A model-data comparison, *Geology*, *36*(4), 315-318.

Patterson, M., D. Francis, and T. McCandless (2009), Kimberlites: Magmas or mixtures?, *Lithos*, *112*(Supplement 1), 191-200.

Pell, J. A. (1997), Kimberlites in the Slave Craton, Northwest Territories, Canada: a preliminary review, *Russian Geology and Geophysics*, *38*(1).

Rohl, U., T. J. Bralower, G. Norris, and G. Wefer (2000), New chronology for the late Paleocene thermal maximum and its environmental implications, *Geology*, *28*, 927-930.

Russell, J. K., L. A. Porritt, Y. Lavallee, and D. B. Dingwell (2012), Kimberlite ascent by assimilation-fuelled buoyancy, *Nature*, *481*(7381), 352-356.

Scott Smith, B. H. (2008), Canadian kimberlites: Geological characteristics relevant to emplacement, *Journal of Volcanology and Geothermal Research*, *174*(1-3), 9-19.

Secord, R., P. D. Gingerich, K. C. Lohmann, and K. G. MacLeod (2010), Continental warming preceding the Palaeocene-Eocene thermal maximum, *Nature*, *467*(7318), 955-958.

Self, S., M. Widdowson, T. Thordarson, and A. E. Jay (2006), Volatile fluxes during flood basalt eruptions and potential effects on the global environment: A Deccan perspective, *Earth and Planetary Science Letters*, *248*(1-2), 518-532.

Skinner, E. M. W., and J. S. Marsh (2004), Distinct kimberlite pipe classes with contrasting eruption processes, *Lithos*, *76*(1-4), 183-200.

Sluijs, A., H. Brinkhuis, S. Schouten, S. M. Bohaty, C. M. John, J. C. Zachos, G.-J. Reichart, J. S. Sinninghe Damste, E. M. Crouch, and G. R. Dickens (2007), Environmental precursors to rapid light carbon injection at the Palaeocene/Eocene boundary, *Nature*, *450*(7173), 1218-1221.

Snyder, D. B., and G. D. Lockhart (2005), Kimberlite trends in NW Canada, *Journal of the Geological Society*, *162*(5), 737-740.

Sobolev, S. V., A. V. Sobolev, D. V. Kuzmin, N. A. Krivolutskaya, A. G. Petrunin, N. T. Arndt, V. A. Radko, and Y. R. Vasiliev (2011), Linking mantle plumes, large igneous provinces and environmental catastrophes, *Nature*, *477*(7364), 312-316.

Sparks, R. S. J., M. C. Gardeweg, E. S. Calder, and S. J. Matthews (1997), Erosion by pyroclastic flows on Lascar Volcano, Chile, *Bulletin of Volcanology*, *58*(7), 557-565.

Sparks, R. S. J., L. Baker, R. J. Brown, M. Field, J. Schumacher, G. Stripp, and A. Walters (2006), Dynamical constraints on kimberlite volcanism, *Journal of Volcanology and Geothermal Research*, *155*(1-2), 18-48.

Stasiuk, L. D., G. D. Lockhart, W. W. Nassichuk, and J. A. Carlson (1999), Thermal maturity evaluation of dispersed organic matter inclusions from kimberlite pipes, Lac de Gras, Northwest Territories, Canada, *International Journal of Coal Geology*, *40*(1), 1-25.

Stasiuk, M. V., C. Jaupart, and R. S. J. Sparks (1993), On the variations of flow rate in non-explosive lava eruptions, *Earth and Planetary Science Letters*, *114*(4), 505-516.

Svensen, H. (2004), Release of methane from a volcanic basin as a mechanism for initial Eocene global warming, *Nature*, *429*, 542-545.

Sweet, A. R., Stasiuk, M., Nassichuk, W.W., McIntyre, D.J., Catunneau, O. (2003), Stratigraphy, paleoenvironments and thickness of inferred sedimentary cover and kimberlite crater fill processes, Lac de Gras, Northwest Territories, Canada, *Proceedings of the Eighth International Kimberlite Conference, Victoria, British Columbia, Canada*.

Thomas, D. J., J. C. Zachos, T. J. Bralower, E. Thomas, and S. Bohaty (2002), Warming the fuel for the fire: Evidence for the thermal dissociation of methane hydrate during the Paleocene-Eocene thermal maximum, *Geology*, *30*(12), 1067-1070.

Thomas, E. (2003), Extinction and food at the seafloor: A high-resolution benthic foraminiferal record across the initial Eocene thermal maximum, Southern Ocean site 690, *Geological Society of America Special Papers*, *369*, 319-332.

Thomas, E., and N. J. Shackleton (1996), The Paleocene-Eocene benthic foraminiferal extinction and stable isotope anomalies, *Geological Society, London, Special Publications*, *101*(1), 401-441.

Thomas, E., and J. C. Zachos (2000), Was the late Paleocene thermal maximum a unique event?, *Geol. For. Stockh. Forh. [Trans. Geol. Soc. Stockholm]*, *122*, 169-170.

Tripati, A., and H. Elderfield (2005), Deep-Sea Temperature and Circulation Changes at the Paleocene-Eocene Thermal Maximum, *Science*, *308*(5730), 1894-1898.

Wignall, P. B. (2001), Large igneous provinces and mass extinctions, *Earth-Science Reviews*, *53*(1-2), 1-33.

Wilson, L., and J. W. Head III (2007), An integrated model of kimberlite ascent and eruption, *Nature*, *447*(7140), 53-57.

Zachos, J. C. (2003), A transient rise in tropical sea surface temperature during the Paleocene-Eocene thermal maximum, *Science*, *302*, 1151-1154.

Zachos, J. C. (2004), Early Cenozoic Extreme Climates: The Walvis Ridge Transect, edited.

Zachos, J. C., K. C. Lohmann, J. C. G. Walker, and S. W. Wise (1993), Abrupt Climate Change and Transient Climates during the Paleogene: A Marine Perspective, *The Journal of Geology*, *101*(2), 191-213.

Zachos, J. C., M. Pagani, L. C. Sloan, E. Thomas, and K. Billups (2001), Trends, rhythms, and aberrations in global climate 65[thinsp]Ma to present, *Science*, *292*, 686-693.

Zachos, J. C., S. M. Bohaty, C. M. John, H. McCarren, D. C. Kelly, and T. Nielsen (2007), The Palaeocene–Eocene carbon isotope excursion: constraints from individual shell planktonic foraminifer records, *Philosophical Transactions of the Royal Society A: Mathematical, Physical and Engineering Sciences*, *365*(1856), 1829-1842.

Zachos, J. C., et al. (2005), Rapid acidification of the ocean during the Paleocene-Eocene thermal maximum, *Science*, *308*(5728), 1611-1615.

Zeebe, R. E., J. C. Zachos, and G. R. Dickens (2009), Carbon dioxide forcing alone insufficient to explain Palaeocene-Eocene Thermal Maximum warming, *Nature geosciences*, *2*(8), 576-580.

Figures

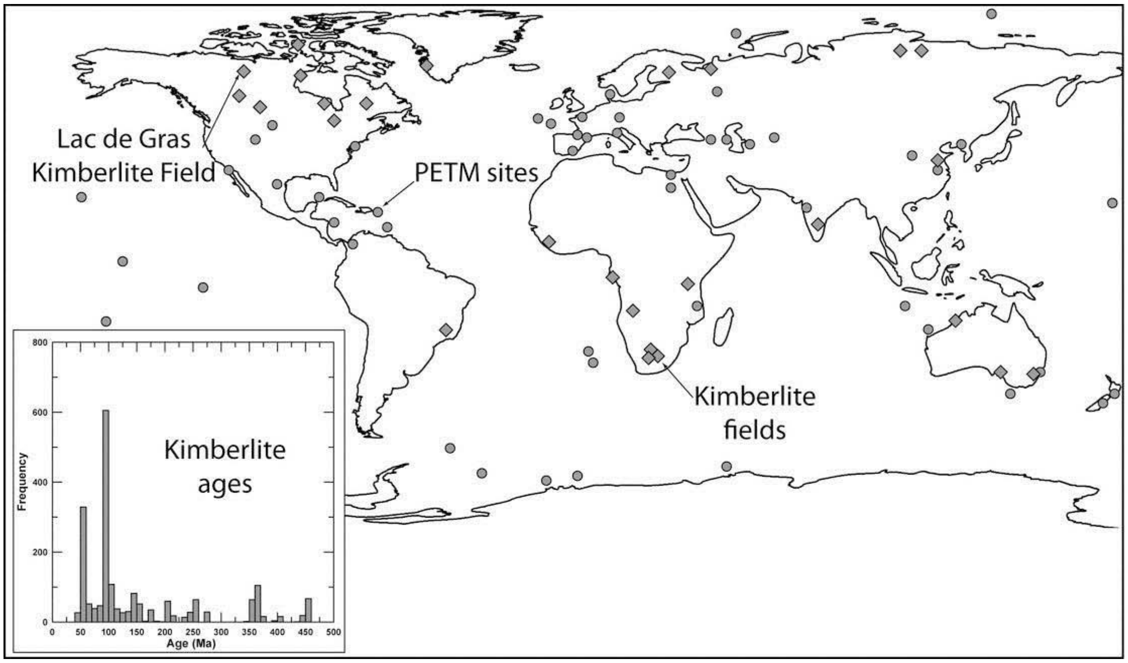

Figure 4- 1: World map illustrating the major kimberlite fields containing hundreds of kimberlite pipes and (inset) illustrating the temporal clusters of kimberlite eruption episodes (Location and age data – [*Faure*, 2010]). Diamond – major kimberlite occurrence; circles – representative selection of sample sites containing PETM sediment [*McInerney and Wing*, 2011; *J. C. Zachos et al.*, 2005]. For additional sites of both kimberlite eruptions and hyperthermal locations, please refer to the exhaustive list in references.

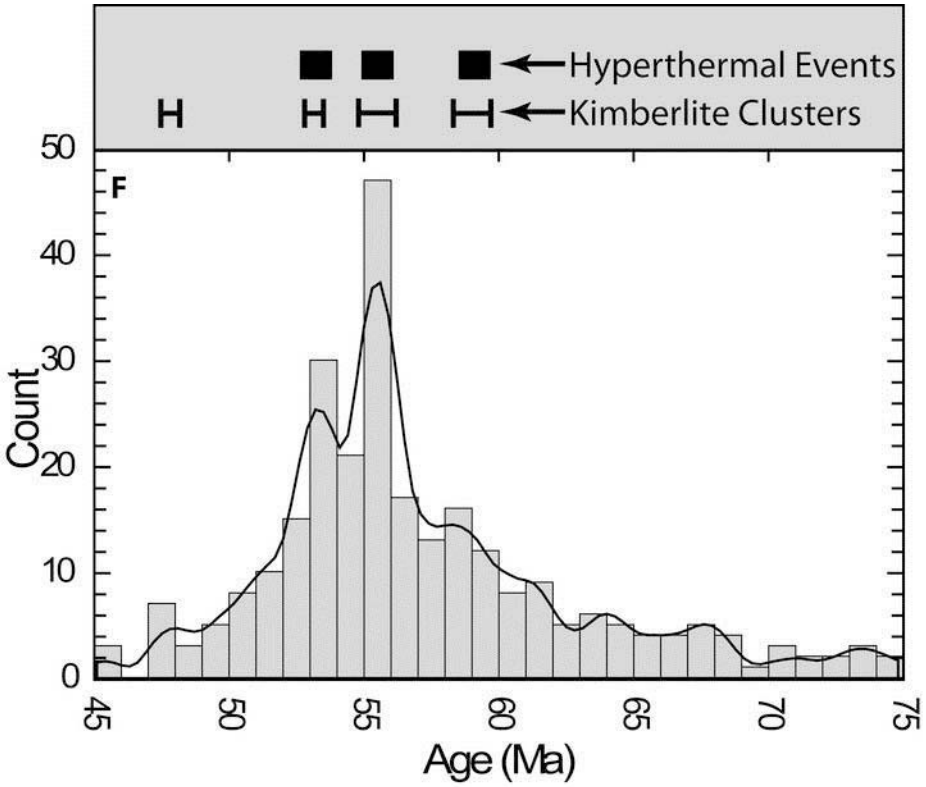

Figure 4- 2: Histogram of showing the final distribution of Lac de Gras kimberlite emplacement age (rationale available in text), hyperthermal events, and main kimberlite clusters indicated (age data references same as in text).

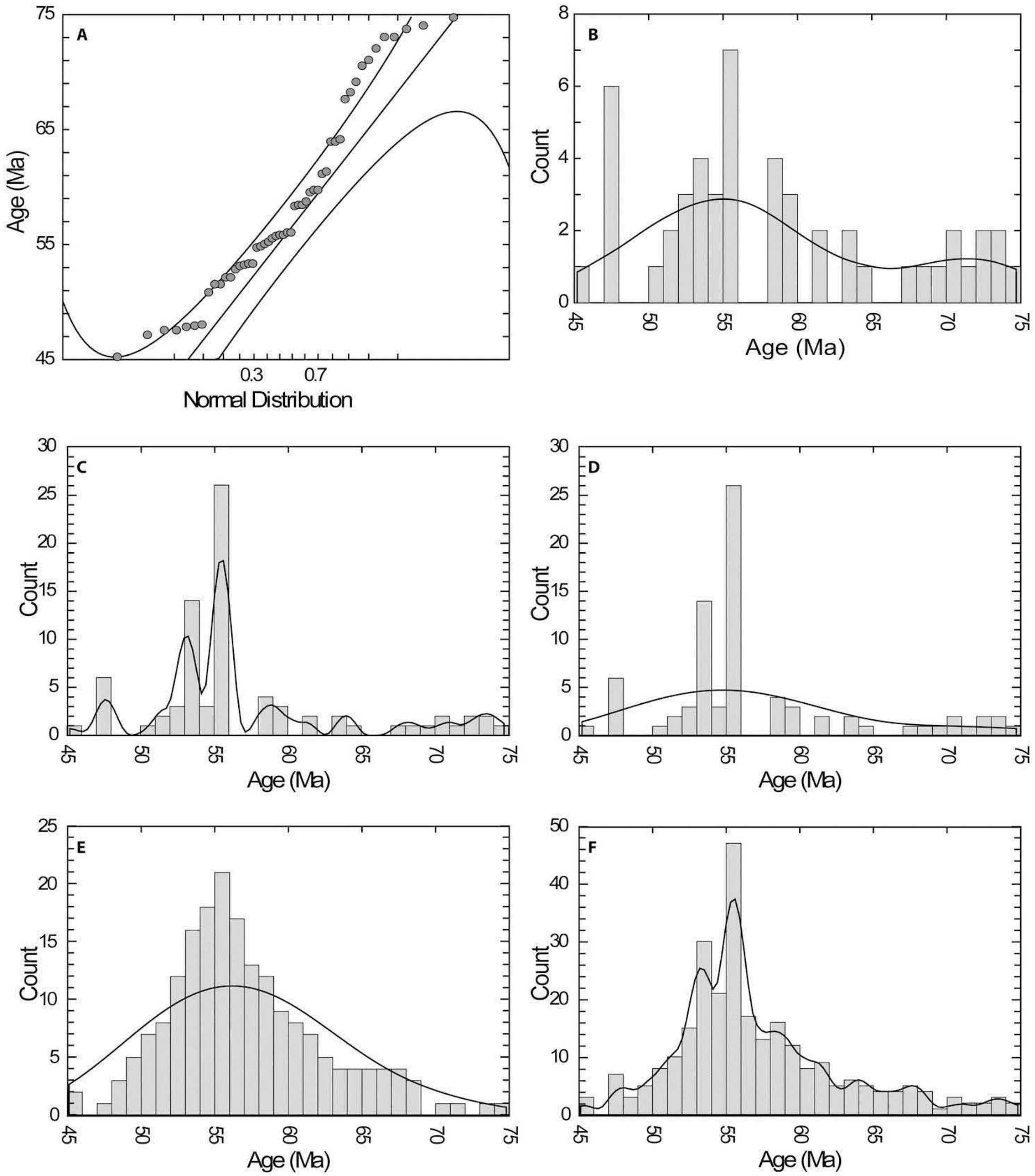

Figure 4- 3: Series of statistical probability, histogram plots and density traces results from NCSS statistical software that illustrates our statistical approach during reconstruction of the age distribution for the Lac de Gras kimberlite field. A – Probability plot showing the age clusters similar to previous studies [*Lockhart et al.*, 2004]; B – histogram and density trace line for 50 known kimberlite ages reported for the Lac de Gras kimberlite field; C – histogram and density

trace of the 50 known kimberlite ages and the additional 29 kimberlites assigned to the 55.5 and 53.2 age clusters; D – same data as panel C, however, density trace forced into smoothest curve to illustrate over all age distribution for the Lac de Gras kimberlite field, note the mode at ~56 Ma; E – histogram of random age data generated to produce similar density trace distribution as seen in panel D, note mode at ~56 Ma; F – histogram and density trace resulting from adding data in panel C and panel E.

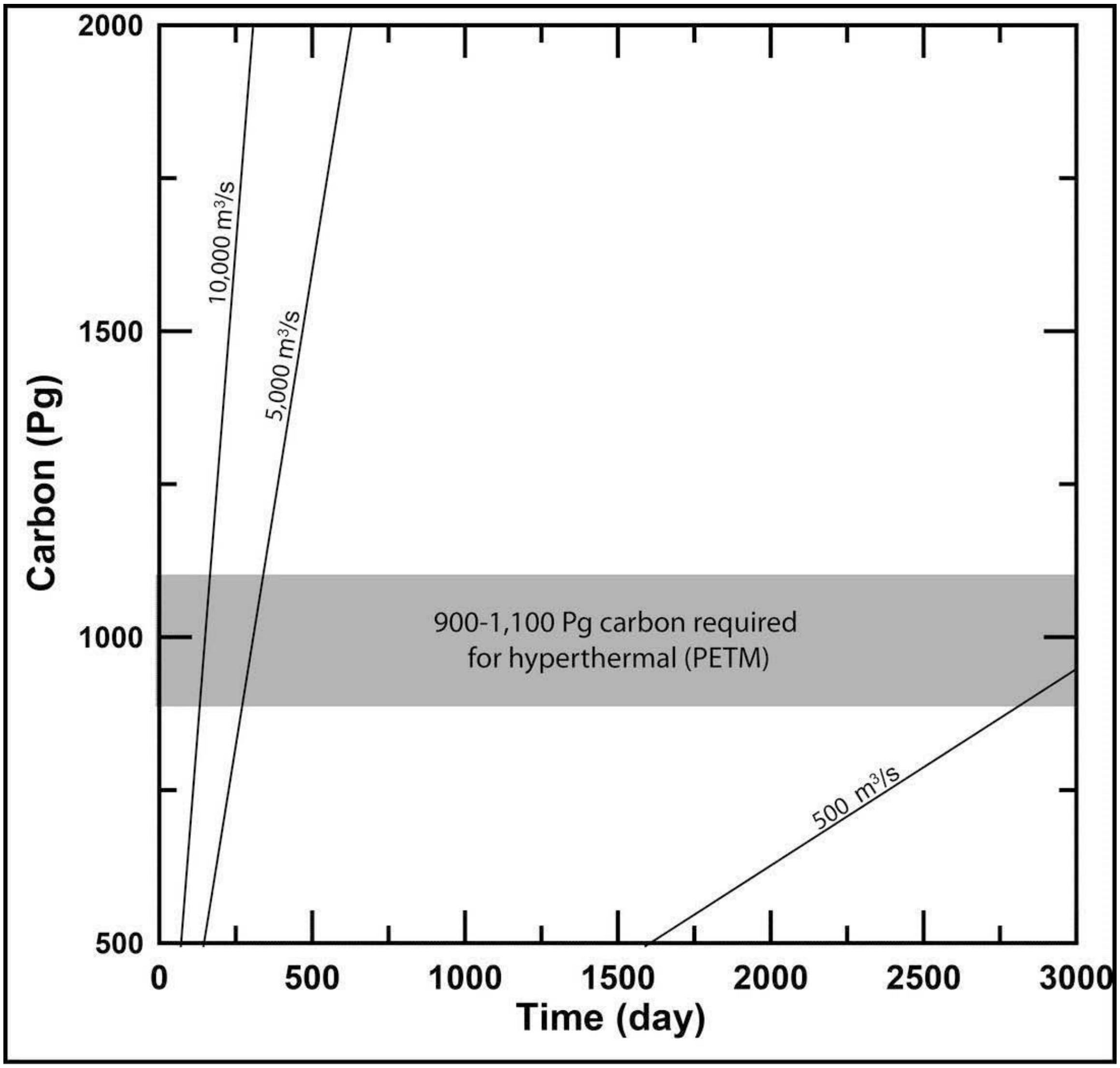

Figure 4- 4: Plot of carbon versus time produced by cluster of 50 kimberlites with varying magma supply rates. Range of carbon required to produce 3 °C of initial warming indicated by shaded box.

CHAPTER 5

General Conclusions

Despite many years of investigation, the nature of kimberlite magma remains debated, with some going as far as *positively asserting that this problem will never be solved by science*. In part, this capitulation is due to the hybrid, often contaminated and altered nature of kimberlite, as well as the absence of rapidly-quenched lavas that might represent primary kimberlite liquids. Identification of a suitable composition as a candidate that approximates a relatively primary magma is certainly difficult, however recent studies on kimberlite have shown that the contamination and alteration of kimberlite can be effectively mitigated during sample selection and preparation. Often the hybrid nature of kimberlite is thought to pose an insurmountable challenge, however, the major primary components of kimberlite are simple: olivine and carbonate, both of a mantle origin. Approaching kimberlite from this well-established fact, and applying the principles of igneous petrology, the nature of kimberlite magma is evident.

Chapter 2 is titled “The implications of xenocrystic olivine magmatic margins for kimberlite magma composition,” and it utilizes conventional analytical methods (Electron microprobe and x-ray fluorescence) to gather compositional data for olivine and the bulk rock kimberlite. The principles of igneous petrology are then employed to model crystal fractionation and assimilation, allowing the composition of the residual liquid to be tracked. In summary, Chapter 2 of this thesis shows that:

1) The olivine overgrowth margins that develop on xenocrystic olivine in kimberlite represent the crystallization of olivine from kimberlite magma that has assimilated orthopyroxene derived from the cratonic mantle;

2) That the $k_{D(Fe/Mg)}$ for olivine crystallization in kimberlite magmas is ~0.3, similar to that of basalts, and therefore the previously high $k_{D(Fe/Mg)}$ of >0.5 are not reasonable;
3) Magmatic olivine accounts for only 5-15% of the kimberlite modal mineralogy;
4) The compositions of magmatic margins on kimberlite olivine constrain the composition of kimberlite magma as silico-carbonatite.

Chapter 3 is titled “Constraining the compositions of kimberlite magma using pelletal lapilli.” It introduces a novel technique to analyze the composition of pelletal lapilli that were previously too small to analyze using conventional methods. Large pelletal lapilli were analyzed using both broad beam electron microprobe (EMP) analysis and x-ray fluorescence (XRF). The compositions resulting from the two techniques were found to be indistinguishable, thus establishing that EMP analysis does produce an accurate lapilli composition. This allows for the same EMP analytical technique to be employed in analyzing pelletal lapilli for major element chemistry at the millimeter scale, with image analysis used as a supplement. The compositional trend of the pelletal lapilli was then compared to the compositional trend of the host kimberlite and it was found that the two trends converge. In summary, Chapter 3 of this thesis indicates that:

1) The composition of small samples can be reliably analyzed using a broad beam electron microprobe technique;
2) The compositional variation of the pelletal lapilli suggests that the variation reflects magmatic evolution due to orthopyroxene assimilation;

3) The convergence of the pelletal lapilli trend and kimberlite bulk rock trend approximates the composition of the kimberlite magma and is similar to magma compositions derived by the xenocrystic mantle extraction method.

Chapter 4 is titled “Kimberlite eruptions as triggers for early Cenozoic hyperthermals,” and it examines the possible climatic effects of a kimberlite eruption. The impetus of this study was to answer the question that is invariably left unanswered by studies of the Paleocene-Eocene Thermal Maximum (PETM): what was the source of the initial CO_2 in-flux? Applying a statistical model to this data set, an estimation of the mass of carbon produced during eruption was calculated. This mass was found to either match or exceed the mass that the paleo-climatology community has determined is required to trigger the sequence of events that lead to the PETM. Employing a compilation of kimberlite age dates, documented kimberlite occurrences and structural controls on kimberlite emplacement, I have attempted to reconstruct the eruption history of the Lac de Gras kimberlite field. It was found that the ages of the kimberlite eruptions in question are indistinguishable from the PETM and two other Cenozoic hyperthermals. In summary, Chapter 4 concludes that;

1) Three early Cenozoic hyperthermal events that require a large mass of carbon to be injected into the atmosphere are coincident with three major kimberlite eruptions;
2) The volume of CO_2 degassed from large kimberlite eruptions is sufficient to satisfy the mass of carbon required for the global temperature increase involved in triggering the hyperthermals;

3) Most importantly, the rate at which kimberlite degasses CO_2 to the atmosphere will overcome the oceans' ability to buffer atmosphere CO_2 partial pressure.

The silico-carbonatite nature of kimberlite magma is incontrovertible if the observer recognizes that kimberlite has two major components: olivine and carbonate. Carbonate that is found in kimberlite has a mantle origin, based on its isotopic signature, and must therefore be considered a chemical constituent of the magma composition. The vast majority (85-95%) of the olivine found in kimberlite is xenocrystic and is derived from the cratonic mantle; olivine must therefore *not* be considered a major chemical constituent of the magma composition. That very little olivine crystallizes from the kimberlite magma suggests that silica content is too low for the melt to be silicic in character. The simple mathematical extraction of the xenocrystic olivine composition from a kimberlite bulk rock composition results in a silico-carbonatite magmatic composition. More involved models that take into account orthopyroxene assimilation and the resulting crystallization of a small amount of olivine still yield similar silico-carbonatitic compositions. Thorough analysis of olivine overgrowth margins and pelletal lapilli both clearly point to a silico-carbonatitic magma composition. A silico-carbonatitic magma composition is thus supported by petrographic evidence, xenocrystic extraction models, and the geochemistry of the most primary materials available. The most simple explanation for kimberlite, the one that struck me the first time I saw kimberlite in thin section, is thus supported by the most reliable and time-tested methods known to geology.

This truth, firmly based on first-order principles and well-supported by major element geochemistry, cannot be discredited with any amount of trace element or isotopic minutiae. As the analytical abilities available to geologists have increased exponentially over the decades, there has developed a tendency to focus on measurements made on the micro- and nano-scale. While there are indisputably insights to be gleaned from this data, perspective must be kept. If the trace element or isotopic data appears to contradict the major element data, the major element data must be taken to be the most reliable. In the case of kimberlite, the petrography and the major element geochemistry point to a silico-carbonatitic magma composition; arguing that the kimberlite magma is silicic in character based solely on trace elements or isotopes ignores the hierarchy of scale. Similarly, it has been shown in this thesis that the $k_{D(Fe/Mg)}$ for olivine crystallization is ~0.3, just as it is universally in magmatic systems; changing olivine's $k_{D(Fe/Mg)}$ in order to make a silicic magma composition work is desperate and unreasonable.

The motivation behind these attempts at proving a silicic composition for kimberlite magmas is that a silicic composition allows for kimberlite to be consistent within the plate tectonic model. A silico-carbonatitic composition, while not directly contradictory to plate tectonics, operates outside of the framework of plate tectonics. This prospect appears to cause discomfort amongst many kimberlite researchers. However, the abundance of evidence for a silico-carbonatitic kimberlite magma, unrelated to plate tectonic processes as they are understood, precludes the possibility of rational denial. The fact that the debate is still on-going is therefore a case of "real science" butting up against "normal science." The most reliable lines of study and first-order principles both indicate a silico-carbonatitic magma composition; the normal science rejects the idea and all its supporting evidence because it does not fit into the currently-accepted paradigm of plate tectonics.

However, it is time for the debate to move on. With reasonable constraints on the composition of the kimberlite magma, a myriad of other interesting questions may be addressed with confidence. While the composition of the kimberlite parental magma was addressed in Chapters 2 and 3, the most fascinating result of this thesis is the effect that the eruptions of large kimberlite fields have on climate. The rare connection between the deep mantle and atmospheric reservoirs is examined, with catastrophic implications. Three examples of this interaction are seen in the early Cenozoic hyperthermal events. Gargantuan amounts of carbon are rapidly injected from the mantle into the atmosphere through the Lac de Gras kimberlite eruptions, and the timing of these catastrophic eruptions coincides with three significant hyperthermals of the Cenozoic.

As science becomes more diverse and scientists more specialized, there are basic unifying principles that must not be lost. Adherence to first principles must not be forgotten, even amidst the abundance of data. Major element chemistry must not be ignored, even with the omnipresence of trace element and isotopic data. A holistic view of the world must not be sacrificed for a compartmentalized, shuttered practice; that is how unexpected answers remain undiscovered. As scientists, as geologists, it is our responsibility to not only to judge new and challenging ideas on their merits, and not on our prejudices, but to seek out answers, even in the most unforeseen of places.

APPENDIX A

Patterson M. V., and D. Francis (2013) Kimberlite eruptions as triggers for early Cenozoic hyperthermals, Geochem. Geophys. Geosys., 14, 448–456, doi:10.1002/ggge.20054.

Geochemistry
Geophysics
Geosystems
G3

Published by AGU and the Geochemical Society

Article
Volume 14, Number 2
28 February 2013
doi:10.1002/ggge.20054
ISSN: 1525-2027

Kimberlite eruptions as triggers for early Cenozoic hyperthermals

Michael V. Patterson and Don Francis
Earth and Planetary Sciences, McGill University, 3450 University Street, Montreal, Quebec, Canada, H3A 2A7 (Bodhi111@gmail.com)

[1] The early Cenozoic experienced at least three short but major hyperthermals associated with disruptions of the global carbon cycle. The largest among those, the Paleocene-Eocene thermal maximum, was associated with a negative carbon isotopic excursion of ~ 2.5‰ that appears to be best explained by the thermal dissociation of methane hydrates due to an initial period of warming. The cause of the initial warming has been attributed to a massive injection of carbon (CO_2 and/or CH_4) into the atmosphere; however, the source of the carbon is as yet unknown. The emplacement of a large cluster of kimberlite pipes at ~56 Ma in the Lac de Gras region of northern Canada may have provided the carbon that triggered early warming in the form of exsolved magmatic CO_2. Our calculations indicate that the estimated 900–1100 Pg of carbon required for the initial ~3°C of ocean water warming associated with the Paleocene-Eocene thermal maximum could have been released during the emplacement of a large kimberlite cluster. The coeval ages of two other kimberlite clusters in the Lac de Gras field and two other early Cenozoic hyperthermals indicate that CO_2 degassing during kimberlite emplacement is a plausible source of the CO_2 responsible for these sudden global warming events.

Components: 5,800 words, 4 figures.

Keywords: paleoclimate; kimberlite; Cenozoic hyperthermals.

Index Terms: 0473 Biogeosciences: Paleoclimatology and paleoceanography (3344, 4900).

Received 29 March 2012; **Revised** 17 December 2012; **Accepted** 18 December 2012; **Published** 28 February 2013.

Patterson M. V., and D. Francis (2013) Kimberlite eruptions as triggers for early Cenozoic hyperthermals, *Geochem. Geophys. Geosys.*, *14*, 448–456, doi:10.1002/ggge.20054.

1. Introduction

[2] The Paleocene-Eocene thermal maximum (PETM) is an early Cenozoic hyperthermal that occurred both on land and in the ocean. It is associated with a global disturbance in carbon isotopes and a global dissolution of $CaCO_3$ sediments. On the basis of these and other environmental changes, the PETM has been related to an enormous release of CO_2 and/or CH_4 [*Dickens et al.*, 1997]. Although the sequence of the events during the PETM are difficult to piece together, the available evidence indicates early warming, followed by a more drastic warming coincident with a negative shift in $\delta^{13}C$ [*Carozza et al.*, 2011; *Leon-Rodriguez and Dickens*, 2010; *Secord et al.*, 2010; *Sluijs et al.*, 2007; *D. J. Thomas et al.*, 2002]. Although the negative carbon isotopic excursion (CIE) associated with the PETM has been attributed to carbon released from methane hydrates on the sea floor, the source of carbon that produced the early warming that

destabilized these hydrates is yet unknown [*Bowen et al.*, 2004; *Bralower et al.*, 1997; *Carozza et al.*, 2011; *Dickens*, 2000; *Dickens et al.*, 1995, 1997; *Hancock and Dickens*, 2005; *Kent*, 2003; *Lourens et al.*, 2005; *Moore and Kurtz*, 2008; *Panchuk et al.*, 2008; *Sluijs et al.*, 2007; *D. J. Thomas et al.*, 2002; *E. Thomas*, 2003; *E. Thomas and Shackleton*, 1996; *E. Thomas and Zachos*, 2000; *Tripati and Elderfield*, 2005; *Zachos*, 2003, 2004; *Zachos et al.*, 1993, 2001, 2005, 2007; *Zeebe et al.*, 2009]. In this paper, we propose that the initial warming that occurred during the early stages of the PETM (and two other early Cenozoic hyperthermals) was caused by the release of CO_2 during the eruption of a large cluster of kimberlite pipes in the Lac de Gras kimberlite field of the Slave Province, Canada.

2. Background

[3] Several proposals have been offered to explain the PETM including: comet impact [*Kent*, 2003], global wild fires [*Kurtz et al.*, 2003], volcanic activity [*Svensen*, 2004], and methane hydrate dissociation [*Dickens et al.*, 1997]. The lack of extra-terrestrial tracer material in CIE deposits, such as iridium anomalies, and the discovery that magnetotactic bacteria is the cause of magnetically anomalous clay layers renders the impact hypothesis unlikely [*Kopp et al.*, 2007]. The relative absence of anomalous graphitic black carbon in the PETM sediments argues against the possibility that global wildfires were the cause of the PETM [*Moore and Kurtz*, 2008]. Typical basaltic volcanic activity is also an unlikely source of this initial CO_2 because of the low CO_2 contents of basalts (< 1 wt %) associated with large igneous provinces and their slow eruption rates [*Blundy et al.*, 2010; *Caldeira and Rampino*, 1991; *Gerlach et al.*, 2002; *Keeling et al.*, 1995; *Sobolev et al.*, 2011]. Furthermore, volcanic SO_2 released during large igneous province eruptions forms considerable amounts of atmospheric sulfate aerosols, which would cause global cooling [*Self et al.*, 2006]. The release of thermogenic methane produced by igneous intrusions into organic-rich sediments would require that the CIE precedes the ocean water warming event, contrary to the observed isotopic data. Although methane from hydrate dissociation is thought to have played a pivotal role during the PETM, because it is highly depleted in ^{13}C and a strong greenhouse gas, its role is most consistent with having caused the CIE and not the initial warming.

[4] The negative shift of $\delta^{13}C$ (CIE) during the PETM is thought to be related to a geologically rapid (<10 kyr) carbon release that was significantly depleted in ^{13}C [*Röhl et al.*, 2000; *Zachos et al.*, 2007]. Prior to the light carbon injection, a brief period of oceanic [*Sluijs et al.*, 2007; *D. J. Thomas et al.*, 2002] and continental [*Secord et al.*, 2010] warming, as well as dissolution of seafloor carbonates [*Leon-Rodriguez and Dickens*, 2010], is thought to have occurred, indicating that the carbon input that caused the CIE is unlikely to have produced the initial warming. Recent models of carbon emissions during the PETM indicate that it is characterized by an initial period of warming and carbonate dissolution requiring ~1000 Pg of carbon, which is then followed by a rapid input of depleted carbon that caused the CIE [*Carozza et al.*, 2011]. There are few carbon reservoirs available that could contribute to the early warming, without resulting in large $\delta^{13}C$ excursions, because organic matter and methane hydrates are strongly depleted in ^{13}C.

3. Observations

[5] The Earth's mantle is a vast reservoir of carbon, likely equivalent to all other carbon reservoirs combined. Normally, mantle carbon leaks out slowly through mid-ocean ridges and volcanoes, at rates of 10^{-3} Pg/yr of carbon [*Caldeira and Rampino*, 1991], three orders of magnitude lower than that required for hyperthermals (~1 Pg/yr; [*Zeebe et al.*, 2009]). However, in rare circumstances, direct conduits between the deep mantle and the atmosphere are provided by rapid explosive kimberlite eruptions. In contrast, the CO_2 contents of basaltic magmas in large volcanic provinces (i.e., shield volcanoes or flood basalts) are estimated to be $<< 1$ wt % [*Blundy et al.*, 2010; *Gerlach et al.*, 2002; *Keeling et al.*, 1995; *Sobolev et al.*, 2011] and although large volcanic provinces provide vast amounts of lava (10^5–10^6 km^3), thus vast amounts of CO_2, they are emplaced over timescales of millions of years [*Wignall*, 2001]. Kimberlite fields are found on every continent, and throughout at least the last 1 billion years of the geological record, and their emplacement is distinct in that they occur in discrete fields and during distinct episodes (Figure 1).

[6] Magmatic kimberlite rocks have very high carbonate contents (CO_2 ~20 wt %; [*Brooker et al.*, 2001; *Francis and Patterson*, 2009; *Nielsen and Jensen*, 2005; *Patterson et al.*, 2009; *Sparks et al.*, 2006]), yet volcanoclastic kimberlite rocks are relatively carbonate-poor ($CO_2 < 5$ wt %) and characterized by the final crystallization of monticellite,

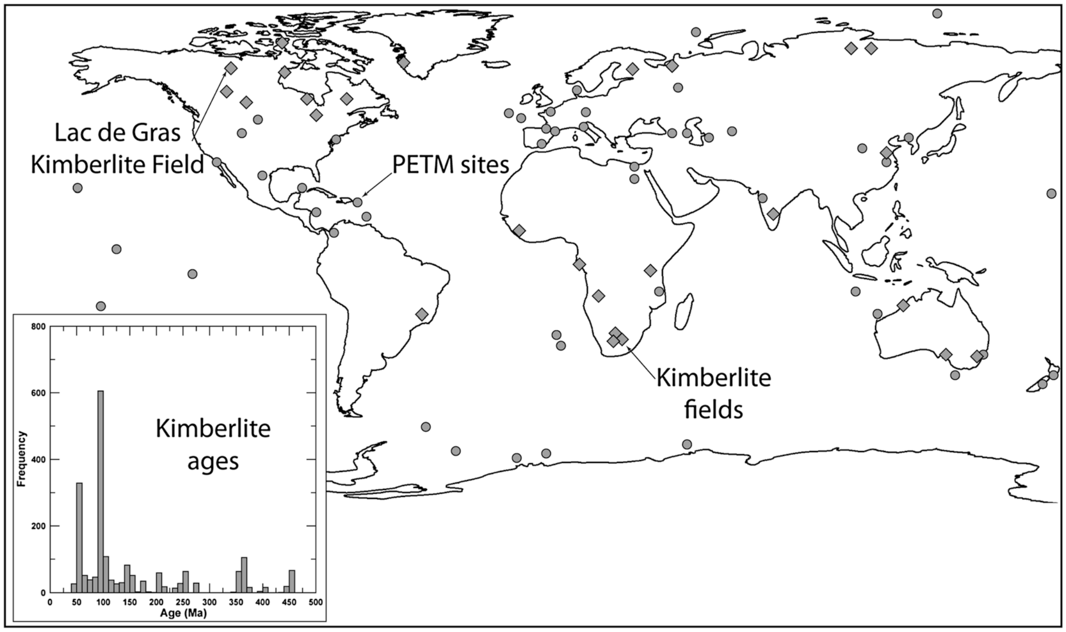

Figure 1. World map illustrating the major kimberlite fields containing hundreds of kimberlite pipes and (inset) illustrating the temporal clusters of kimberlite eruption episodes (Location and age data – *Faure* [2010]). Diamond – major kimberlite occurrence; circles – representative selection of sample sites containing PETM sediment [*McInerney and Wing*, 2011; *Zachos et al.*, 2005]. For additional sites of both kimberlite eruptions and hyperthermal locations, please refer to the exhaustive list in references.

phlogopite, and diopside at the expense of the typical carbonate-rich matrix that characterizes magmatic kimberlite [*Skinner and Marsh*, 2004; *Sparks et al.*, 2006]. That is as CO_2 degasses from the ascending magma, the a_{SiO2} of the melt increased to levels that favor crystallization of silicate minerals (i.e., monticellite, phlogopite and diopside) in the simple $CaO\text{-}MgO\text{-}SiO_2\text{-}CO_2$ system [*Canil and Bellis*, 2008; *Franz and Wyllie*, 1967; *Ootto and Wyllie*, 1993]. Thus, the transition from magmatic kimberlite to volcanoclastic kimberlite is associated with the release of CO_2. Kimberlite magma is estimated to rise to the surface in a matter of hours and have eruption durations on the order of weeks, thus significant amounts of CO_2 can be released at high rates.

[7] The ages of the three early Cenozoic hyperthermals (~59.2, 55.5, and 53.2 Ma; [*Charles et al.*, 2011; *Hancock and Dickens*, 2005; *Lourens et al.*, 2005; *E. Thomas and Zachos*, 2000]) are indistinguishable from three of the four ages of kimberlite clusters that comprise the Lac de Gras kimberlite field of northern Canada. There are over 270 kimberlites in the Lac de Gras kimberlite field that range in age from 74 to 45 Ma, with at least four distinct age and spatial clusters: 59.0±0.7, 55.5±0.7, 53.2±0.3, and 47.8±0.3 Ma [*Creaser et al.*, 2004; *Graham et al.*, 1999]. Reversals in magnetic polarity in the Lac de Gras kimberlites [*Cande and Kent*, 1995] provide substantially better temporal resolution than that obtained by radiometric dating [*Lockhart et al.*, 2004]. Seismic data indicate that the three younger kimberlite clusters appear to have been emplaced along distinct corridors that represent deep crustal or lithospheric dyke swarms composed of numerous dykes clustered within zones kilometers in width [*Snyder and Lockhart*, 2005]. Although only 50 of the over 270 Lac de Gras kimberlite pipes have precise ages [*Creaser et al.*, 2004; *Graham et al.*, 1999; *Heaman et al.*, 2003], their age data exhibit a clustered distribution (59.0±0.7, 55.5±0.7, 53.2±0.3, and 47.8±0.3 Ma).

[8] Although the ages of the clusters within the Lac de Gras kimberlite field and those of the early Cenozoic hyperthermals have been previously reported, their striking correspondence is first demonstrated here (Figure 2). The lack of age dates for most of the kimberlite pipes in the Lac de Gras field requires a reconstruction of an age distribution for the undated kimberlite pipes to estimate the total number of pipes within each cluster. We have approached this reconstruction by assuming that the unknown age data will have a similar, albeit smooth, distribution as the 50 known ages. Considering that three of the age clusters (55.5±0.7, 53.2±0.3, and 47.8±0.3 Ma) have been shown to be spatially clustered [i.e., *Lockhart et al.*, 2004,

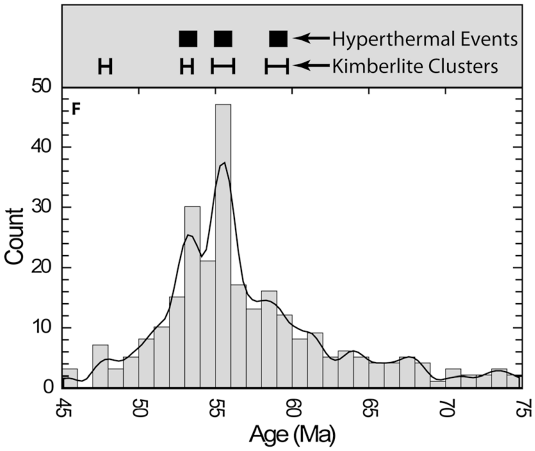

Figure 2. Histogram of showing the final distribution of Lac de Gras kimberlite emplacement age (rationale available in text), hyperthermal events, and main kimberlite clusters indicated (age data references same as in text).

Figure 3], 29 additional undated kimberlite pipes that lie within these intrusive corridors were assigned the mean age for their respective clusters (55.5 = 19; 53.2 = 10). Although age clusters have been demonstrated in the Lac de Gras kimberlite field, it may be reasonable to assume that the remaining kimberlites of unknown age are similarly clustered; we have chosen a simpler distribution approach (Figure 3). The remaining 191 kimberlites are distributed across 45–75 Ma with a similar distribution as the dated kimberlite which have a median age of 55.9. The three methods are then stacked in a histogram resulting with a prominent mode at 55.9 Ma. The modes corresponding to four kimberlite clusters are at 59.0 Ma (*n*= 12), 55.9 Ma (*n*= 50), 53.2 Ma (*n*= 33), and 47.8 Ma (*n*= 7). The three older kimberlite age clusters correspond within error to three early Cenozoic hyperthermals, one of which is the PETM at 55.5 Ma.

4. Volume Estimates

[9] Kimberlite pipes in the Lac de Gras field have a cone morphology similar to that of the classic South African model [*Field and Scott Smith*, 1997]; however, they tend to be shallow (~950 m; [*Moss et al.*, 2008; *Nowicki et al.*, 2008]), thus they are volumetrically smaller. Phanerozoic strata are missing in the Lac de Gras area, although crustal xenoliths preserved within the kimberlite deposits suggest an original succession of Cretaceous marine shales, terrigenous arenite, and organic peat capping basement rocks during the Early Cenozoic, with variable estimates of thickness ranging from 100 to 300 m [*Nowicki et al.*, 2004; *Pell*, 1997; *L. D. Stasiuk et al.*, 1999; *Sweet et al.*, 2003]. Detailed studies of kimberlite pipes in the Lac de Gras area indicate that their present depths vary between 400–1100 m [*Moss et al.*, 2008; *Nowicki et al.*, 2008], and thus emplacement depths of ~600–1300 m. Pipe morphology are characterized by steeply dipping walls (~80°; [*Nowicki et al.*, 2008]), yielding an average volume of 3×10^7 m^3 of kimberlite per pipe. Although kimberlite pipes often deviate from a simplified cone-shaped body [*Nowicki et al.*, 2004], such deviations tend to increase volume and thus the foregoing would be a minimum volume estimate. Furthermore, kimberlite pipes are typically excavated multiple times (3–5) by repeated eruption episodes [*Scott Smith*, 2008] and thus the volume of the erupted kimberlite is likely many times that of the observed pipes. The Lac de Gras kimberlite cluster that is coeval with the PETM comprises ~50 known pipes corresponding to a minimum volume of erupted magma 5–8 $\times 10^9$ m^3.

[10] The capacity of kimberlite magma to transport CO_2 is difficult to constrain because a gaseous CO_2 phase is likely to develop as the magma undergoes depressurization during ascent [*Russell et al.*, 2012; *Sparks et al.*, 2006]. *Russell et al.* [2012] demonstrated that the chemical assimilation of orthopyroxene by proto kimberlite magma (carbonatite) would release large amounts of CO_2 due to the decreasing solubility of CO_2 in a melt as the a_{SiO2} increases, thus it is likely that an additional 25–30 wt % of free CO_2 gas is accompanying kimberlite eruptions. The presence of this free gas phase was first demonstrated as a requirement for kimberlite dyke initiation and propagation to explain the ultrarapid ascent of kimberlite from such great depths [*Wilson and Head*, 2007]. Despite the foregoing, the volume of a free CO_2 gas phase is difficult to quantify; however, a minimum constraint on CO_2 in magmatic kimberlite is simply estimated by the stoichiometry of carbonate and the carbonate content of magmatic kimberlite, ~20% of CO_2 by weight [*Brooker et al.*, 2001; *Nielsen and Sand*, 2008; *Patterson et al.*, 2009; *Sparks et al.*, 2006]. The density of magmatic kimberlite is ~3.2×10^6 g/m^3 (80% Fo_{90} and 20% calcite), thus volumes of 5–8 $\times 10^9$ m^3 yield 2–3 $\times 10^{16}$ g of kimberlite. Kimberlite pipes, however, are dominated by volcanoclastic kimberlite rocks, which form through explosive degassing that occurs during kimberlite pipe excavation and thus are CO_2 poor compared to magmatic kimberlite, typically <5% of CO_2 by weight. Calculating the mass of CO_2 degassed during emplacement as a 15% net weight loss, results in 2–4 $\times 10^{15}$ g of CO_2 or

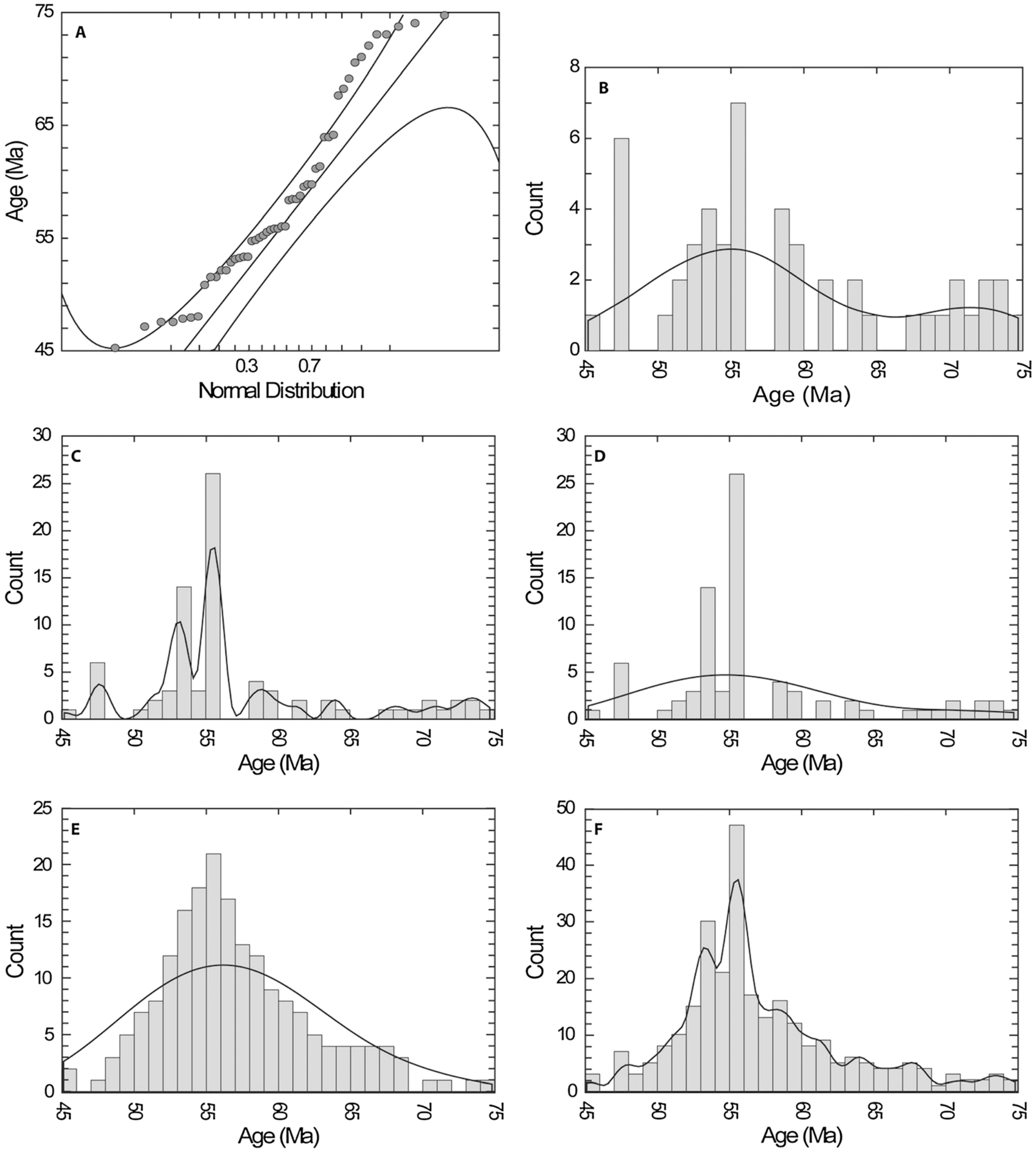

Figure 3. Series of statistical probability, histogram plots and density traces results from NCSS statistical software that illustrates our statistical approach during reconstruction of the age distribution for the Lac de Gras kimberlite field. (A) Probability plot showing the age clusters similar to previous studies [*Lockhart et al*., 2004]; (B) histogram and density trace line for 50 known kimberlite ages reported for the Lac de Gras kimberlite field; (C) histogram and density trace of the 50 known kimberlite ages and the additional 29 kimberlites assigned to the 55.5 and 53.2 age clusters; (D) same data as Figure 3C, however, density trace forced into smoothest curve to illustrate overall age distribution for the Lac de Gras kimberlite field, note the mode at ~56 Ma; (E) histogram of random age data generated to produce similar density trace distribution as seen in Figure 3D, note mode at ~56 Ma; (F) histogram and density trace resulting from adding data in Figures 3C and 3E.

6.0–10.0 × 10^{14} g of carbon per kimberlite cluster, using the observed pipe volume. Studies regarding kimberlite eruption dynamics suggest the range of magma supply rates is 500–10,000 m^3/s [*Sparks et al*., 2006], thus a kimberlite cluster of 55 pipes would degas the above mass of carbon between 5 and 200 days. The eruption of a single kimberlite cluster could release carbon at a rate of ~2–40 Pg/yr. As stated earlier, kimberlite pipes are typically excavated by repeated eruption episodes [*Field and Scott Smith*, 1997], and erupt larger volumes of magma than what remains in the pipes, thus the calculated duration required to produce 1000 Pg of carbon is estimated to be 200–3000 days (Figure 4).

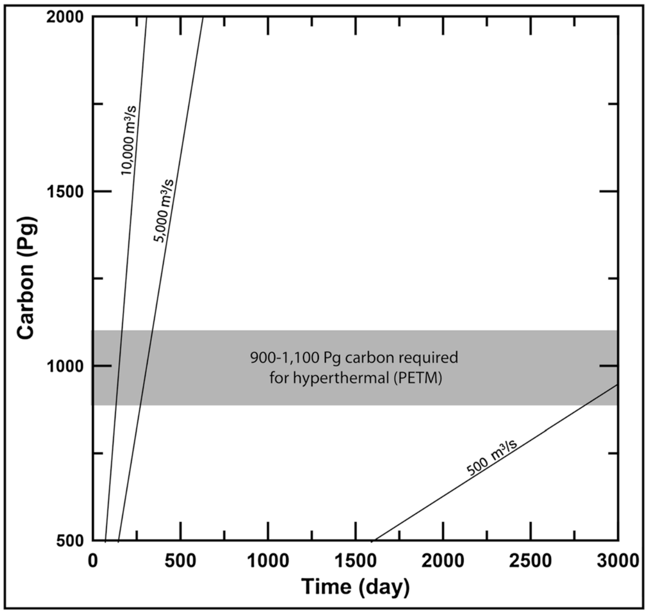

Figure 4. Plot of carbon versus time produced by cluster of 50 kimberlites with varying magma supply rates. Range of carbon required to produce 3°C of initial warming indicated by shaded box.

5. Discussion

[11] Our calculations suggest that kimberlite eruptions release carbon at a rate that far exceeds 1 Pg/yr. Estimates of minimum kimberlite eruption volumes that range from 10^6 to 10^8 m^3 based on observable pipe volumes suggest durations of days to weeks dependent on the magma supply rate (500–10,000 m^3/s; *Sparks et al.* [2006]). These durations are, however, likely to be much shorter than the total duration of the eruptions: (1) the volume estimates are the lower bounds because they do not include the amount of magma ejected out of the kimberlite pipe, and (2) driving pressure in the source region may decline as an eruption proceeds, thus leading to an exponential decrease of magma supply rate, which results in lower estimated supply rates [*Sparks et al.*, 2006; *M. V. Stasiuk et al.*, 1993]. The inferred flow rate (500–10,000 m^3/s) approaches those typical of Plinian eruption columns that reach 10 to 35 km into the stratosphere [*Sparks et al.*, 1997, 2006]. The volume of kimberlite trapped in the pipe is only a small fraction of the total erupted magma and thus the eruptions are likely to be on the order of weeks to months in duration. Calculating the eruption duration if the magma supply rate is increased to 5000 m^3/s, the duration required to produce 900–1100 Pg of carbon is reduced to 300–200 days (Figure 4). Furthermore, even these durations are considered longer than required due to the almost certain presence of a gaseous CO_2 phase that develops during magma ascent.

[12] In addition to the much studied PETM, there are two other hyperthermals with dissolution horizons observed during the late Paleocene to mid-Eocene period that are similar to that associated with the PETM (~55.6 Ma); during the mid-Paleocene at ~59.1 Ma [*Hancock and Dickens*, 2005] and the early-Eocene at ~53.2 Ma [*Lourens et al.*, 2005]. These horizons are similar to the horizon associated with the PETM and are characterized by the presence of a distinct reddish clay layer, an abrupt drop in carbonate content, and a pronounced peak in magnetic susceptibility that is thought to reflect increased clay content [*Bernaola et al.*, 2007]. These two dissolution horizons are characterized by decreased oxygen isotope ($\delta^{18}O$) and carbon isotope ($\delta^{13}C$) values similar to the anomalies associated with the PETM, although of smaller magnitudes [*Hancock and Dickens*, 2005; *Lourens et al.*, 2005]. The similarities between the three hyperthermals have led most workers to consider all three to be sedimentary responses to abrupt climatic change attributed to disruption of the carbon cycle.

[13] The correspondence between the ages of three early Cenozoic hyperthermals and three kimberlite clusters in the Lac de Gras kimberlite field suggests that kimberlite eruption may have provided the CO_2 responsible for the initial global warming that

destabilized marine methane hydrates. Although the analytical uncertainties associated with ages of the Lac de Gras kimberlites are relatively small (~1–2 Ma), it is difficult to discern whether individual kimberlite pipes in a cluster erupt concurrently or sporadically over longer time spans. The spatial trends of the clusters indicate that they belong to common dyke systems which, coupled with the high estimated ascent rates, suggest that the magma of individual kimberlite clusters is delivered to the kimberlite pipes simultaneously. Furthermore, detailed facies studies of re-sedimented kimberlite in the A154 kimberlite pipe (coeval with the PETM) indicate that material from adjacent kimberlite pipes was deposited in the still open pipe [*Moss et al.*, 2008]. It is therefore likely that numerous kimberlite pipes composing a cluster erupt within relatively short time periods. Thus, our best estimates suggest that the eruption of a large kimberlite cluster is capable of delivering to the atmosphere the CO_2 required to produce the early initial warming associated with three early Cenozoic hyperthermals. We propose that the eruption of kimberlite clusters within the Lac de Gras kimberlite field produced the CO_2 responsible for the initial surface water warming associated with the early Cenozoic hyperthermals and that the transfer of those warm surface waters to intermediate depths led to thermal dissociation of sea floor methane hydrates and the resultant CIEs.

6. Conclusions

[14] The striking correspondence between the emplacement ages of three kimberlite clusters in the Lac de Gras field of the Slave Province and the three hyperthermals in the early Cenozoic suggests that they are genetically linked. Our calculations indicate that the eruption of three kimberlite clusters of the Lac de Gras field could have provided the CO_2 required for the initial warming of ocean water of the Paleocene-Eocene thermal maximum and two other early Cenozoic hyperthermals. As the global oceans buffered the increased atmospheric CO_2, ocean waters became increasingly acidified and produced the carbonate dissolution horizons. The transfer of warm surface ocean water to intermediate depths led to thermal dissociation of seafloor methane hydrates providing the isotopically depleted carbon that produced the carbon isotopic excursion. The rapid transfer of large amounts of CO_2 from the mantle to the atmosphere by kimberlite eruptions may thus provide a genetic link between mantle processes and enigmatic climatic events in the geologic record.

Acknowledgments

[15] This paper arose out of discussions regarding paleoclimate with a number of colleagues at McGill University, mainly Al Mucci, Eric Galbraith, Dirk Schumann and David Carozza. In addition, the ideas in this paper have benefited from discussions with William Manarik and Boswell Wing as well as statistical advice from Vincent Van Hinsberg. We appreciate the rigorous and many reviews of our manuscript, the thoughtful and helpful comments from Dante Canil were greatly appreciated.

References

Bernaola G., J. I. Baceta, X. Orue-Etxebarria, L. Alegret, M. Martin-Rubio, J. Arostegui, and J. Dinares-Turell (2007), Evidence of an abrupt environmental disruption during the mid-Paleocene biotic event (Zumaia section, western Pyrenees), *Geological Society of America Bulletin*, *119*(7-8), 785–795.

Blundy J., K. V. Cashman, A. Rust, and F. Witham (2010), A case for CO2-rich arc magmas, *Earth and Planetary Science Letters*, *290*(3-4), 289–301.

Bowen G. J., D. J. Beerling, P. L. Koch, J. C. Zachos, and T. Quattlebaum (2004), A humid climate state during the Palaeocene/Eocene thermal maximum, *Nature*, *432*(7016), 495–499.

Bralower T. J., D. J. Thomas, J. C. Zachos, M. M. Hirschmann, U. Rohl, H. Sigurdsson, E. Thomas and D. L. Whitney (1997), High-resolution records of the late Paleocene thermal maximum and circum-Caribbean volcanism: Is there a causal link?, *Geology*, *25*(11), 963–966.

Brooker R. A., S. C. Kohn, J. R. Holloway, and P. F. McMillan (2001), Structural controls on the solubility of CO2 in silicate melts: Part I: bulk solubility data, *Chemical Geology*, *174*(1-3), 225–239.

Caldeira K., and M. R. Rampino (1991), The Mid-Cretaceous Super Plume, carbon dioxide, and global warming, *Geophys. Res. Lett.*, *18*(6), 987–990.

Cande S. C., and D. V. Kent (1995), Revised calibration of the geomagnetic polarity timescale for the Late Cretaceous and Cenozoic, *J. Geophys. Res.*, *100*(B4), 6093–6095.

Canil D., and A. J. Bellis (2008), Phase equilibria in a volatile-free kimberlite at 0.1 *MPa and the search for primary kimberlite magma, Lithos*, *105*(1-2), 111–117.

Carozza D. A., L. A. Mysak, and G. A. Schmidt (2011), Methane and environmental change during the Paleocene-Eocene thermal maximum (PETM): Modeling the PETM onset as a two-stage event, *Geophys. Res. Lett.*, *38*(5), L05702.

Charles A. J., D. J. Condon, I. C. Harding, H. Pälike, J. E. A. Marshall, Y. Cui, L. Kump, and I. W. Croudace (2011), Constraints on the numerical age of the Paleocene-Eocene boundary, *Geochem. Geophys. Geosyst.*, *12*, Q0AA17.

Creaser R. A., H. Grütter, J. Carlson, and B. Crawford (2004), Macrocrystal phlogopite Rb-Sr dates for the Ekati property kimberlites, Slave Province, Canada: evidence for multiple intrusive episodes in the Paleocene and Eocene, *Lithos*, *76*(1-4), 399–414.

Dickens G. R. (2000), Methane oxidation during the Late Palaeocene Thermal Maximum, *Bull. Soc. Geol. Fr.*, *171*(1), 37–49.

Dickens G. R., M. M. Castillo, and J. C. G. Walker (1997), A blast of gas in the latest Paleocene: Simulating first-order effects of massive dissociation of oceanic methane hydrate, *Geology*, *25*, 259–262.

Dickens G. R., J. R. O'Neil, D. K. Rea, and R. M. Owen (1995), Dissociation of oceanic methane hydrate as a cause of the carbon isotope excursion at the end of the Paleocene, *Paleoceanography*, *10*, 965–971.

Faure S. (2010), World Kimberlites CONSOREM Database (Version 3).

Field M., and B. H. Scott Smith (1997), *Contrasting geology and near surface emplacement of kimberlite pipes in southern Africa and Canada*, Red Roof Design, Cape Town, South Africa.

Francis D., and M. Patterson (2009), Kimberlites and aillikites as probes of the continental lithospheric mantle, *Lithos*, *109*(1–2), 72–80.

Franz G. W., and P. J. Wyllie (1967), *Experimental studies in the system CaO–MgO–SiO2–CO2–H2O*, Wiley and Sons, New York.

Gerlach T. M., K. A. McGee, T. Elias, A. J. Sutton, and M. P. Doukas (2002), Carbon dioxide emission rate of Kilauea Volcano: Implications for primary magma and the summit reservoir, *J. Geophys. Res.*, *107*(B9), 2189.

Graham I., J. L. Burgess, D. Bryan, P. J. Ravenscroft, E. Thomas, B. J. Doyle, R. Hopkings, and K. A. Armstrong (1999), Exploration history and geology of the Diavik kimberlites, *Lac de Gras, Northwest Territories, Canada, Seventh International Kimberlite Conference*, *1*, 262–279.

Hancock H. J. L., and G. R. Dickens (2005), Carbonate dissolution episodes in Paleocene and Eocene sediment, *Shatsky Rise, West-central Pacific, Proceedings of the Ocean Drilling Program, Scientific Results*, *198*, 1–24.

Heaman L. M., B. A. Kjarsgaard, and R. A. Creaser (2003), The timing of kimberlite magmatism in North America: implications for global kimberlite genesis and diamond exploration, *Lithos*, *71*(2-4), 153–184.

Keeling C. D., T. P. Whorf, M. Wahlen, and J. van der Plichtt (1995), Interannual extremes in the rate of rise of atmospheric carbon dioxide since 1980, *Nature*, *375*(6533), 666–670.

Kent D. V. (2003), A case for a comet impact trigger for the Paleocene/Eocene thermal maximum and carbon isotope excursion, Earth Planet. *Sci. Lett.*, *211*, 13–26.

Kopp R. E., T. D. Raub, D. Schumann, H. Vali, A. V. Smirnov, and J. L. Kirschvink (2007), Magnetofossil spike during the Paleocene-Eocene thermal maximum: Ferromagnetic resonance, rock magnetic, and electron microscopy evidence from Ancora, New Jersey, United States, *Paleoceanography*, *22*(4), PA4103.

Kurtz A. C., L. R. Kump, M. A. Arthur, J. C. Zachos, and A. Paytan (2003), Early Cenozoic decoupling of the global carbon and sulfur cycles, *Paleoceanography*, *18*(4), 1090.

Leon-Rodriguez L., and G. R. Dickens (2010), Constraints on ocean acidification associated with rapid and massive carbon injections: The early Paleogene record at ocean drilling program site 1215, equatorial Pacific Ocean, Palaeogeography, Palaeoclimatology, *Palaeoecology*, *298*(3-4), 409–420.

Lockhart G., H. Grütter, and J. Carlson (2004), Temporal, geomagnetic and related attributes of kimberlite magmatism at Ekati, Northwest Territories, Canada, *Lithos*, *77*(1-4), 665–682.

Lourens L. J., A. Sluijs, D. Kroon, J. C. Zachos, E. Thomas, U. Rohl, J. Bowles, and I. Raffi (2005), Astronomical pacing of late Palaeocene to early Eocene global warming events, *Nature*, *435*(7045), 1083–1087.

McInerney F. A., and S. L. Wing (2011), The Paleocene-Eocene Thermal Maximum: A Perturbation of Carbon Cycle, Climate, and Biosphere with Implications for the Future, *Annual Review of Earth and Planetary Sciences*, *39*(1), 489–516.

Moore E. A., and A. C. Kurtz (2008), Black carbon in Paleocene-Eocene boundary sediments: A test of biomass combustion as the PETM trigger, Palaeogeography, Palaeoclimatology, *Palaeoecology*, *267*(1-2), 147–152.

Moss S., J. K. Russell, and G. D. M. Andrews (2008), Progressive infilling of a kimberlite pipe at Diavik, Northwest Territories, Canada: Insights from volcanic facies architecture, textures, and granulometry, *Journal of Volcanology and Geothermal Research*, *174*(1-3), 103–116.

Nielsen T. F. D., and S. M. Jensen (2005), The Majuagaa kimberlite dyke, Maniitsoq, southern West Greenland, Geological Survey of Greenland and Denmark, Report 2005/43.

Nielsen T. F. D., and K. K. Sand (2008), The Majuagaa kimberlite dike, Maniitsoq region, West Greenland: Constraints on an Mg-rich silicocarbonatitic melt composition from groundmass mineralogy and bulk compositions, *Canadian Mineralogist*, *46*(4), 1043–1061.

Nowicki T., L. Porritt, B. Crawford, and B. Kjarsgaard (2008), Geochemical trends in kimberlites of the Ekati property, Northwest Territories, Canada: Insights on volcanic and resedimentation processes, *Journal of Volcanology and Geothermal Research*, *174*(1-3), 117–127.

Nowicki T., B. Crawford, D. Dyck, J. Carlson, R. McElroy, P. Oshust, and H. Helmstaedt (2004), The geology of kimberlite pipes of the Ekati property, Northwest Territories, Canada, *Lithos*, *76*(1-4), 1–27.

Ootto J. W., and P. J. Wyllie (1993), Relationships between silicate melts and carbonate-precipitating melts in CaO-MgO-SiO2-CO2-H2O at 2 kbar, *Mineralogy and Petrology*, *48*(2-4), 343–365.

Panchuk K., A. Ridgwell, and L. R. Kump (2008), Sedimentary response to Paleocene-Eocene Thermal Maximum carbon release: A model-data comparison, *Geology*, *36*(4), 315–318.

Patterson M., D. Francis, and T. McCandless (2009), Kimberlites: Magmas or mixtures?, *Lithos*, *112*(Supplement 1), 191–200.

Pell J. A. (1997), Kimberlites in the Slave Craton, Northwest Territories, Canada: a preliminary review, *Russian Geology and Geophysics*, *38*(1).

Röhl U., T. J. Bralower, G. Norris, and G. Wefer (2000), New chronology for the late Paleocene thermal maximum and its environmental implications, *Geology*, *28*, 927–930.

Russell J. K., L. A. Porritt, Y. Lavallee, and D. B. Dingwell (2012), Kimberlite ascent by assimilation-fuelled buoyancy, *Nature*, *481*(7381), 352–356.

Scott Smith B. H. (2008), Canadian kimberlites: Geological characteristics relevant to emplacement, *Journal of Volcanology and Geothermal Research*, *174*(1-3), 9–19.

Secord R., P. D. Gingerich, K. C. Lohmann, and K. G. MacLeod (2010), Continental warming preceding the Palaeocene-Eocene thermal maximum, *Nature*, *467*(7318), 955–958.

Self S., M. Widdowson, T. Thordarson, and A. E. Jay (2006), Volatile fluxes during flood basalt eruptions and potential effects on the global environment: A Deccan perspective, *Earth and Planetary Science Letters*, *248*(1-2), 518–532.

Skinner E. M. W., and J. S. Marsh (2004), Distinct kimberlite pipe classes with contrasting eruption processes, *Lithos*, *76*(1-4), 183–200.

Sluijs A., H. Brinkhuis, S. Schouten, S. M. Bohaty, C. M. John, J. C. Zachos, G.-J. Reichart, J. S. Sinninghe Damste E. M. Crouch, and G. R. Dickens (2007), Environmental precursors to rapid light carbon injection at the Palaeocene/Eocene boundary, *Nature*, *450*(7173), 1218–1221.

Snyder D. B., and G. D. Lockhart (2005), Kimberlite trends in NW Canada, *Journal of the Geological Society*, *162*(5), 737–740.

Sobolev S. V., A. V. Sobolev, D. V. Kuzmin, N. A. Krivolutskaya, A. G. Petrunin, N. T. Arndt, V. A. Radko, and Y. R. Vasiliev (2011), Linking mantle plumes, large igneous provinces and environmental catastrophes, *Nature*, *477*(7364), 312–316.

Sparks R. S. J., M. C. Gardeweg, E. S. Calder, and S. J. Matthews (1997), Erosion by pyroclastic flows on Lascar Volcano, Chile, *Bulletin of Volcanology*, *58*(7), 557–565.

Sparks R. S. J., L. Baker, R. J. Brown, M. Field, J. Schumacher, G. Stripp, and A. Walters (2006), Dynamical constraints on kimberlite volcanism, *Journal of Volcanology and Geothermal Research*, *155*(1-2), 18–48.

Stasiuk L. D., G. D. Lockhart, W. W. Nassichuk, and J. A. Carlson (1999), Thermal maturity evaluation of dispersed organic matter inclusions from kimberlite pipes, Lac de Gras, Northwest Territories, Canada, *International Journal of Coal Geology*, *40*(1), 1–25.

Stasiuk M. V., C. Jaupart, and R. S. J. Sparks (1993), On the variations of flow rate in non-explosive lava eruptions, *Earth and Planetary Science Letters*, *114*(4), 505–516.

Svensen H. (2004), Release of methane from a volcanic basin as a mechanism for initial Eocene global warming, *Nature*, *429*, 542–545.

Sweet A. R., Stasiuk, M., Nassichuk, W.W., McIntyre, D.J., Catunneau, O. (2003), *Stratigraphy, paleoenvironments and thickness of inferred sedimentary cover and kimberlite crater fill processes, Lac de Gras, Northwest Territories, Canada, Proceedings of the Eighth International Kimberlite Conference*, Victoria, British Columbia, Canada.

Thomas D. J., J. C. Zachos, T. J. Bralower, E. Thomas, and S. Bohaty (2002), Warming the fuel for the fire: Evidence for the thermal dissociation of methane hydrate during the Paleocene-Eocene thermal maximum, *Geology*, *30*(12), 1067–1070.

Thomas E. (2003), Extinction and food at the seafloor: A high-resolution benthic foraminiferal record across the initial Eocene thermal maximum, Southern Ocean site 690, *Geological Society of America Special Papers*, *369*, 319–332.

Thomas E., and N. J. Shackleton (1996), The Paleocene-Eocene benthic foraminiferal extinction and stable isotope anomalies, Geological Society, London, *Special Publications*, *101*(1), 401–441.

Thomas E., and J. C. Zachos (2000), Was the late Paleocene thermal maximum a unique event?, *Geol. For. Stockh. Forh. [Trans. Geol. Soc. Stockholm]*, *122*, 169–170.

Tripati A., and H. Elderfield (2005), Deep-Sea Temperature and Circulation Changes at the Paleocene-Eocene Thermal Maximum, *Science*, *308*(5730), 1894–1898.

Wignall P. B. (2001), Large igneous provinces and mass extinctions, *Earth-Science Reviews*, *53*(1-2), 1–33.

Wilson L., and J. W. Head III (2007), An integrated model of kimberlite ascent and eruption, *Nature*, *447*(7140), 53–57.

Zachos J. C. (2003), A transient rise in tropical sea surface temperature during the Paleocene-Eocene thermal maximum, *Science*, *302*, 1151–1154.

Zachos J. C. (2004), Early Cenozoic Extreme Climates: The Walvis Ridge Transect, edited.

Zachos J. C., K. C. Lohmann, J. C. G. Walker, and S. W. Wise (1993), Abrupt Climate Change and Transient Climates during the Paleogene: A Marine Perspective, *The Journal of Geology*, *101*(2), 191–213.

Zachos J. C., M. Pagani, L. C. Sloan, E. Thomas, and K. Billups (2001), Trends, rhythms, and aberrations in global climate 65[thinsp]Ma to present, *Science*, *292*, 686–693.

Zachos J. C., S. M. Bohaty, C. M. John, H. McCarren, D. C. Kelly, and T. Nielsen (2007), The Palaeocene–Eocene carbon isotope excursion: constraints from individual shell planktonic foraminifer records, Philosophical Transactions of the Royal Society A: Mathematical, *Physical and Engineering Sciences*, *365*(1856), 1829–1842.

Zachos J. C., et al. (2005), Rapid acidification of the ocean during the Paleocene-Eocene thermal maximum, *Science*, *308*(5728), 1611–1615.

Zeebe R. E., J. C. Zachos, and G. R. Dickens (2009), Carbon dioxide forcing alone insufficient to explain Palaeocene-Eocene Thermal Maximum warming, *Nature geosciences*, *2*(8), 576–580.